REVIEWS OF MODERN PHYSICS, VOLUME 95, JANUARY–MARCH 2023

Measuring interfacial Dzyaloshinskii-Moriya interaction in ultrathin magnetic films

M. Kuepferling, A. Casiraghi, G. Soares, and G. Durin[*]

Istituto Nazionale di Ricerca Metrologica, Strada delle Cacce 91, 10135 Torino, Italy

F. Garcia-Sanchez[†]

Departamento de Fisica Aplicada, Universidad de Salamanca,
Plaza de la Merced s/n, 37008 Salamanca, Spain

L. Chen[‡] and C. H. Back[§]

Technical University Munich, James-Frank-Straße 1, 85748 Garching, Germany

C. H. Marrows

School of Physics and Astronomy, University of Leeds, Leeds LS2 9JT, United Kingdom

S. Tacchi[¶]

CNR, Istituto Officina dei Materiali–Perugia, c/o Dipartimento di Fisica e Geologia,
Universitá di Perugia, Via Alessandro Pascoli, 06123 Perugia, Italy

G. Carlotti

Dipartimento di Fisica e Geologia, Universitá di Perugia,
Via Alessandro Pascoli, 06123 Perugia, Italy

(published 22 March 2023)

The Dzyaloshinskii-Moriya interaction (DMI), one of the origins of chiral magnetism, is currently attracting considerable attention in the research community focusing on applied magnetism and spintronics. For future applications, an accurate measurement of its strength is indispensable. Here the state of the art of measurement techniques involving the coefficient of the Dzyaloshinskii-Moriya interaction, the DMI constant D, is reviewed, with a focus on systems where the interaction arises from the interface between two materials (i.e., the interfacial DMI). An overview of the experimental techniques, as well as their theoretical background and models for the quantification of the DMI constant, is given. The measurement techniques are divided into three categories: (a) domain-wall-based measurements, (b) spin-wave-based measurements, and (c) spin-orbit torque-based measurements. The advantages and disadvantages of each method are analyzed, and D values at different interfaces are compared. The review aims to obtain a better understanding of the applicability of the different techniques to various stacks and of the origin of apparent disagreements among literature values.

DOI: 10.1103/RevModPhys.95.015003

CONTENTS

---

[*] Corresponding author.
g.durin@inrim.it
[†] fgs@usal.es
[‡] lin0.chen@tum.de
[§] christian.back@tum.de
[¶] tacchi@iom.cnr.it

I. INTRODUCTION

Topological spin structures such as chiral domain walls (DWs) and skyrmions are emerging as promising information carriers for future spintronics technologies (Dieny *et al.*, 2020). Electric currents can drive such spin structures with an unprecedented level of efficiency, which makes them particularly attractive for innovative storage devices, including the racetrack memory (Parkin and Yang, 2015). The crucial ingredient needed for stabilizing these chiral spin textures is the Dzyaloshinskii-Moriya interaction (DMI).

The DMI is an anisotropic exchange interaction favoring a canted spin arrangement and has a net contribution only in systems without a center of inversion. It originates from the spin-orbit coupling (SOC) that acts as a perturbation on localized spin states. Given two neighboring spins $\vec{S}_i$ and $\vec{S}_j$, the DMI contributes to the Hamiltonian locally with a first bilinear energy term described by the following expression[1]:

$$\mathcal{H}_{\rm DMI} = \vec{D}_{ij} \cdot (\vec{S}_i \times \vec{S}_j), \tag{1.1}$$

where $\vec{D}_{ij}$ is a local DMI vector. Equation (1.1) is part of a generalized exchange interaction that relates $\vec{D}_{ij}$ to the isotropic exchange $-J_{ij}\vec{S}_i \cdot \vec{S}_j$ with exchange constant J_{ij}, i.e., Heisenberg exchange, in the case of localized electrons with a direct orbital overlap, or any other direct or indirect exchange described by this Hamiltonian. Contrary to the Heisenberg-type exchange, which favors collinear alignment, the DMI promotes an orthogonal arrangement between $\vec{S}_i$ and $\vec{S}_j$, with a chirality imposed by the direction of $\vec{D}_{ij}$.

The DMI was first proposed in the 1950s for antiferromagnets such as α-Fe$_2$O$_3$ to account for the existence of a weak ferromagnetism (Dzyaloshinskii, 1958; Moriya, 1960). In the following decades, several magnetic materials, such as spin glasses, orthoferrites, manganites, and superconducting cuprates (Fert and Levy, 1980; Levy and Fert, 1981; Coffey, Rice, and Zhang, 1991; Fert, 1991; Luo *et al.*, 1999; Bogdanov *et al.*, 2002), were investigated for their noncollinear or helical magnetism and for the influence of the DMI on the magnetic state. An important step toward multilayers, on which this review focuses, was taken by Fert (1991), who considered anisotropic pair interactions on surfaces or interfaces.

From an experimental point of view, the development of sophisticated imaging techniques to visualize the magnetic textures, such as spin-polarized scanning tunnel microscopy (SPSTM) and spin-polarized low-energy electron microscopy (SPLEEM), was crucial for triggering a renewed interest in the topic at the beginning of the 21st century, highlighted by Heinze (2000), Bode *et al.* (2007), and Heinze *et al.* (2011). In noncentrosymmetric single crystals with FeSi structure,[2] such as the materials MnSi and FeGe, it was shown that DMI gives rise to skyrmion lattices and other exotic spin textures at low temperatures, which could be directly visualized (Rößler, Bogdanov, and Pfleiderer, 2006; Mühlbauer *et al.*, 2009; Yu *et al.*, 2010).

More recently the presence of the DMI was also demonstrated in thin magnetic multilayers with perpendicular magnetic anisotropy (PMA) and shown to be localized at the interface between the layers (Zakeri *et al.*, 2010; Ryu *et al.*, 2012; Je *et al.*, 2013; Moon *et al.*, 2013). This interfacial DMI has since received broad attention from the magnetic community; see Hellman *et al.* (2017). It is of particular importance in the context of systems consisting of an ultrathin ferromagnetic (FM) film with PMA, in contact with a heavy metal (HM) underlayer or overlayer. In such a system the DMI arises due to the broken inversion symmetry at the interface between the two materials and the large SOC of the heavy metal atoms, which mediate the interaction between neighboring spins $\vec{S}_i$ and $\vec{S}_j$ of the ferromagnet. It follows that the DMI has an interfacial nature with a strength decreasing with the magnetic film thickness. If the symmetry breaking is due only to the interface and symmetry planes or the axes are always normal to the film plane, according to Moriya's rules the local DMI vector $\vec{D}_{ij}$ defined at the interface has to be necessarily perpendicular to the film normal, favoring canting of the out-of-plane magnetization; see Fig. 1. In this case the DMI vector can be written as $\vec{D}_{ij} = D_{ij}(\hat{r}_{ij} \times \hat{n})$, with $\hat{r}_{ij}$ the unit vector linking the two neighboring spins and $\hat{n}$ running along the direction of symmetry breaking, and thus normal to the film plane.

Bilayers composed of a thin magnetic film with PMA and a heavy metal are particularly interesting from the application point of view due to the fast domain-wall motion driven by an electric current in the presence of the DMI. Early experiments

---

[1] In particular, Eq. (1.1) is the antisymmetric part of the general expression for the bilinear spin-spin interaction (Moriya, 1960).

[2] Often called B20 according to classification of the journal *Strukturbericht*.

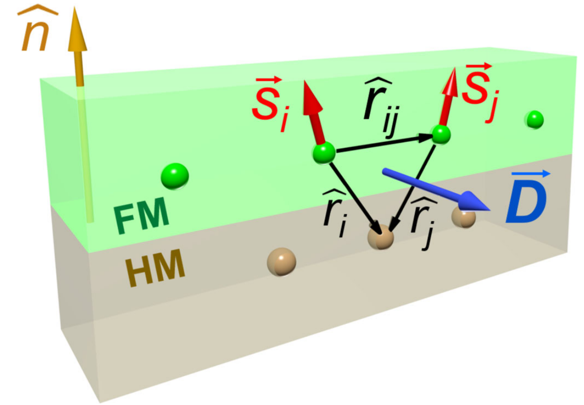

FIG. 1. Diagram of a system possessing an interfacial DMI. The exchange coupling between the spins $\vec{S}_i$ and $\vec{S}_j$ in a ferromagnetic (FM) layer is mediated by a heavy metal (HM) atom with large spin-orbit coupling. In this case, the local DMI vector with magnitude D_{ij} is perpendicular to the plane formed by the two atoms of the ferromagnetic layer and the one of the heavy metal layer.

on current-induced domain-wall motion in such systems could not fully unravel the driving mechanisms behind such motion. The conventional spin-transfer torque (STT) theory (Berger, 1996; Slonczewski, 1996) predicts motion in the direction of electron flow, which is the opposite of many observations (Moore *et al.*, 2008). On the other hand, the newly proposed spin-orbit torques (SOTs) [caused by the inverse spin galvanic (or Rashba) effect (ISGE) (Miron *et al.*, 2010, 2011) and the spin Hall effect (SHE) (Liu *et al.*, 2012; Haazen *et al.*, 2013)] did not have the correct symmetry to drive Bloch walls (Khvalkovskiy *et al.*, 2013), which were believed to be present in these ultrathin PMA films from purely magnetostatic considerations. This issue was resolved when it was suggested[3] that in the presence of the DMI Néel walls, which have a fixed chirality (Heide, Bihlmayer, and Blügel, 2008; Thiaville *et al.*, 2012), occur instead of the expected Bloch walls; see Fig. 2. A series of experimental works later confirmed these findings (Emori *et al.*, 2013; Ryu *et al.*, 2013), substantiating the view that DMI-stabilized Néel walls are moved mostly by the SHE torque. Ever since, DMI-based phenomena have resulted in an extremely active research field, often referred to as chiral magnetism.

For an isotropic ferromagnetic film (i.e., without special crystal symmetries, leading to an additional symmetry breaking), the DMI vector can usually be considered constant in the film plane (Moriya, 1960; Crépieux and Lacroix, 1998; Thiaville *et al.*, 2012), with a constant D describing the strength of the DMI. The interfacial DMI can then be thought of as equivalent to an effective in-plane magnetic field H_{DMI} that, acting across the domain wall, causes a reorientation of spins from the Bloch configuration into the Néel configuration with a fixed chirality (Thiaville *et al.*, 2012; Chen, Ma *et al.*, 2013). The strength of the interfacial DMI can then be measured as the DMI field (Thiaville *et al.*, 2012), to which it is proportional. The sign of D dictates the chirality of the Néel domain wall and, consequently, together with the sign of the spin Hall angle, the direction of the domain-wall motion under SHE torque.[4]

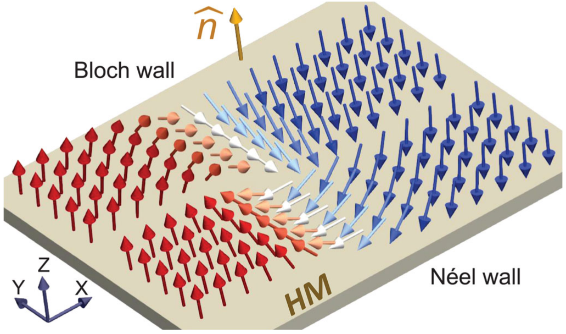

FIG. 2. Bloch and Néel configurations for a domain wall in a perpendicularly magnetized material. The Néel wall has left-handed chirality (↑ ← ↓), considering the positive Z direction parallel and fixed to the normal, which is depicted by the arrow $\hat{n}$ and defined pointing from the substrate to the magnetic film.

Because of the crucial role that the interfacial DMI plays in stabilizing chiral spin structures as well as in attaining extremely efficient domain-wall motion, it is of the utmost importance for the magnetic community to be able to accurately measure and predict the magnitude and sign of D in HM/FM combinations in order to be able to optimize these relevant effects. However, despite a rapidly increasing number of works quantifying the DMI through different experimental techniques, a considerable spread of data are currently present in the literature, and systematic studies or reviews are still rare (Choe and You, 2018). Not only are different measurement techniques found to provide contradictory values of D for nominally the same system, but controversies are also present when one utilizes the same method on nominally identical stacks, or different methods on the same sample (Soucaille *et al.*, 2016; Shahbazi *et al.*, 2019).

The most commonly used experimental techniques that in recent years have been employed to measure D in HM/FM structures can be broadly divided into the following three categories.

(1) *Domain-wall methods*.—Here D is extracted by measuring the domain-wall velocity or the domain-wall energy as a function of an in-plane magnetic field, by measuring the domain-wall spacing in stripe domain phases, or by directly measuring the domain-wall internal structure;

(2) *Spin-wave methods*.—Here D is extracted by measuring the nonreciprocity of propagating spin waves,

---

[3] Here direct imaging of the domain-wall chirality (Bode *et al.*, 2007) played a crucial role.

[4] The sign of D depends on the convention chosen in relation with the Hamiltonian (1.1), which can be either positive or negative. Throughout this review we use the plus sign in the Hamiltonian such that positive D corresponds to Néel domain walls with the right-handed (clockwise) chirality (↑ → ↓ or ↓ ← ↑), while negative D corresponds to Néel domain walls with the left-handed (counterclockwise) chirality (↑ ← ↓ or ↓ → ↑), where the up direction is defined by the normal in Fig. 2.

owing to the presence of DMI, in in-plane magnetized films.

(3) *Spin-orbit torque methods*.—Here D is extracted by measuring the field shift of the out-of-plane hysteresis loop under an in-plane magnetic field. While this method is used less frequently, it is transparent and reliable.

In this review we aim to provide an accurate analysis of the current state of the art regarding measurements of the interfacial DMI constant D based on the previously summarized techniques. Therefore, Secs. II–IV are devoted to analyzing each of the three main classes of the aforementioned techniques. In particular, in each section we start with a theoretical background, followed by an overview of the relevant experimental methodologies, and then a number of detailed tables with a collection of the relevant results published in the literature. Finally, for each of these three sections, we provide a critical discussion of the advantages and limitations of each experimental technique. Section V is devoted to a comparison and discussion of the methods and results obtained by the three classes of methods analyzed in the previous sections, as well as to final considerations about open problems and challenges. In particular, we address crucial aspects of the current research, such as the reliability of the different techniques, the choice of material combinations to achieve a large or small, negative or positive DMI, and the reasons for the spread of the results (such as the sample or interface quality, the growth conditions, and the reliability of the measuring techniques).

We anticipate that, with regard to the available literature, it is out of the scope of this review to give definitive recipes to prepare specific interfaces with a controlled value of DMI, evaluate the level of uncertainty of the different measurement methods, or classify the methods clearly according to their applicability. Therefore, one should consider our synoptic figures 28 and 29 as general guides for exploring measurement methods and ranges of values of common heterostructures. We emphasize instead the need for more systematic studies and hope that this review will stimulate the community to tackle metrological aspects of the measurement of the DMI at interfaces.

II. DOMAIN-WALL METHODS

A. Method overview

In ultrathin films with PMA, Bloch DWs are magnetostatically favored over Néel DWs.[5] However, the interfacial DMI manifests itself as a local effective in-plane magnetic field H_{DMI} that acts on the domain wall, which, when large enough to overcome the magnetostatic energy coming from the shape of the wall, converts Bloch DWs into Néel DWs with a chirality determined by the sign of D (Thiaville *et al.*, 2012; Chen, Ma *et al.*, 2013). By tuning the spin texture of the DWs toward a chiral Néel configuration, the interfacial DMI changes the static and dynamic properties of the DWs (Thiaville *et al.*, 2012).

The direct observation of chiral magnetization states in the presence of a DMI (Heinze, 2000; Bode *et al.*, 2007) was the key to understanding the modified DW dynamics. Indeed, first estimates of the DMI strength were obtained by fitting DW energies and numerical simulations of DW imaging in FM monolayers or double layers on tungsten heavy metal substrates (Bode *et al.*, 2007; Ferriani *et al.*, 2008; Heide, Bihlmayer, and Blügel, 2008; Zakeri *et al.*, 2010). A further experimental technique used to extract a quantitative value of D was the measurement of DW velocities driven by an electric current as a function of in-plane magnetic fields (Torrejon *et al.*, 2014). This is not surprising given the importance of the DMIs in these systems in the context of current-induced domain-wall motion experiments (Emori *et al.*, 2013; Ryu *et al.*, 2013). At the same time, it was proven that D could also be inferred by measuring magnetic-field-driven DW velocities (Je *et al.*, 2013; Hrabec *et al.*, 2014). H_{DMI}, and thus D, is extracted by analyzing the dependence of the DW velocity on the in-plane magnetic fields, which (added or subtracted to the H_{DMI}) can enhance or reduce the DW speed.

Following these early investigations (Je *et al.*, 2013; Ryu *et al.*, 2013; Hrabec *et al.*, 2014; Torrejon *et al.*, 2014), several subsequent works used DW motion, induced by either current or field, to estimate the strength and sign of the interfacial DMI in different material systems. Nucleation of reverse domains, which is a necessary step to study the motion of DWs, was shown to be dependent on D (Pizzini *et al.*, 2014), which established another path to access the magnitude and sign of D. Finally, the static properties of domains were shown to be altered by the presence of a DMI. This was observed from two points of view: First, the domain width is altered due the modification of the DW energy originating from the DMI (Moreau-Luchaire *et al.*, 2016). Second, the DMI affects the stability of the reversed domains and their field of annihilation (Hiramatsu *et al.*, 2014). Both effects have been used to estimate the magnitude of D.

DW dynamics in the presence of a DMI can be understood by making use of analytical 1D models. One-dimensional DW models have been established as useful tools to support computationally costly micromagnetic simulations as well as to interpret experimental results. As the name suggests, the 1D models for DW dynamics are based on the approximation that the magnetization $\vec{M}$ varies along one direction only, namely, the axis of a narrow wire, usually identified with x, as depicted in Fig. 3.

The origins of the 1D models can be traced back to the original description of Bloch walls (Bloch, 1932). The simplest form of the 1D model was introduced[6] by Schryer and Walker (1974) and Malozemoff and Slonczewski (1979) in the 1970s to study DW dynamics in PMA materials under the influence of an applied perpendicular field. Here DW dynamics was described in terms of two time-dependent variables (see Fig. 3): the DW position $q(t)$ along the wire axis and the DW angle $\Phi(t)$, defined as the in-plane (x-y)

---

[5] However, Néel DWs become energetically more favorable when the film is patterned into narrow wires (Koyama *et al.*, 2011).

[6] The 1D model was reported earlier by Walker (1956). A description of this work was given by Dillon (1963).

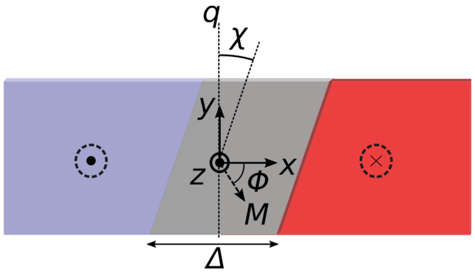

FIG. 3. Sketch of the collective coordinates used to describe DW dynamics in different types of 1D models. q is the domain-wall position, Φ is the angle of projection of the magnetization $\vec{M}$ in the x-y plane, Δ is the width, and χ is the tilting angle of the DW.

angle of the internal DW magnetization $\vec{M}$ with respect to the positive x axis.[7] The q-Φ model was later extended by Sobolev, Huang, and Chen (1994) and Sobolev, Chen, and Huang (1995) to describe DW dynamics in PMA materials under in-plane fields. Thiaville, García, and Miltat (2002) next adapted the 1D model to systems with in-plane magnetic anisotropy using the domain-wall width $\Delta(t)$ as an additional time-dependent variable in a revised q-Φ-Δ model.

More recently several other contributions have been included in the 1D model to take into account newly discovered effects, such as the STTs (Zhang and Li, 2004; Thiaville *et al.*, 2005), the SOTs (Boulle *et al.*, 2012; Hayashi *et al.*, 2012; Seo *et al.*, 2012; Martinez, Emori, and Beach, 2013; Martinez *et al.*, 2013) [see Eq. (2.2)], and the DMIs (Thiaville *et al.*, 2012; Emori *et al.*, 2013; Martinez, Emori, and Beach, 2013). In this context, D is then derived according to Emori *et al.* (2013):

$$D = \mu_0 H_{\mathrm{DMI}} M_{\mathrm{S}} \Delta, \tag{2.1}$$

where M_{S} is the saturation magnetization and $\Delta = \sqrt{A/K_{\mathrm{eff}}}$ is the DW width parameter, with A the exchange stiffness and $K_{\mathrm{eff}} = K_u - (1/2)\mu_0 M_{\mathrm{S}}^2$ the effective perpendicular anisotropy constant, corresponding to the intrinsic perpendicular anisotropy constant K_u decreased by the demagnetizing energy $(1/2)\mu_0 M_{\mathrm{S}}^2$.

Additions of thermal fluctuations (Martinez *et al.*, 2007) and of spatially dependent pinning (Consolo and Martinez, 2012) have helped to make the 1D model more realistic. Furthermore, considering experiments of fast current-driven DW motion (Ryu *et al.*, 2012), Boulle *et al.* (2013) proposed including DW tilting as an additional time-dependent variable $\chi(t)$ (defined as the angle of the DW normal plane with respect to the positive x axis), which led to the development of the q-Φ-χ model. Recently the 1D model was extended to implement all four collective coordinates, namely, q, Φ, Δ, and χ, with the aim of improving the agreement with experimental observations and micromagnetic simulations when large in-plane fields are applied (Nasseri *et al.*, 2017). Nasseri, Martinez, and Durin (2018) later showed that the simple two coordinate q-Φ model can grant higher accuracy when combined with an ansatz (which links collective coordinates to magnetization components) that takes into account magnetization canting within the domains under an in-plane field.

Here we provide a summary for the different DW-based techniques, explaining the underlying models (Sec. II.B), reviewing the main results achieved regarding the determination of D (Sec. II.C), and highlighting the respective advantages and limitations (Sec. II.D).

B. Theory and models

1. Current-driven domain-wall motion

The driving mechanism behind the current-induced motion of DWs in heavy metal/ferromagnet bilayers with PMA is now widely believed to be due to a combination of the SHE and the DMI, while the ISGE torque is considered to be negligible (Emori *et al.*, 2013; Ryu *et al.*, 2013; Martinez *et al.*, 2014), as the latter acts to stabilize Bloch walls (Miron *et al.*, 2011), and does not have the correct symmetry to drive DWs directly (Emori *et al.*, 2013; Khvalkovskiy *et al.*, 2013). The SHE in the heavy metal converts an in-plane charge current into a transverse spin current that gives rise to spin accumulation at the interface between the two layers, with consequent spin-current diffusion into the ferromagnet. This spin current can interact with the local magnetization by exerting a torque on it, known as the SHE SOT.[8] According to the 1D model, the amplitude of the effective field associated with the SHE SOT is expressed as (Thiaville *et al.*, 2012; Khvalkovskiy *et al.*, 2013)

$$H_{\mathrm{SHE}} = \frac{\hbar \theta_{\mathrm{SH}} |J_e|}{2\mu_0 |e| M_{\mathrm{S}} d} \cos(\Phi), \tag{2.2}$$

where θ_{SH} is the spin Hall angle, J_e is the electron current density, d is the thickness of the ferromagnetic film, and Φ is the internal in-plane DW angle as defined in Fig. 3. As a consequence, the SHE SOT can move DWs only if they possess a Néel component (i.e., $\Phi \neq \pm\pi/2$) in their spin structure, due to the interfacial DMI. The direction in which DWs move with the current depends both on the sign of the spin Hall angle θ_{SH} determined by the spin-orbit coupling constant of the heavy metal and on the sign of D (i.e., on the chirality of the DW). Micromagnetic simulations and the 1D model predict that the maximum velocity of the DWs driven by the SHE-SOT increases with the magnitude of D and saturates for larger currents showing a clear plateau (Thiaville *et al.*, 2012; del Real *et al.*, 2017; Lemesh and Beach, 2019).

The current-driven DW dynamics is dramatically affected by the application of an in-plane magnetic field H_x along the current direction. It is indeed due to this that DW velocity measurements as a function of H_x provide a means to quantify D. Given a fixed J, it is observed that Néel DWs with the same chirality $\uparrow \rightarrow \downarrow$ and $\downarrow \leftarrow \uparrow$ have the same velocity when

---

[7] According to these conventions, $\Phi = 0$ (π) corresponds to a right- (left-) handed chiral Néel DW, while $\Phi = \pm\pi/2$ corresponds to a Bloch DW.

[8] To be precise, fieldlike and dampinglike torques can occur as a result of ISGE or SHE effects.

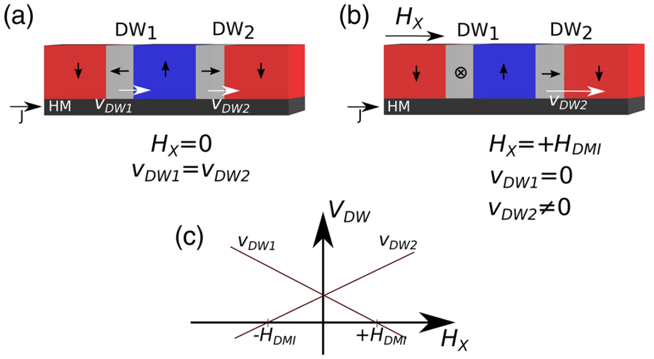

FIG. 4. Sketch of the dynamics of DWs driven by current in (a) the absence or (b) the presence of an applied in-plane field H_x. The white arrows indicate DW velocity. The strength of H_x applied in (b) matches that of the DMI field H_{DMI}, thus stopping the motion of DW_1. (c) Sketch of the velocity for the two DWs as a function of applied H_x.

$H_x = 0$, while they move with different velocities under a nonvanishing H_x. In particular, for a given sign of H_x the DW type for which H_x is parallel to H_{DMI} moves faster, while the other kind, where H_x partially compensates H_{DMI}, slows down with respect to its velocity at $H_x = 0$. The situation is reversed by changing the sign of the applied H_x. This noteworthy behavior has an important consequence: both DWs stop moving for a certain $|H_x|$, equal in strength but opposite in sign for $\uparrow\rightarrow\downarrow$ and $\downarrow\leftarrow\uparrow$DWs, respectively, as schematically shown in Fig. 4.

The applied H_x under which these Néel DWs stop moving (typically referred to as the "compensating" or "stopping" field) is the field that, opposing the DMI, restores a Bloch DW configuration, for which indeed no motion is expected via SHE SOT. As such, this compensating field H_x^* can be considered equivalent in strength (but opposite in sign) to the H_{DMI} acting locally across the DWs. In other words, because of the change in the DW internal magnetization angle (Ryu *et al.*, 2012), Néel DWs move faster or slower depending on whether the effective in-plane field experienced by the DW is enhanced ($H_x + H_{\mathrm{DMI}}$) or decreased ($H_x - H_{\mathrm{DMI}}$), respectively. In the latter case, DWs stop moving for $H_x = H_x^* = -H_{\mathrm{DMI}}$, when they become Bloch walls, and they reverse direction of motion for $H_x > -H_{\mathrm{DMI}}$, when the Néel configuration is reestablished but with an opposite chirality. However, identifying H_x^* with H_{DMI} is valid only if the conventional STT, due to the spin-polarized current in the ferromagnet (Berger, 1996; Slonczewski, 1996), can be neglected. When a significant STT is present, the relationship between the H_x^* and H_{DMI} in the 1D model becomes (Emori *et al.*, 2013; Ryu *et al.*, 2013)

$$H_x^* = H_{\mathrm{DMI}} + \mathrm{sgn}(\theta_{\mathrm{SH}})\frac{2}{\pi}\frac{\mu_B P}{\gamma e M_{\mathrm{S}}\Delta}|J_e|, \tag{2.3}$$

where μ_B is the Bohr magneton, P is the spin-current polarization, and γ is the gyromagnetic ratio. Equation (2.3) implies that H_x^* can depend on the amplitude of the current used to drive the DWs. When only a modest dependence of H_x^* on J_e is observed, as seen by Ryu *et al.* (2014) and Karnad *et al.* (2018), it is possible to conclude that the contribution of STT is small. In any case, once H_{DMI} is determined, the magnitude of D is derived through Eq. (2.1), while its sign is inferred from the direction of the DW motion and the sign of the spin Hall angle θ_{SH}.

The dependence of the DW velocity on an in-plane field for a fixed current density can be analytically described in the context of the 1D model, taking into account the STT, SHE SOT, and DMI (Thiaville *et al.*, 2012; Emori *et al.*, 2013; Ryu *et al.*, 2013). As seen in Fig. 4, the DW velocity is expected to be approximately linear with H_x around the compensating field H_x^*, and some experimental works derive H_{DMI} by linearly fitting the data (Ryu *et al.*, 2013; Torrejon *et al.*, 2014). In some cases, it has been observed that the DW velocity remains small or null in a large range of H_x around H_x^* (Ryu *et al.*, 2014; Lo Conte *et al.*, 2015, 2017), which is consistent with thermally activated creep regime and strong pinning effects. To account for it, the 1D model has been extended to include an effective pinning potential both without (Ryu *et al.*, 2014; Lo Conte *et al.*, 2017) and with thermal fields (Lo Conte *et al.*, 2015) to describe the influence of thermal fluctuations. In both cases, the modified 1D model has provided good agreement with the experimental data and has been used to extract H_{DMI}. The range of H_x values for which the DW velocity is negligible has been observed to decrease upon increasing the current density, due to a reduced influence of pinning (Ryu *et al.*, 2014).

Franken *et al.* (2014) and D.-Y. Kim *et al.* (2018) showed that D can also be quantified through current-driven DW dynamics by measuring the dependence of the DW depinning efficiency, rather than the DW velocity, on the in-plane field H_x. The efficiency of DW depinning is defined as

$$\epsilon = \mu_0 \frac{dH_{\mathrm{SHE}}}{dJ_e} \tag{2.4}$$

and is measured as the slope of the out-of-plane depinning field as a function of J_e. The DW depinning efficiency changes as a function of H_x due to the corresponding variation of the DW internal structure. In particular, ϵ is found to vanish at a certain H_x^*, equal in strength but opposite in sign for $\uparrow\rightarrow\downarrow$ and $\downarrow\leftarrow\uparrow$DWs. As previously discussed for the DW velocity dependence on H_x, this in-plane field H_x^* for which $\epsilon = 0$ represents the field at which a Bloch DW configuration is restored, and can thus be identified with H_{DMI}.

2. Field-driven domain-wall motion

The simplest and most common way to move DWs in PMA materials is by applying a perpendicular field H_z. To minimize the Zeeman energy associated with H_z, domains with magnetization along the field direction expand at the expense of the others, leading to DW motion. Schematically, when disorder is present, field-driven DW dynamics can show three distinctive regimes, creep, depinning, and flow, which occur in succession upon increasing H_z, as shown in Fig. 5(a). For sufficiently low driving fields ($H_z \ll H_{\mathrm{dep}}$), DWs move in the thermally activated creep regime, where they interact strongly with disorder, and their velocity grows exponentially as $v \sim \exp(-H_z)^{-1/4}$ (Lemerle *et al.*, 1998; Chauve, Giamarchi, and

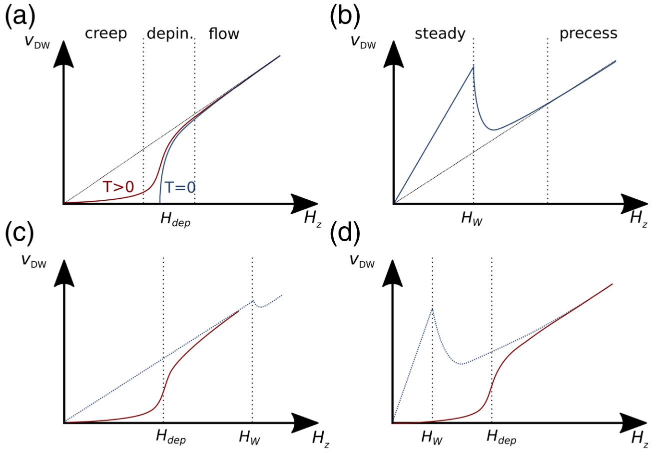

FIG. 5. Dependence of the DW velocity v_{DW} as a function of an increased applied field (schematic only). (a) Display of the three regimes: creep, depinning, and flow. The depinning transition, which is abrupt at zero temperature, shows some rounding due to thermal effects. In (b), two distinct regimes can be distinguished within the flow regime, namely, steady and precessional flow. The drop in the velocity is called Walker breakdown and occurs at the Walker field H_W. In experiments, the breakdown is visible if $H_W \gg H_{\mathrm{dep}}$, with two flow regimes as in (c), while it is hidden by the thermal regime when $H_W \ll H_{\mathrm{dep}}$ as in (d). Adapted from Metaxas *et al.*, 2007.

Doussal, 2000). Upon increasing H_z above a critical value, known as the depinning field H_{dep}, disorder starts to become irrelevant and the DW velocity grows as $v \sim (H_z - H_{\mathrm{dep}})^{\beta}$ (Chauve, Giamarchi, and Doussal, 2000), with β the depinning exponent at $T = 0$ as in Fig. 5(a). Finally, for $H_z \gg H_{\mathrm{dep}}$ the DW enters the flow regime where the velocity increases linearly with H_z.

In a system with no defects, following the 1D model the velocity grows up to the so-called Walker field H_W, which marks a significant decrease in DW velocity due to a change in its internal dynamics, as in Fig. 5(b) (Metaxas *et al.*, 2007). For $H_z \gg H_W$ the DW recovers a linear flow with H_z, albeit with a reduced mobility dv/dH. In real systems, one should consider the cases where $H_W \gg H_{\mathrm{dep}}$ or $H_W \ll H_{\mathrm{dep}}$, as in Figs. 5(c) and 5(d), where one or two flow regimes are found.

With the exceptions of a few works (Vaňatka *et al.*, 2015; Jué *et al.*, 2016a; Pham *et al.*, 2016; Ajejas *et al.*, 2017; Krizakova *et al.*, 2019; de Souza Chaves *et al.*, 2019), the DMI has been quantified mostly through experiments of field-driven DW motion in the creep regime, which is addressed in Sec. II.B.2.a. Methods to extract the DMI from DW dynamics in the flow regime are discussed later.

a. Creep regime

In the creep regime, DWs are driven by modest fields (typically down to a few percent of H_{dep}) and move slowly by thermal activation, interacting strongly with disorder of various origins (pinning defects, film thickness variations, M_S inhomogeneities, etc.). The DW creep dynamics is understood in terms of the motion of a one-dimensional elastic line in a two-dimensional disordered potential. The dependence of the DW velocity v on the applied field H_z is described using the so-called creep law (Lemerle *et al.*, 1998; Chauve, Giamarchi, and Doussal, 2000):

$$v = v_0 \exp\left[-\zeta(\mu_0 H_z)^{-\mu}\right], \tag{2.5}$$

where v_0 is the characteristic speed proportional to the attempt frequency for DW propagation, ζ is a scaling constant, and $\mu = 1/4$ is the scaling exponent for the 1D elastic line.

Creep motion of DWs driven by a perpendicular field H_z is significantly altered by the simultaneous presence of an in-plane field H_x, as previously discussed for the current-driven case; see Sec. II.B.1. Indeed, it had been observed experimentally that when a circular magnetic bubble expands under the application of H_z only, the radial symmetry is maintained and the bubble grows isotropically (thus retaining its original shape). However, the symmetry is broken when the bubble is expanded under the application of both H_z and H_x, as Néel $\uparrow \rightarrow \downarrow$ and $\downarrow \leftarrow \uparrow$DWs acquire different velocities along the direction of the applied H_x. This circumstance was first observed for continuous films of Pt/Co/Pt (see Fig. 6) by Kabanov *et al.* (2010), who mentioned the interfacial DMI as a possible origin. Only later was it fully understood and modeled in the context of DW creep.

The first model proposed to explain the asymmetric motion of Néel DWs with the in-plane field suggested modifying the creep law [Eq. (2.5)] by changing the scaling parameter ζ to take into account the dependence of the DW energy on the in-plane field (Je *et al.*, 2013):

$$\zeta(H_x) = \zeta_0[\sigma(H_x)/\sigma(0)]^{1/4}, \tag{2.6}$$

where ζ_0 is a scaling constant and σ is the DW energy density. The dependence of the DW energy density on the in-plane field has been calculated as (Thiaville *et al.*, 2012; Je *et al.*, 2013)

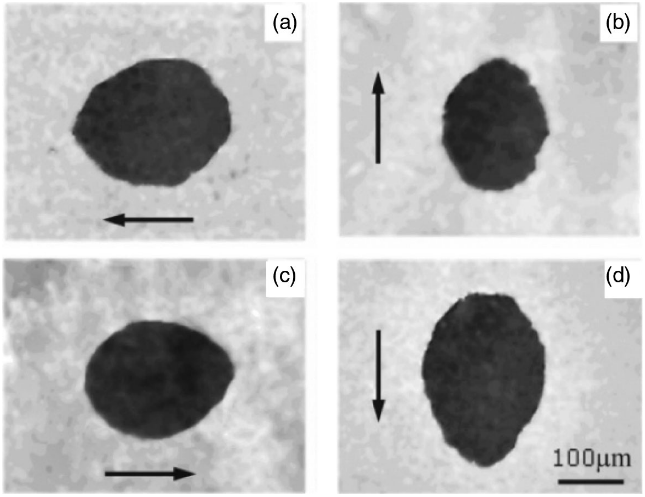

FIG. 6. First observation by the magneto-optical Kerr effect (MOKE) of the asymmetric expansion of a bubble under an in-plane magnetic field in a continuous film of Pt/Co/Pt. Arrows show the in-plane field directions. From Kabanov *et al.*, 2010.

$$\sigma(H_x) = \sigma_0 - \frac{\pi^2 \Delta \mu_0^2 M_\mathrm{S}^2}{8K_\mathrm{D}}(H_x + H_\mathrm{DMI})^2 \tag{2.7}$$

when the condition $|H_x + H_\mathrm{DMI}| < 4K_\mathrm{D}/\pi\mu_0 M_\mathrm{S}$ is satisfied. In this case the effective field acting on the DW is not strong enough to fully convert it into a Néel DW. Otherwise, for higher fields and fully Néel DWs the expression becomes

$$\sigma(H_x) = \sigma_0 + 2K_\mathrm{D}\Delta - \pi\Delta\mu_0 M_\mathrm{S}|H_x + H_\mathrm{DMI}|. \tag{2.8}$$

In Eqs. (2.6)–(2.8), $\sigma_0 = 4\sqrt{AK_\mathrm{eff}}$ is the Bloch DW energy density, $\Delta = \sqrt{A/K_\mathrm{eff}}$ is the domain-wall width parameter, and $K_\mathrm{D} = N_x \mu_0 M_\mathrm{S}^2/2$ is the DW shape anisotropy energy density,[9] with the demagnetizing factor of the DW given by $N_x = \ln(2)d/\pi\Delta$, with d the magnetic film thickness (Tarasenko *et al.*, 1998). In other words, this model predicts that the effective in-plane field acting locally on the Néel DWs on either side of the bubble can be increased (decreased) if H_x and H_DMI have the same (opposite) sign, resulting in smaller (larger) DW energy σ and thus a faster (slower) DW, just as in the current-driven case; see Fig. 7.

The field $H_x^* = -H_\mathrm{DMI}$ at which Néel DWs are converted into Bloch DWs is then equal in magnitude but opposite in sign for ↑↓ and ↓↑DWs. Notice that, unlike in the current-driven case, field-driven Bloch DWs do not stop moving under the in-plane field H_x^*, since the perpendicular field H_z keeps expanding the magnetic bubble to minimize the Zeeman energy. Rather, in field-driven experiments $|H_x^*| = H_\mathrm{DMI}$ corresponds to a minimum in the DW velocity. In this simple model, the velocity for each type of DW should be symmetric around its own minimum, as in Fig. 7(c), although in many experimental cases it is not. It follows that in the absence of DMI, i.e., when the bubble DW is in the Bloch configuration, both sides of the bubble have the same velocity dependence with H_x, show a minimum at $H_x = 0$, and are symmetric around $H_x = 0$ (Kim, Kim *et al.*, 2015). This model can be used to fit the dependence of bubble DW velocities on in-plane field using three fitting parameters: v_0, ζ_0, and H_DMI itself. Alternatively, the scaling parameters v_0 and ζ_0 can be extracted separately as the intercept and gradient of a linear fit to the curve $\ln(v)$ vs $H_z^{-1/4}$ for $H_x = 0$, thus leaving H_DMI as the only fitting parameter of the v dependence on H_x. Once H_DMI has been determined, the magnitude of D is derived through Eq. (2.1), while its sign is inferred from the orientation of the bubble asymmetry with respect to the H_x direction.

This modified creep model, in which the in-plane field affects DW dynamics only through a variation of domain-wall energy, has been successfully applied to fit several experimental data and to estimate the interfacial DMI constant D (Je *et al.*, 2013; Hrabec *et al.*, 2014; Petit *et al.*, 2015; Khan *et al.*, 2016; Yu, Qiu *et al.*, 2016; Kim, Yoo *et al.*, 2017; Wells *et al.*, 2017; Kuświk *et al.*, 2018; Shahbazi *et al.*, 2018). However, for a growing number of experiments, as in Fig. 8, the model fails to provide an adequate description of the data, which often show an asymmetric behavior around the minimum velocity (Lavrijsen *et al.*, 2015; Jué *et al.*, 2016b; Lau *et al.*, 2016; Soucaille *et al.*, 2016; Pellegren, Lau, and Sokalski, 2017; Cao, Zhang *et al.*, 2018; D.-Y. Kim *et al.*, 2018; Shepley *et al.*, 2018; Shahbazi *et al.*, 2019), a local peak in velocity (Lavrijsen *et al.*, 2015; Soucaille *et al.*, 2016; Balk *et al.*, 2017), or even a maximum in velocity in the creep regime (Vaňatka *et al.*, 2015).

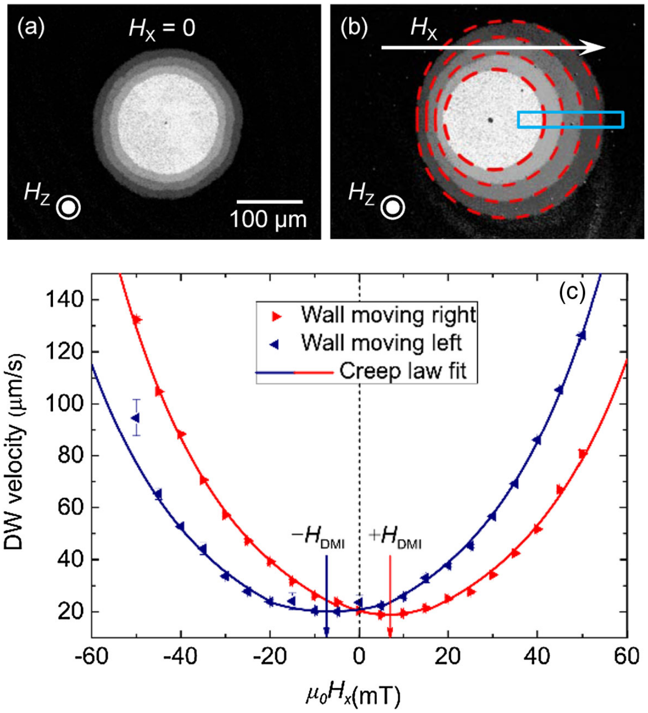

FIG. 7. Dynamics of bubble DWs driven by a perpendicular field $\mu_0 H_z = 3$ mT in (a) the absence (or (b) the presence of an in-plane field $\mu_0 H_x = 50$ mT in a Ta(5 nm)/Pt(2.5 nm)/Co(0.3 nm) thin film with PMA. Each image is obtained by adding four sequential images with a fixed time step (0.4 s), which are captured using a magneto-optical Kerr effect microscope. The blue box in (b) designates the field of measurement. From Je *et al.*, 2013. (c) A typical symmetric profile of the DW moving left and right as a function of the in-plane field H_x in a Ta(5 nm)/Co$_{20}$Fe$_{60}$B$_{20}$(0.8 nm)/MgO(2 nm) thin film. Here the velocity minima occur at $|H_x| = H_\mathrm{DMI}$. From Khan *et al.*, 2016.

To explain these nonsymmetric results, several different mechanisms have been suggested. Jué *et al.* (2016b) proposed to neglect any DW energy contribution and considered a DW chirality-dependent damping, which acts as a dissipative SOT on the DW: this damping would modulate the attempt frequency for DW motion, and would thus modify the characteristic speed v_0 of the creep law; see Eq. (2.5). On the contrary, Lavrijsen *et al.* (2015) suggested that chiral damping could not explain the asymmetry of their own results, as v_0 was found to be symmetric with respect to H_x. The importance of considering possible H_x dependences on both creep parameters v_0 and ζ (not necessarily related to chiral damping) was highlighted by Balk *et al.* (2017) and Shepley *et al.* (2018). While Shepley *et al.* showed that the dependence on H_x is asymmetric for both v_0 and ζ, Balk *et al.* modeled their results through a modified creep law that takes H_x into account for both parameters. By combining Eqs. (2.5),

---

[9] K_D represents the fact that Bloch DWs are magnetostatically more stable in the absence of a DMI due to the PMA of the films.

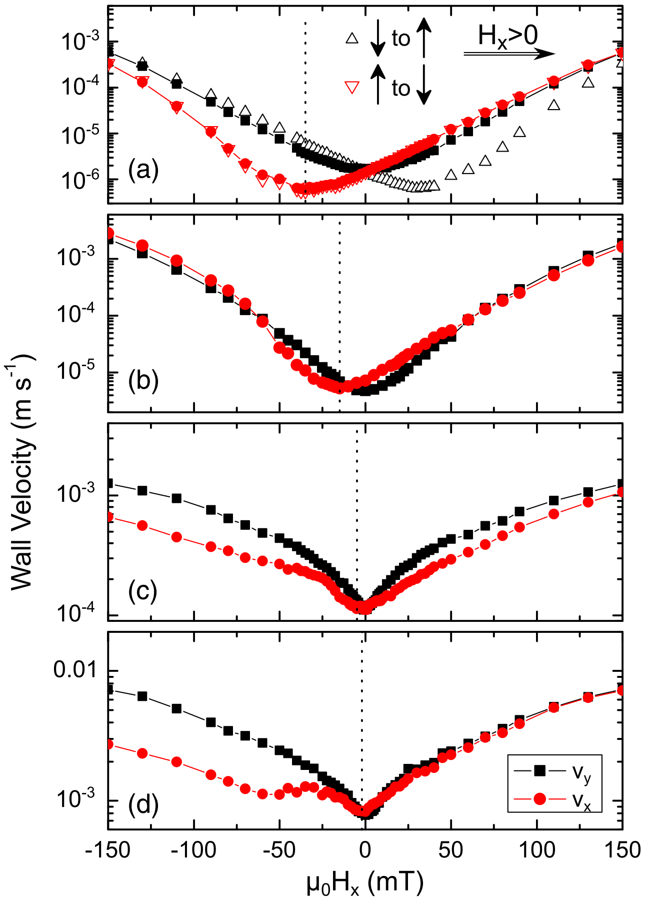

FIG. 8. Example of asymmetry of the domain-wall velocity profile as a function of the in-plane field (red dots) for a set of multilayers with nominal structure $\mathrm{Si/SiO_2}/X(t)/\mathrm{Co_{20}Fe_{60}B_{20}}(1\ \mathrm{nm})/\mathrm{MgO}(2\ \mathrm{nm})/\mathrm{Ta}(1\ \mathrm{nm})$, with four underlayers $X(t)$: (a) W (2 nm), (b) W (3 nm), (c) TaN (1 nm), and (d) Hf (1 nm). All cases are highly asymmetric in the velocity profile, even showing a local maximum, as in (d). Note that the velocity in the direction orthogonal to the in-plane field (black squares) remains symmetric. From Soucaille *et al.*, 2016.

and (2.6), with their expression for v_0 they were able to fit velocity versus H_x curves that showed a local peak around $H_x = 0$, introducing a local anisotropy due to pinning K_{pin} and having ζ_0 and H_{DMI} as fitting parameters.

Several analytical and numerical studies were devoted to understanding these features. Kim, Kim, and Choe (2016) attributed the asymmetry in the DW energy density σ to the asymmetric variation of the DW width with H_x, which was later confirmed by micromagnetic simulations (Sarma *et al.*, 2018). Lau *et al.* (2016) described the velocity asymmetry in terms of the Wulff construction, which yields a methodology determining the shape of a magnetic bubble, although it does not explicitly provide a model for the velocity as a function of the in-plane field. They also speculated that nucleation and annihilation of Bloch lines may be responsible for a peculiar flattening of magnetic bubbles, which could in turn cause the observed velocity asymmetry. This was again confirmed through micromagnetic simulations by Sarma *et al.* (2018). Pellegren, Lau, and Sokalski (2017) argued that under an applied magnetic field H_x, where the DW energy density σ becomes anisotropic with respect to the DW orientation in the film plane, the correct elastic energy that should be considered to describe the creep regime does not simply identify with σ, as typically assumed in the phenomenological model of creep (Lemerle *et al.*, 1998). Rather, to reproduce the asymmetry in their velocity curves, they proposed that σ should be replaced by the DW stiffness $\tilde{\sigma} = \sigma + \sigma''$, with $\sigma'' = \partial^2\sigma/\partial\Theta^2$, where Θ is the azimuthal angle of the DW normal. The H_{DMI} value extracted using this stiffness model was found to be higher than the field at which the minimum in velocity is observed. In a later work, Lau *et al.* (2018) proposed upgrading the stiffness model by taking into account a possible variation of the characteristic speed v_0 with H_x, which they also speculated could be due to a chiral damping mechanism. Through this improved model, they could fit velocity curves as a function of H_x that not only are asymmetric about the minimum but also show a crossover between DW velocities at opposite sides of the bubble. More recently another model was advanced by Shahbazi *et al.* (2019) to explain the presence of both asymmetry and DW crossover in the velocity curves. Here the DW depinning field H_{dep} is allowed to vary with H_x in a manner determined from micromagnetic simulations. Notably this work showed that the velocity minimum underestimates H_{DMI}, as was also found for the stiffness model (Pellegren, Lau, and Sokalski, 2017). This was confirmed by Hartmann *et al.* (2019) and Géhanne *et al.* (2020): the former reconsidered the change of the DW stiffness due to deformation as an angular shape, and minimizing the energy of the system with a semianalytical approach they were able to calculate the velocity profile and show that the minimum of the velocity does not occur at H_{DMI}. The latter showed that H_x can also modify the characteristic length scale of pinning, in strong correlation with the DW width, again implying that the minimum of the velocity could not correspond to the H_{DMI} field.

b. Flow regime

According to the 1D model (Thiaville *et al.*, 2012), the presence of DMI significantly increases the Walker field H_W. Indeed, in samples with a strong enough DMI to convert the wall to a fully Néel form, H_W is proportional to H_{DMI}:

$$H_W \propto \alpha H_{\mathrm{DMI}}, \tag{2.9}$$

where α is the Gilbert damping constant (Thiaville *et al.*, 2012). The DW velocity at the Walker field can thus be expressed as

$$v_W = \gamma_0 \frac{\Delta}{\alpha} H_W \sim \gamma \frac{D}{M_S}, \tag{2.10}$$

where $\gamma_0 = \mu_o \gamma$ and γ is the gyromagnetic ratio. In contrast to the prediction of the 1D model, it was found experimentally and confirmed by 2D micromagnetic simulations that in samples with a large DMI, the DW velocity does not decrease at fields larger than H_W, but instead reaches a plateau (Pham *et al.*, 2016; Yoshimura *et al.*, 2016; Ajejas *et al.*, 2017). This fact originates from the complex meander structure that the DW adopts at velocities above H_W, with continuous nucleation and annihilation of pairs of vertical Bloch lines (Pham *et al.*, 2016; Yoshimura *et al.*, 2016). Measurements of this roughly constant velocity, which corresponds to v_W, provide a simple way to determine D for samples with large DMIs. A combination of experiments and modeling has been used to show that D is also associated with the value of H_z at which the end of the plateau is reached (Krizakova *et al.*, 2019).

In other works (Vaňatka *et al.*, 2015; Pham *et al.*, 2016; Ajejas *et al.*, 2017; de Souza Chaves *et al.*, 2019) measurements of the minimum DW velocity as a function of H_x in the flow regime have also been used to quantify D: in the flow regime the DW velocity depends only on the DW width (not then on the DW energy), and this assumes the minimum value when there is a Bloch DW. Indeed, it has been shown that under certain conditions the 1D model provides an expression for the DW velocity that exhibits a parabolic dependence on $H_x + H_{\mathrm{DMI}}$ (D.-H. Kim *et al.*, 2019).

3. Equilibrium stripe domain pattern

The demagnetized state of PMA materials consists of a complex domain pattern, usually in the form of labyrinth structures of domains pointing either up or down. If the thickness of the sample is small, the equilibrium domain width can exceed the sample dimensions, and such structures are not expected. Examples of the typical patterns are shown in Fig. 9 for a multilayer of $\mathrm{Pt/Co/Al_2O_3}$ taken from Legrand *et al.* (2018). The exact demagnetized pattern depends on the direction and the history of the applied field: when an out-of-plane field is applied, a maze domain structure is created [Fig. 9(a)], while for an in-plane field domain walls remain almost parallel and typically form a stripe structure [Fig. 9(b)]. In the latter, the width and density of the domains can be used to estimate the domain-wall energy. As suggested by the theory developed for infinite parallel stripe domains (Málek and Kamberský, 1958; Kooy and Enz, 1960), the domain width is a function of the domain-wall energy, which includes magnetostatic, anisotropy, Zeeman, and exchange terms. Néel walls, which are favored by DMIs, have a reduced energy, and consequently the DMI markedly affects the equilibrium domain width.

For domain widths much larger than the domain-wall width, as is generally the case for PMA materials, the magnetostatic contribution comes only from surface charges at the top and bottom surfaces, so the DW energy is calculated as

$$\sigma_{\mathrm{DW}} = \frac{2A}{\Delta} + 2K_{\mathrm{eff}}\Delta - \pi\cos(\Phi)|D|, \tag{2.11}$$

where Φ is the angle of the internal DW magnetization defined in Fig. 3. The minimization of the energy with respect to the domain width Δ and core angle Φ gives the value of the equilibrium domain width: a critical value D_c is obtained. For $D > D_c$ the preferred configuration is a Néel wall, and for $D \leq D_c$ it gradually transforms into a Bloch wall as D approaches zero.

Initially, this method was limited to Néel walls only, with $D > D_c$, and hence $\cos(\Phi) = 1$, such that the DW energy density simplifies to $\sigma_{\mathrm{DW}} = \sigma_0 - \pi|D|$. Later the inclusion of the angle of the wall Φ in Eq. (2.11) removed this limitation (Lemesh, Büttner, and Beach, 2017; Meier, Kronseder, and Back, 2017). A further improvement took into account the dipolar terms coming from the internal structure of the DW and/or from the DW interaction (Lemesh, Büttner, and Beach, 2017). This is important in thicker samples, as the dipolar energy causes the internal magnetization to vary along the thickness, even in the presence of a DMI. To account for all these situations, the model was extended, thereby allowing a different angle Φ for each layer of the sample (Lemesh and Beach, 2018).

The analytical expression for the DW energy σ_{DW} as a function of the periodicity w of the domains, which is twice the domain width, is

$$\frac{\sigma_{\mathrm{DW}}}{\mu_0 M_S^2 d} = \frac{w^2}{d^2\pi^3} \sum_{\mathrm{odd}\, n=1}^{\infty} \frac{1 - (1 + 2\pi n d/w)e^{-2\pi n d/w}}{n^3}, \tag{2.12}$$

where d is the thickness. From the experimentally obtained domain width one can then calculate the domain-wall energy and estimate the DMI constant using one of the previously derived approximations.

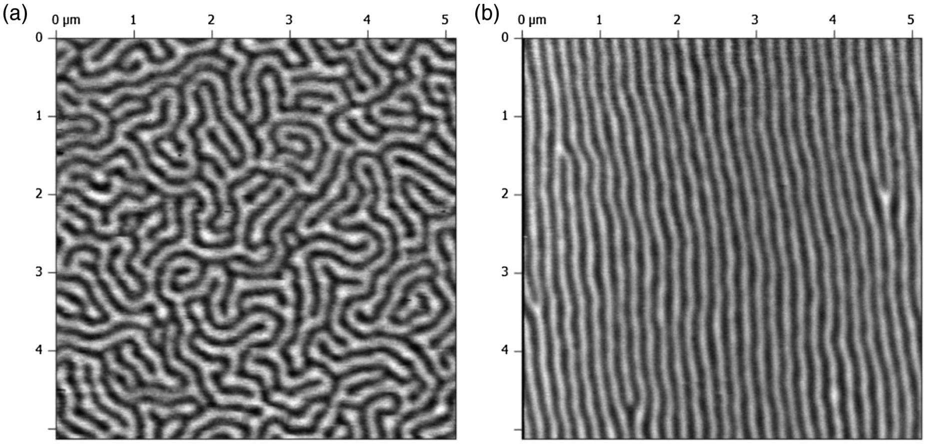

FIG. 9. MFM domain patterns for (a) an out-of-plane and (b) an in-plane demagnetized multilayer composed of $[\mathrm{Pt(1\ nm)/Co(0.8\ nm)/Al_2O_3(1\ nm)}]_{20}$. From Legrand *et al.*, 2018.

This general method has been applied in three different ways: comparisons to micromagnetic simulations (Moreau-Luchaire *et al.*, 2016; Legrand *et al.*, 2018), analytical estimations (Woo *et al.*, 2016, 2017; Yu *et al.*, 2017; Wong *et al.*, 2018), and scaling of the energy of an experimental image (Baćani *et al.*, 2019).

4. Magnetic stripe annihilation

Two parallel domain walls in a thin film with strong enough DMI are homochiral Néel walls. Since the chirality of the domain walls is the same, either left-handed or right-handed, the core magnetization of those parallel domain walls point in opposite directions. Such a pair of domains constitutes a topological structure. This situation differs from the case of the absence of a DMI, where the core magnetization of the Bloch walls points in the same direction, but not in a fixed orientation. The annihilation of these two parallel Néel walls depends on the strength of the DMI due to the topological configuration. This fact was confirmed by simulations (Hiramatsu *et al.*, 2014; Martínez and Alejos, 2014). To annihilate the walls, an out-of-plane field is applied that reduces the size of the domain disfavored by the field. This domain achieves a minimum size until the walls meet as a so-called winding pair to form a 360° wall that annihilates when a given value of the out-of-plane field is exceeded. From the determination of the field of annihilation and the minimum domain width, the DMI can be extracted when compared to the corresponding simulations (Hiramatsu *et al.*, 2014). An example given by Benitez *et al.* (2015) for the annihilation field dependence on the DMI calculated by means of micromagnetic simulations is shown in Fig. 10. More recently a formula for the minimum width of stripe domains was derived (Lemesh, Büttner, and Beach, 2017) using the analytical formulation of Eq. (2.12). This allowed the extraction of the DMI value without the performance of systematic micromagnetic simulations.

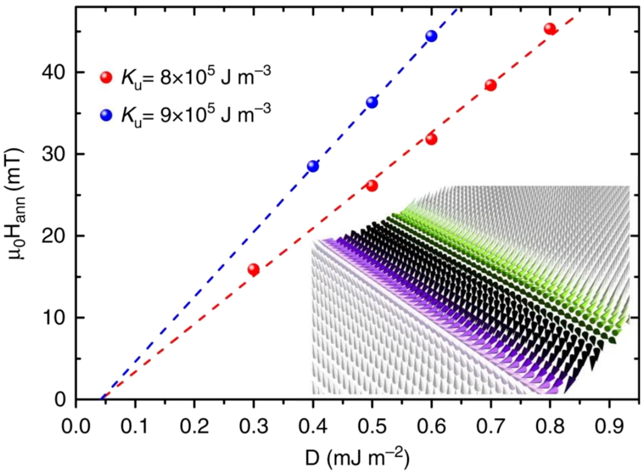

FIG. 10. Annihilation field of two homochiral walls as a function of the DMI value calculated from micromagnetic simulations for two different anisotropy values. Inset: magnetic configuration of the two Néel walls squeezed together by the perpendicular field. From Benitez *et al.*, 2015.

The analytical formula for the domain-wall energy σ_{DW} obtained from the minimum domain width $w_{\min}$ is given by

$$\frac{\sigma_{\mathrm{DW}}}{\mu_0 M_{\mathrm{S}}^2 d} = \frac{1}{2\pi}\{\ln[1+(w_{\min}/d)^2] + (w_{\min}/d)^2 \ln[1+(w_{\min}/d)^{-2}]\}. \tag{2.13}$$

As in the previous method, this allows the value of the domain-wall energy density, which is also a function of the DMI constant, to be extracted. Using the same expressions for the energy density as given in Eq. (2.11), one can estimate its value.

5. Nucleation field

As stated, the energy of a domain wall is reduced by the presence of a DMI. This modification also affects the energy barrier relevant for nucleation of reversed domains. Pizzini *et al.* (2014) showed that the nucleation process is affected by the presence of a DMI. They distinguished between nucleation at the edge of the patterned sample and in the center of the magnetic film. They showed that the nucleation of reversed domains at the edge depends on the value of the in-plane applied field, and that it is asymmetric with respect to the combination of the DMI sign and the in-plane field direction. The nucleation is favored at the edge of the sample having a nucleated wall with the core magnetization in the direction of the in-plane field. The half-droplet model (Vogel, Moritz, and Fruchart, 2006) applied by Pizzini *et al.* describes the nucleation of a magnetic domain at the side edge under the application of an in-plane magnetic field. The out-of-plane nucleation field for a reversed domain is

$$H_{\mathrm{n}} = \frac{\pi \sigma^2 d}{2\mu_0 M_s p k_{\mathrm{B}} T} \tag{2.14}$$

where σ is the domain-wall energy associated with the bubble, T is the temperature, and p is the factor related to the waiting time according to $\tau = \tau_0 \exp(p)$, where τ_0 is the attempt frequency. The DW energy is a function of the in-plane field and the DMI constant. From the best adjustment of their numerical model to the experimental results, they were able to estimate the DMI constant in Pt/Co/AlO$_x$.

In the case of a bubble domain away from the edges, Pizzini *et al.* (2014) concluded that the Zeeman energy gained within the half-droplet having a DW magnetization component parallel to the in-plane field is compensated for by the loss of energy within the half droplet with the opposite magnetization [see the orientation of the magnetization in Fig. 11(b)], while this is not true for an incomplete bubble nucleated at the edge. Therefore, the nucleation field for a complete bubble is independent of the in-plane field value. This fact agrees well with their model shown in Fig. 11(a) and their measurements shown in Fig. 11(b).

More recently Kim, Jang *et al.* (2017) realized that such an argument does not hold for bubbles in films above a critical in-plane field value, corresponding to the DMI field, where the energy of the bubble is altered due to the fact that the magnetization at its boundary aligns with the in-plane field. Hence, Fig. 11(c) is no longer valid. This fact leads to a

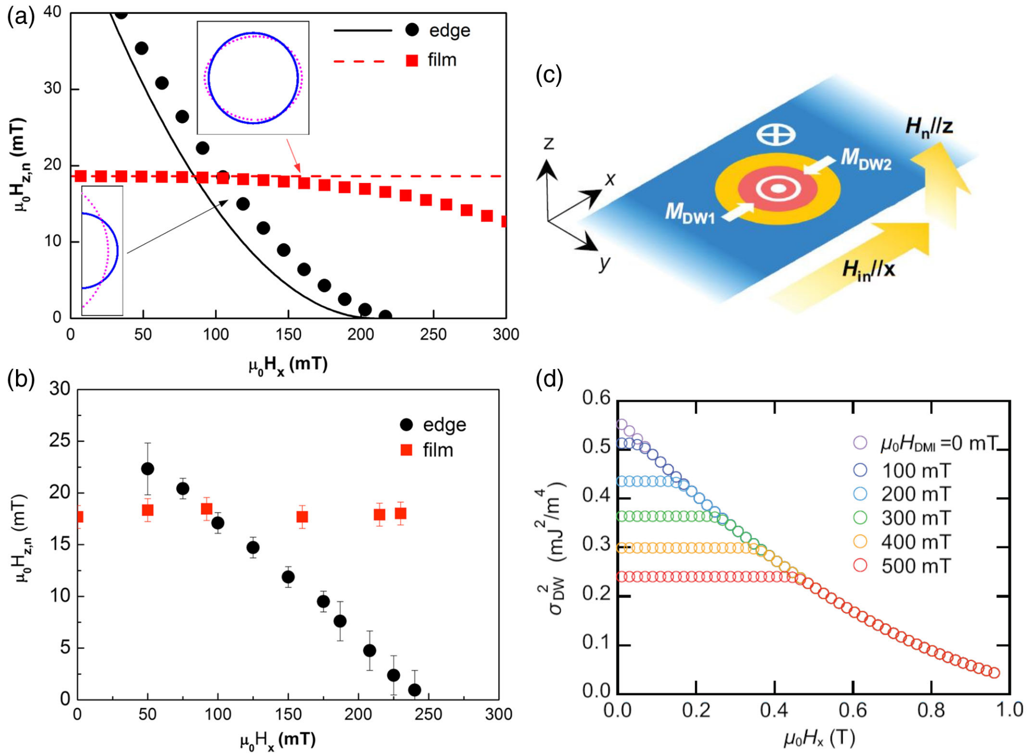

FIG. 11. (a) Theoretical nucleation field as a function of the magnetic field applied perpendicularly to the edge of the sample for edge and bubble (film) nucleation as a function of the field. (b) Experimental nucleation field as a function of the magnetic field applied perpendicularly to the edge for edge and bubble (film) nucleation. (c) Schematics of the nucleation of bubble domain (red area) showing the orientation of the wall core parallel and antiparallel to the applied field for in-plane fields below the DMI field. (d) Calculated domain-wall energy as a function of the in-plane field for different DMI fields. (a),(b) From Pizzini *et al.*, 2014. (c),(d) From Kim, Jang *et al.*, 2017.

reduced value of the bubble magnetic energy and an associated reduction of the nucleation field when the in-plane field value is increased beyond the DMI field. This was in agreement with their numerical calculations, as shown in Fig. 11(d). This fact was not observed by Pizzini *et al.* (2014) due to the large DMI field in the samples studied in their work.

Therefore, the critical field above which a change from a constant nucleation field to a field-dependent nucleation is observed is a measure of the DMI constant since it coincides with the DMI field H_{DMI}. Experimentally, this can be determined from the dependence of the out-of-plane nucleation field on the in-plane field.

6. Domain-wall stray fields

Another method taking into account the static DW structure is the direct measurement of the stray field in the DW. The stray field has a typical profile along the axis perpendicular to the DW, including information on the angle Φ and the strength and sign of D; see Fig. 12. This method is limited to low values of $D \leq D_{\mathrm{c}}$, i.e., when a significant angle is present. Here $D_{\mathrm{c}} = 2\mu_0 M_{\mathrm{S}}^2 d \ln 2/\pi^2$ is the critical D value above which formation of fully oriented Néel walls occurs (d is the film thickness). Therefore, only samples with relatively small D can be measured since D_{c} is typically on the scale of $0.2\ \mathrm{mJ/m^2}$; see Table XII. For samples with larger DMIs, where fully oriented Néel walls are present, only a lower limit of D can be given together with its sign (Tetienne *et al.*, 2015). Since DW widths are of the order of 5–10 nm, the stray field profile determination requires good spatial resolution, which was experimentally addressed using nitrogen-vacancy (NV) magnetometry (Gross *et al.*, 2016).

7. Domain-wall internal structure imaging

With progress in the development of advanced microscopy techniques with nanometric resolution and magnetic contrast, it has become possible not only to access the size and distribution of magnetic domains but also to study the detailed structure of domain walls. As previously discussed, the domain-wall structure is influenced by the presence of a DMI, so from a detailed identification of the wall structure one can in principle quantify the DMI strength. Basically four methods for spin sensitive imaging have been used in the literature: pioneering works were performed by SPSTM and spin-polarized scanning tunneling spectroscopy, the most quantitative works were done using SPLEEM, and in a few more recent works scanning electron microscopy with polarization analysis (SEMPA) and Lorentz transmission electron microscopy (LTEM) were employed.

Some of the earliest evidence indicating that the DMI influences domain-wall energies and alters DW configurations was obtained from SPSTM of ultrathin magnetic films deposited on heavy metal substrates such as single atomic layers of Mn or Fe on W(110) substrates (Bode *et al.*, 2007; Heide,

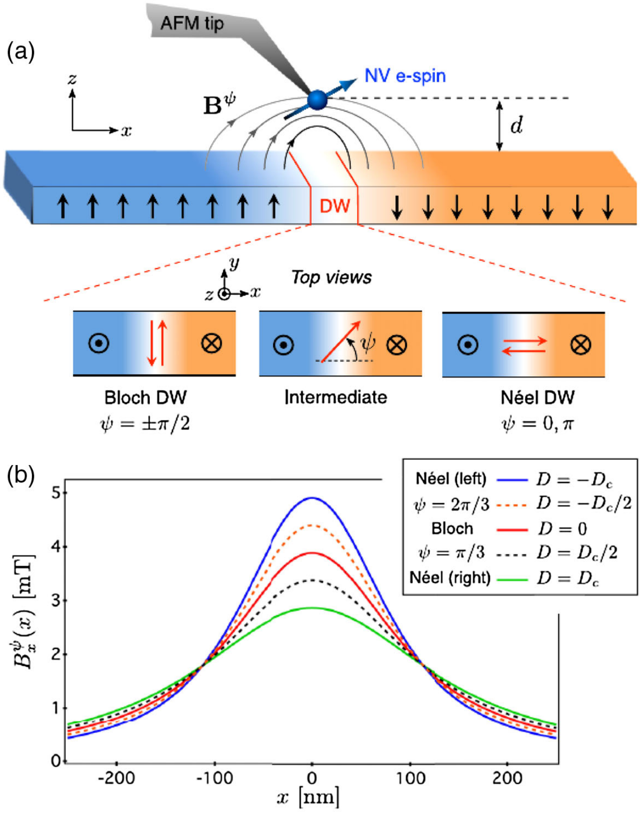

FIG. 12. Schematic of the stray field measurement using a NV magnetometer. The internal DW magnetization angle ψ (Φ in our notation) depends on the DMI constant, resulting in different profiles of the stray field component $B_x^\psi(x)$. From Gross *et al.*, 2016.

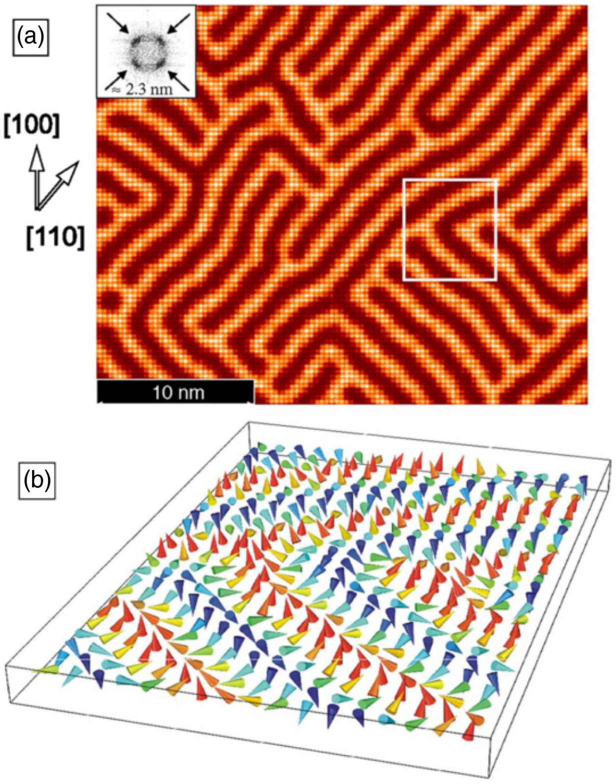

FIG. 13. (a) Simulations of SPSTM images based on Monte Carlo calculations (Heinze, 2006) of a monolayer of Mn on W(001) at 13 K. Inset: Fourier transform. (b) Detailed spin structure for the white square indicated in (a), where the helical spinstructure can be directly seen in the illustration. From Ferriani *et al.*, 2008.

Bihlmayer, and Blügel, 2008; Heinze *et al.*, 2011). These methods provide information on the magnetic order at the atomic scale. To extract the parameters entering the total energy of the observed noncollinear spin structures, such as the DMI constant, simulations of the images (see Fig. 13) based on models describing the tunneling process in the tip (Tersoff and Hamann, 1983) and density functional theory (DFT) were performed (Wortmann *et al.*, 2001). Since the computational cost of *ab initio* models is large, simplified approaches combining them with Monte Carlo or micromagnetic calculations were devised (Heinze, 2006; Heide, Bihlmayer, and Blügel, 2008). Successively using SPSTM Meckler, Gyamfi *et al.* (2009), Meckler, Mikuszeit *et al.* (2009), and Pietzsch and Wiesendanger (2011) concentrated on spin spiral domains in these bilayers and showed that the magnetic structure of the Fe double layer grown on W(110) is an inhomogeneous right-rotating cycloidal spin spiral. Meckler, Mikuszeit *et al.* (2009) extracted the magnitude of the Dzyaloshinskii-Moriya vector from the experimental data using analytical micromagnetic calculations. The result was then confirmed by a comparison of the measured saturation field along the easy axis to the respective value obtained from Monte Carlo simulations.

More recently SPLEEM has been successfully exploited to achieve a quantification of the DMI strength in different systems (Chen *et al.*, 2013, 2017, 2020; Chen, Ma *et al.*, 2013; Yang *et al.*, 2018). While first works give only an estimate of the DMI constant, a noteworthy development toward quantitative values has been observed in the literature. Here the HM thickness-dependent transition from chiral Néel walls to achiral Bloch walls is investigated in wedge samples. From the critical thickness a quantitative estimate of the DMI strength is obtained. In addition to SPSTM and SPLEEM, LTEM (Garlow *et al.*, 2019) and SEMPA (Corredor *et al.*, 2017; Kloodt-Twesten *et al.*, 2019; Meijer, Lucassen, Duine *et al.*, 2020) have also been used to quantify the DMI strength by comparing the measured and calculated profiles of the domain walls. In most cases micromagnetic analytical calculations or simulations of the DW energy or stray field are employed.

C. Experimental results

1. Current-driven domain-wall motion

Measurements of current-driven DW motion are performed in wires with typical widths ranging from 1 to 5 μm and lengths of a few tens of micrometers. Usually, the magnetization in the wire is initially saturated by applying an out-of-plane field H_z. H_z is then removed and a current pulse (with a duration of a few tens of nanoseconds) is applied directly either to the wire or to an Oersted line patterned atop the wire. In either case the current pulse nucleates a reversed magnetic domain and a DW is thus injected into the wire. Alternatively, one can use a magnetic-field pulse to generate domains in injection pads and inject them into the wires.

For measurements of DW velocities, current pulses are applied to the wire to move a DW, while the DW position along the wire is imaged using magneto-optical Kerr effect (MOKE) microscopy in a polar configuration. The number and duration of the applied current pulses is chosen to obtain a significant displacement of the DW, at least over a few micrometers. Typical values of current densities fall in a range of between 10^{10} and 10^{12} $\mathrm{A/m^2}$. The velocity of the DW is calculated as the ratio between the current-induced DW displacement and the total duration of the pulses. Finally, velocities are measured for both ↑↓ and ↓↑ DWs under different strengths of H_x, keeping the current density fixed, in order to determine the compensating field H_x^* of Fig. 4.

For measurements of DW depinning efficiencies, a constant current density J_e is applied continuously to the wire for a given in-plane field H_x, while the out-of-plane field H_z is ramped up until DW motion is detected using the MOKE. The DW depinning efficiency ϵ for a given H_x is then determined from the slope of the depinning field $H_{z,\mathrm{dep}}$ as a function of J_e. Modest current values of up to about 10^{10} $\mathrm{A/m^2}$ are used in order to exclude Joule heating effects. Finally, ϵ is measured for both ↑↓ and ↓↑ DWs under different strengths of H_x, and H_{DMI} is determined as the compensating field H_x^* for which $\epsilon = 0$.

Measurements of current-driven DW motion as a function of the in-plane field H_x have been used to extract H_{DMI} in several material stacks, with Co/Ni/Co, $\mathrm{Co_{20}Fe_{60}B_{20}}$, or Co as ferromagnetic films, different heavy metals as underlayers, and either heavy metals or oxides as overlayers. Tables I–III present a summary of the DMI values measured for Co/Ni/Co, CoFeB, and Co, respectively.

For Co/Ni/Co films (see Table I), the DMI seems to increase with the thickness of the Pt underlayer (Ryu *et al.*, 2013), while it is low when Pd or Ir is used as the underlayer (Ryu *et al.*, 2014).

For CoFeB films with Ta and MgO as the underlayer and over-layer (see Table II), the DMI values, generally small, are spread not only in magnitude but also in sign (Torrejon *et al.*, 2014; Lo Conte *et al.*, 2015; Karnad *et al.*, 2018). This can be explained by the fact that the two interfaces contribute with small and opposite DMI values, and that the DMI at the CoFeB/oxide interface strongly depends on its oxidation state. Furthermore, Karnad *et al.* (2018) found unexpectedly different signs of DMI for Ta/CoFeB/MgO, depending on whether they measured the DW motion driven by the current or the field; see Table V for the field-driven case). Among the underlayers used with CoFeB, W provided the highest positive DMI (Torrejon *et al.*, 2014).

Finally, for Co films, Pt was the only underlayer investigated, while overlayers were either oxides or metals; see Table III. In the symmetric structure Pt/Co/Pt, where no DMI is expected if the two interfaces are identical as experienced with epitaxial layers, either negative (Franken *et al.*, 2014) or vanishing (D.-Y. Kim *et al.*, 2018) DMI values were measured. This lack of perfect compensation depends on growth conditions, oxidation of the interfaces, and many other experimental conditions. For all the other stacks the DMI was always negative and was largest in magnitude when Ti was used as the overlayer (D.-Y. Kim *et al.*, 2018).

TABLE I. Overview of DMI fields for Co/Ni/Co thin films via current-induced domain-wall motion experiments. FM and NM stand for ferromagnetic and nonmagnetic layers, respectively. H_{DMI} is the DMI field, D is the interfacial DMI constant, and $D_s = Dd$, with d the thickness of the ferromagnetic film. Numbers in roman were quoted in the reviewed papers, while numbers in italics were either extracted from figures or calculated using the parameters provided.

FM (nm)	Bottom NM (nm)	Top NM (nm)	$\lvert\mu_0 H_{\mathrm{DMI}}\rvert$ (mT)	D ($\mathrm{mJ/m^2}$)	D_s (pJ/m)	Reference
Co(0.3)/Ni(0.7)/Co(0.15)	Pt(1)	TaN(5)	*60*			Ryu *et al.* (2013)
	Pt(1.5)		*190*			
	Pt(3)		*240*			
	Pt(5)		*220*			
Co(0.3)/Ni(0.7)/Co(0.15)	Pd(5)	TaN(5)	12			Ryu *et al.* (2014)
	Ir(3)		18			
	Pt(5)		140			

TABLE II. Overview of DMI measurements for CoFeB thin films via current-induced domain-wall motion experiments. FM and NM stand for ferromagnetic and nonmagnetic layers, respectively. H_{DMI} is the DMI field, D is the interfacial DMI constant, and $D_s = Dd$, with d the thickness of the ferromagnetic film. Numbers in roman were quoted in the reviewed papers, while numbers in italics were either extracted from figures or calculated using the parameters provided.

FM (nm)	Bottom NM (nm)	Top NM (nm)	$\lvert\mu_0 H_{\mathrm{DMI}}\rvert$ (mT)	D ($\mathrm{mJ/m^2}$)	D_s (pJ/m)	Sign	Reference
$\mathrm{Co_{20}Fe_{60}B_{20}}(1)$	Hf(2.6 – 6)	MgO(2)		*0.38–0.05*[a]	*0.38–0.05*[a]	−	Torrejon *et al.* (2014)
	Ta(0.5 – 1.3)			*0.08–0.07*[a]	*0.08–0.07*[a]	−	
	TaN(0.4 – 6.6)			*0.04–0.20*[a]	*0.04–0.20*[a]	+	
	W(2.1 – 3.6)			*0.24–0.37*[a]	*0.24–0.37*[a]	+	
$\mathrm{Co_{20}Fe_{60}B_{20}}(1)$	Ta(5)	MgO(2)	7.8	0.06	*0.06*	+	Lo Conte *et al.* (2015)
$\mathrm{Co_{20}Fe_{60}B_{20}}(0.8)$	Ta(5)	MgO(2)		0.03	*0.02*	−	Karnad *et al.* (2018)

[a] The highest and lowest DMI values reported do not necessarily correspond to the extremes of the bottom layer thickness range (for instance, the highest DMI value could occur in the middle thickness range).

TABLE III. Overview of DMI measurements for Co thin films via current-induced domain-wall motion experiments. FM and NM stand for ferromagnetic and nonmagnetic layers, respectively. H_{DMI} is the DMI field, D is the interfacial DMI constant, and $D_s = Dd$, with d the thickness of the ferromagnetic film. Numbers in roman were quoted in the reviewed papers, while numbers in italics were either extracted from figures or calculated using the parameters provided.

FM (nm)	Bottom NM (nm)	Top NM (nm)	$\lvert\mu_0 H_{\mathrm{DMI}}\rvert$ (mT)	D (mJ/m^2)	D_s (pJ/m)	Sign	Reference
Co(0.36)	Pt(4)	Pt(1)	37	*0.24*	*0.09*	−	Franken *et al.* (2014)
Co(0.36)	Pt(4)	Pt(2)	12.5	*0.10*	*0.04*	−	
Co(0.5)	Pt(4)	Pt(2)	11	*0.09*	*0.04*	−	
Co(0.5)	Pt(2)	Pt(4)	3	*0.03*	*0.02*	−	
Co(0.8)	Pt(4)	AlO$_x$(1.9)	≫40				
Co(1)	Pt(5)	Gd(2)	280	*1.00*	1.00	−	Vaňatka *et al.* (2015)
Co(0.93)	Pt(4)	AlO$_x$(2)	99	0.54	*0.50*	−	Lo Conte *et al.* (2017)
Co(1.31)			*54*	*0.48*	*0.63*	−	
Co(1.37)			*48*	*0.47*	*0.64*	−	
Co(0.9)	Pt(2.5)	Al(2.5)	107	0.87	*0.78*	−	D.-Y. Kim *et al.* (2018)
Co(0.9)		Ti(2.5)	*197*	1.42	*1.28*	−	
Co(0.9)		W(2.5)	*183*	1.35	*1.22*	−	
Co(0.5)		Pt(1.5)	0	0	0		

2. Field-driven domain-wall motion

Experiments of field-driven DW dynamics are mostly performed in continuous films where magnetization reversal proceeds by nucleation and growth of magnetic bubble domains. Only a few works have reported studies of planar DW dynamics (i.e., straight walls) in continuous films (Kim, Yoo *et al.*, 2017; Pellegren, Lau, and Sokalski, 2017) or in micrometer-wide wires (Jué *et al.*, 2016a; D.-Y. Kim *et al.*, 2018). The magnetization in the continuous film or wire is initially saturated by applying a perpendicular field H_z. A bubble domain (or a domain separated by a planar DW) is then nucleated by applying a short H_z pulse in the opposite direction, through either a coil or an electromagnet. The bubble domain (or the planar domain) is expanded under a simultaneous application of continuous H_x (from an electromagnet) and a pulsed or continuous H_z (from a coil or an electromagnet). The initial and final positions of the DW are imaged through MOKE microscopy in polar configuration, avoiding coalescence with other bubbles. The velocity of the DW is measured along the direction of the applied H_x and is calculated as the ratio between the DW displacement and the total time during which H_z is applied (whether in pulses or continuously). Finally, velocities are measured for both ↑↓ and ↓↑ DWs (i.e., DWs on opposite sides of the bubble) under different strengths of H_x upon keeping H_z constant. In this way velocity versus H_x curves are constructed for both DWs and H_{DMI} is determined through a fitting with one of the previously discussed modified creep formula (see Sec. II.B.2), or simply by finding the field for which the velocity is at minimum.

Regarding the strength of the applied fields, values differ greatly depending on the material and DW motion regime investigated. For measurements in the creep regime only modest $\mu_0 H_z$ are usually needed (a few millitesla depending on the depinning field, with some exceptions), while $\mu_0 H_z$ up to hundreds of millitesla can be required to drive DWs in the flow regime. The maximum values of applied $\mu_0 H_x$ instead depend on the strength of the DMI. In samples with a large DMI, in-plane fields of up to 350 mT have been used (Hrabec *et al.*, 2014; Lavrijsen *et al.*, 2015; Cao, Zhang *et al.*, 2018). However, since the use of in-plane fields can be accompanied by artifacts (for example, misalignments of the fields and crosstalk between perpendicular and in-plane electromagnets might be present), measuring large DMI values can be problematic. A simple scheme has been proposed to overcome the need for high H_x values (Kim, Yoo *et al.*, 2017), where the DW velocity is measured at an angle $\theta > 0$ with respect to the in-plane field direction. In this way, the minimum of the DW velocity scales by a factor $\cos\theta$ and also becomes measurable for samples with large DMIs by applying moderate in-plane fields.

Field-driven DW dynamics in the creep regimes have been investigated to extract H_{DMI} in material systems with Co/Ni multilayers, CoFeB or Co as ferromagnetic layers, and different combinations of heavy metals and oxides as underlayers and overlayers. Regarding the flow regime, H_{DMI} has been measured only for Co films, as shown in Table VII. Tables IV–VI present a summary of DMI measurements in the creep regime for Co/Ni, CoFeB, and Co, respectively. In the following we highlight some of the most noteworthy findings and observations of these experimental studies.

For Co/Ni multilayers (see Table IV), Yu, Qiu *et al.* (2016) studied the effect of different capping layers with a Pt underlayer and found values for D ranging from $D = 0.05$ mJ/m^2 ($D_s = 0.05$ pJ/m) for MgO to $D = 0.39$ mJ/m^2 ($D_s = 0.35$ pJ/m) for Ta. Separately, three works by the same group (Lau *et al.*, 2016, 2018; Pellegren, Lau, and Sokalski, 2017) reported on the asymmetry of DW velocity curves about their minima and on the crossover between DW velocities for the ↑↓ and ↓↑ sides of magnetic bubbles, corresponding to a morphological change from flattened to teardrop bubble shapes (Fig. 14). As previously mentioned, these velocity curves have been fitted through a model that takes into account both DW stiffness and a field-dependent prefactor v_0, showing that measurements of the minimum in velocity can be misleading to quantify the DMI (Lau *et al.*, 2018). The maximum value corresponds to an underlayer of Pt and a top layer of Ta/TaN with $D = 0.52$ mJ/m^2 ($D_s = 0.94$ pJ/m). The range of values are larger than in Yu, Qiu *et al.* (2016), but further analysis is needed to identify its origin.

TABLE IV. Overview of DMI measurements for Co/Ni multilayers via field-induced domain-wall motion experiments in the creep regime. FM and NM stand for ferromagnetic and nonmagnetic layers, respectively. H_{DMI} is the DMI field, D is the interfacial DMI constant, and $D_s = Dd$, with d the thickness of the ferromagnetic film. Numbers in roman were quoted in the reviewed papers, while numbers in italics were either extracted from figures or calculated using the parameters provided.

FM (nm)	Bottom NM (nm)	Top NM (nm)	$\lvert\mu_0 H_{\mathrm{DMI}}\rvert$ (mT)	D (mJ/m^2)	D_s (pJ/m)	Sign	Reference
$\mathrm{Co}(0.1)/[\mathrm{Ni}(0.1)/\mathrm{Co}(0.1)]_4$	Pt(4)	MgO(2)	15.59	0.05	*0.05*	−	Yu, Qiu *et al.* (2016)
		Cu(2)	19.23	0.12	*0.11*	−	
		Pt(2)	34.88	0.20	*0.18*	+	
		Ta(2)	103.86	0.39	*0.35*	−	
$[\mathrm{Co}(0.2)/\mathrm{Ni}(0.6)]_2/\mathrm{Co}(0.2)$	Pt(2.5)	Ta(0.5)/TaN(3)	60	*0.21*	*0.38*	−	Lau *et al.* (2016)
$[\mathrm{Co}(0.2)/\mathrm{Ni}(0.6)]_2/\mathrm{Co}(0.2)$	Pt(2.5)	Ta(0.5)/TaN(6)	106	*0.37*	*0.67*	−	Pellegren, Lau, and Sokalski (2017)
$[\mathrm{Co}(0.2)/\mathrm{Ni}(0.6)]_2/\mathrm{Co}(0.2)$	Pt(1.2)	Ta(0.8)/TaN(6)		*0.52*	*0.94*	−	Lau *et al.* (2018)
	Ir(1.2)	Ta(0.8)/TaN(6)		*0.07*	*0.13*	−	
	Pt(2.5)	Ir(2.5)		0.31	*0.56*	−	
	Ir(2.5)	Pt(2.5)		0.21	*0.38*	+	

TABLE V. Overview of DMI measurements for CoFeB thin films via field-induced domain-wall motion experiments in the creep regime. FM and NM stand for ferromagnetic and nonmagnetic layers, respectively. H_{DMI} is the DMI field, D is the interfacial DMI constant, and $D_s = Dd$, with d the thickness of the ferromagnetic film. Numbers in roman were quoted in the reviewed papers, while numbers in italics were either extracted from figures or calculated using the parameters provided.

FM (nm)	Bottom NM (nm)	Top NM (nm)	$\lvert\mu_0 H_{\mathrm{DMI}}\rvert$ (mT)	D (mJ/m^2)	D_s (pJ/m)	Sign	Reference
$\mathrm{Co}_{20}\mathrm{Fe}_{60}\mathrm{B}_{20}(0.8)$	Ta(5)	MgO(2)	*6.2–16.3*$^{\mathrm{a}}$	*0.02–0.06*$^{\mathrm{a}}$	*0.02–0.05*$^{\mathrm{a}}$	+	Khan *et al.* (2016)
CoFeB(1)	W(2)	MgO(2)	35	0.23	*0.23*	+	Soucaille *et al.* (2016)
	W(3)		15	0.12	*0.12*	+	
	TaN(1)		5	0.05	*0.05*	+	
	Hf(1)		2	0.01	*0.01*	+	
$\mathrm{Co}_{20}\mathrm{Fe}_{60}\mathrm{B}_{20}(0.6)$	W(5)	MgO(2)	93	0.68	*0.41*	+	Jaiswal *et al.* (2017)
$\mathrm{Co}_{40}\mathrm{Fe}_{40}\mathrm{B}_{20}(0.6)$		MgO(2)/Ta(5)	4	0.03	*0.02*	+	
$\mathrm{Co}_{20}\mathrm{Fe}_{60}\mathrm{B}_{20}(0.8)$	Ta(5)	MgO(2)	8.8	0.03	*0.02*	+	Karnad *et al.* (2018)
$\mathrm{Co}_{20}\mathrm{Fe}_{60}\mathrm{B}_{20}(1)$	Ta(5)	MgO(2)	2.6–16$^{\mathrm{b}}$	*0.02–0.08*$^{\mathrm{b}}$	*0.02–0.08*$^{\mathrm{b}}$	+	Diez *et al.* (2019b)

[a] Different DMI values correspond to different annealing temperatures.

[b] Different DMI values correspond to different doses of He$^+$ ion irradiation.

Regarding CoFeB films (see Table V), both the respective Co and Fe compositions (Jaiswal *et al.*, 2017) and the postgrowth annealing temperature (Khan *et al.*, 2016) have been shown to play a crucial role in the magnitude of the DMI. Furthermore, for low DMI values (namely, $D \lesssim 0.2$ mJ/m^2), the DW motion technique disagrees with the values obtained with Brillouin light scattering (BLS) (Soucaille *et al.*, 2016). Another noteworthy study was conducted by Diez *et al.* (2019b), who showed that the DMI can be tuned in a Ta/CoFeB/MgO system through light He$^+$ irradiation due to an increasing interface intermixing mostly between Ta and CoFeB layers.

Co is the most widely studied material, specifically in combination with Pt as the underlayer, which can provide high DMI magnitudes depending on the overlayer choice. DMI measurements performed in the creep regime (see Table VI) indicate that the nominally symmetric stack Pt/Co/Pt can have positive values of D_s as high as 0.58 pJ/m (Hrabec *et al.*, 2014), although the same work showed that upon ensuring epitaxial growth D_s reduces to almost 0. An even larger value of 0.71 pJ/m was calculated from the experimental data given by Hartmann *et al.* (2019).[10] Two more studies reported a vanishing DMI (Pham *et al.*, 2016; Ajejas *et al.*, 2017) for Pt/Co/Pt layers measured in the flow regime (see Table VII), while a small negative D_s was found by Shahbazi *et al.* (2018).

Another system widely investigated in the literature is the Pt/Co/Ir stack, which also gave rise to some controversial results. First principles calculations predicted the opposite DMI signs for the Pt/Co and Ir/Co interfaces, which would result in an additive effect for the Pt/Co/Ir stack (Yang *et al.*, 2015; Yamamoto *et al.*, 2017). However, Hrabec *et al.* (2014) showed that D decreases when a thin Ir top layer in a Pt/Co/Pt stack was introduced, and even changes sign with an increase in the Ir thickness. Similarly,

---

[10] In that paper the minimum velocity is found at $\mu_0 H_x \sim 50$ mT, a value compatible with other publications that report much smaller D and D_s values, such as those in Kim, Kim *et al.* (2015). The difference is the model used to evaluate D from the velocity minimum. Hartmann *et al.* (2019) calculated $\mu_0 H_{\mathrm{DMI}} \approx 170$ mT, resulting in a high value of $D_s = 0.71$ pJ/m.

TABLE VI. Overview of DMI measurements for Co thin films via field-induced domain-wall motion experiments in the creep regime. FM and NM stand for ferromagnetic and nonmagnetic layers, respectively. H_{DMI} is the DMI field, D is the interfacial DMI constant, and $D_s = Dd$, with d the thickness of the ferromagnetic film. Numbers in roman were quoted in the reviewed papers, while numbers in italics were either extracted from figures or calculated using the parameters provided.

FM (nm)	Bottom NM (nm)	Top NM (nm)	$\lvert\mu_0 H_{\mathrm{DMI}}\rvert$ (mT)	D (mJ/m^2)	D_s (pJ/m)	Sign	Reference
Co(0.3)	Pt(2.5)	Pt(1.5)	26.5	*0.11*	*0.03*	+	Je *et al.* (2013)
Co(0.7)	Pt(5)	Pt(3)	*104*	*0.83*	*0.58*	+	Hrabec *et al.* (2014)
		Ir(0.23)/Pt(3)	*10*	*0.08*	*0.06*	+	
		Ir(0.69)/Pt(3)	*155*	*1.23*	*0.86*	−	
Co(0.8)	Pt(10)	Pt(3)	50				Petit *et al.* (2015)
Co(0.4)	Pt(2)	Pt(2)	83	*0.33*	*0.13*	+	Kim, Kim *et al.* (2015)
	Pt(2)	Pd(2)	>200				
Co(0.6)	Pt(3)	AlO_x(1.6)	138				Kim, Yoo *et al.* (2017)
		MgO(2)	483				
Co(0.54)	Au(4)	NiO(10)		*2.04*	1.11	+	Kuświk *et al.* (2018)
Co(0.56)	Pt(4)	Ir(5)	*53*	*0.31*	*0.17*	−	Shepley *et al.* (2018)
Co(1.05)			*8.5*	*0.12*	*0.13*	−	
Co(1)	Pt(3)	MgO(0.65)/Pt(5)	*65.8*	0.77	*0.77*		Cao, Zhang *et al.* (2018)
		Mg(0.2)/MgO(1.5–2)/Pt(5)	*311*	2.32	*2.32*		
Co(1.8)	Pt(5)	W(1)/Pt(1)	25	0.19	*0.34*		Lin *et al.* (2018)
Co(0.6)	Pt(3)	Pt(3)	*7.8*	0.07	*0.04*	−	Shahbazi *et al.* (2018)
		$\mathrm{Pt}_{50}\mathrm{Au}_{50}$(3)	*48*	0.35	*0.21*	−	
		Au(3)	*175*	1	*0.6*	−	
Co(0.8)	Pt(2.2)	Ta(4)	*140*[a]	*1.12*[a]	*0.9*[a]	−	Shahbazi *et al.* (2019)
		Ir(0.2–2)/Ta(4)	*64.2–104.2*[b]	*0.49–0.93*[b]	*0.39–0.74*[b]	−	
Co(0.6)	Ta(4)/Pt(4)	Pt(4)	170	*1.20*	*0.71*	−[c]	Hartmann *et al.* (2019)
Co(0.8 − 1.2)		Gd(3)/Pt(2)	217–77	*0.43–0.23*	*0.34*	−[c]	
Co(0.8 − 1)		Ir(4)	156–92	*0.39–0.23*	*0.23*	−[c]	
Co(1)	Ta(4)/Pt(4)	Gd(3)/Pt(4)	280	0.37	*0.37*		Cao, van Hees *et al.* (2020)
Co(1)		Gd(3)/Ta(4)	255	0.24	*0.24*		
Co(1)/Gd(3)/Co(1)		Ta(4)	138	0.90	*0.45*		
Co(0.9)	Pt(5)	Pt(5)	0	0	0		Géhanne *et al.* (2020)
	Pt(5)	Au(5)	105	0.87	*0.78*	−	
	Au(5)	Pt(5)	78	0.59	*0.53*	+	

[a] For the Pt/Co/Ta system, the value provided is obtained while H_{DMI} is considered to be at the minimum in the velocity curves. However, the work estimates the DMI by also using a model that assumes $H_{\mathrm{dep}} = H_{\mathrm{dep}}(H_x)$. In this case $D = -2\,\mathrm{mJ/m^2}$ and $D_s = -1.6\,\mathrm{pJ/m}$.

[b] The highest and lowest DMI values reported do not necessarily correspond to the extremes of the Ir thickness range.

[c] The sign convention used here is the opposite of that used in the review.

Shahbazi *et al.* (2019) found that the magnitude of D was smaller in Pt/Co/Ir/Ta than in Pt/Co/Ta, suggesting that Pt/Co and Co/Ir interfaces contribute to the net DMI with opposite signs. On the other hand, a large increase in the DMI has been observed in Pt/Co/MgO layers upon the insertion of a thin Mg film between Co and MgO (Cao, Zhang *et al.*, 2018), providing among the highest values of $D_s = 2.32$ pJ/m ($D = 2.32$ mJ/m^2) reported in the literature.

All these results show how important the quality of the interfaces is for the determination the DMI. Perfect compensation is rarely obtained for nominally symmetric interfaces, and large variations are possible. The "controlled damage" of the interfaces by Ar^+ ion irradiation can even be an effective way to tune the sign of DMI in Pt/Co/Pt films (Balk *et al.*, 2017). The key aspect is the influence of the growth conditions on DMI, as was extensively investigated by Lavrijsen *et al.* (2015) and Wells *et al.* (2017). Both studies reported a dramatic variation of the DW velocity dependence with the in-plane field observed upon changing the sputter-deposition conditions, namely, Ar gas pressure, substrate temperature, or chamber base pressure. Indeed, it was speculated that such differing growth conditions may lead to different degrees of interfacial intermixing and/or quality, resulting in an expansive range of measured DMI values that can even change sign (Wells *et al.*, 2017).

3. Equilibrium stripe domain pattern

In the case of the equilibrium stripe domain pattern method, the DMI constant is estimated by measuring magnetic domain widths from nanometric magnetic microscopy images. The values and systems analyzed using this method are presented in Table VIII for CoFeB and Ni/Fe and

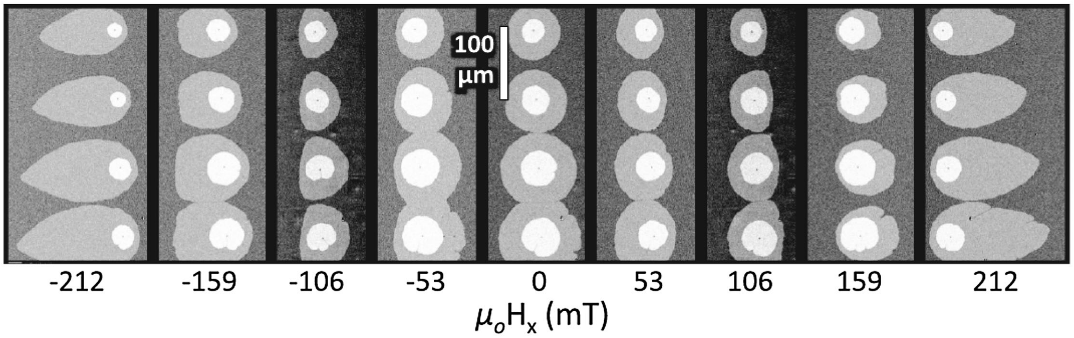

FIG. 14. Evolution of bubble domain shapes in an applied in-plane magnetic field in Co/Ni multilayers measured by the perpendicular Kerr effect. From Lau *et al.*, 2016.

in Table IX for Co and FeCo thin films. As the uncertainty of the measurement relies heavily on the precision of the imaging techniques, submicrometer range resolution is indispensable. The most commonly used experimental techniques for domain widths of several hundreds of nanometers are scanning transmission x-ray microscopy (STXM) (Moreau-Luchaire *et al.*, 2016; Lemesh *et al.*, 2018), magnetic transmission x-ray microscopy (MTXM) (Woo *et al.*, 2016, 2017), and magnetic force microscopy (MFM) (Büttner *et al.*, 2017; Soumyanarayanan *et al.*, 2017; Legrand *et al.*, 2018; Schlotter, Agrawal, and Beach, 2018; Agrawal *et al.*, 2019; Baćani *et al.*, 2019; Casiraghi *et al.*, 2019; Davydenko *et al.*, 2019; Dugato *et al.*, 2019; Kozlov *et al.*, 2020). In a few cases in which the domain width was close to 1 μm (or even larger), MOKE was the imaging technique used (Yu *et al.*, 2017; Wong *et al.*, 2018; Schott *et al.*, 2021). Most of the materials analyzed with this method have large DMI values (Moreau-Luchaire *et al.*, 2016; Woo *et al.*, 2016; Soumyanarayanan *et al.*, 2017). For example, Soumyanarayanan *et al.* (2017) reported that the replacement of the Co layer with a layer of FeCo substantially increases the value of D up to a maximum of $D_s = 2.18$ pJ/m for Fe(0.6 nm)/Co(0.6 nm). The maximum of D corresponds to $D = 2.1\ \mathrm{mJ/m^2}$ for a thinner magnetic layer Fe(0.4 nm)/Co(0.4 nm).

Many of the analyzed films are multilayers because the additional dipolar contribution between layers favors the stabilization of magnetic skyrmions (Moreau-Luchaire *et al.*, 2016). Legrand *et al.* (2018) studied the variation of the DW internal structure along the multilayer thickness due to the competition between the dipolar field and the DMI in Co multilayers. The domain walls in such structures have a hybrid character between Bloch and Néel types with different Néel chiralities at the bottom and top surfaces. Albeit being hybrid

TABLE VII. Overview of DMI measurements for Co thin films via field-induced domain-wall motion experiments in the flow regime. FM and NM stand for ferromagnetic and nonmagnetic layers, respectively. H_{DMI} is the DMI field, D is the interfacial DMI constant, and $D_s = Dd$, with d the thickness of the ferromagnetic film. The subscripts 1 and 2 indicate values of D and D_s extracted from H_{DMI} and v_{sat}, respectively. Numbers in roman were quoted in the reviewed papers, while numbers in italics were either extracted from figures or calculated using the parameters provided.

FM (nm)	Bottom NM (nm)	Top NM (nm)	$\lvert\mu_0 H_{\mathrm{DMI}}\rvert$ (mT)	D_1 (mJ/m^2)	D_2 (mJ/m^2)	D_{s1} (pJ/m)	D_{s2} (pJ/m)	Sign	Reference
Co(1)	Pt(5)	Gd(5)	180	1.48		1.48		−	Vaňatka *et al.* (2015)
Co(0.8)	Pt(4)	AlO$_x$(3)	220	1.63/1.91[a]		*1.3/1.53*[a]		−	Pham *et al.* (2016)
Co(1)		GdO$_x$(4)	200	1.48/1.73[a]		*1.48/1.73*[a]		−	
Co(1)		Gd(3)	300	1.52/1.78[a]		*1.52/1.78*[a]		−	
Co(1)		Pt(4)	0	0		0			
Co(0.6)	Pt(2)	Al(2)	200/212	*1.52/2.02*[b]	*1.38/2.2*[b]	0.91/1.21[b]	0.83/1.32[b]	−	Ajejas *et al.* (2017)
	Pt(2)	Ir(2)	96/125	*0.5/0.92*[b]	*0.37/0.67*[b]	0.3/0.55[b]	0.22/0.4[b]	−	
	Pt(2)	Cu(2)	200	*0.93*	*1.03*	0.56	0.62	−	
	Pt(2)	Pt(2)	0	0	0	0	0		
	Ir(2)	Pt(2)	106	*1.08*	*1.08*	0.65	0.65	+	
Co(0.8)	Pt(30)	AlO$_x$(1–3)			*1–1.79*[c]		0.8–1.43[c]	−	de Souza Chaves *et al.* (2019)
Co(1)	Pt(4)	GdO$_x$(1 − 3)	150–>260[c]	*0.6–1.42*[c]	*0.62–1.34*[c]	0.6–1.42[c]	0.62–1.34[c]	−	
Co(1)	Pt(4)	Gd(4)			1.45		*1.45*	−	Krizakova *et al.* (2019)
Co(1)		GdO$_x$(4)			1.5		*1.5*	−	
GdCo(4)		Ta			0.2		*0.8*	−	
GdCo(4.8)		Ta			0.2		*0.96*	−	

[a] The two reported values of DMI derive from two different values for the exchange constant A.
[b] The two values of DMI reported are due to different growth temperatures for the Co layer, either room temperature or 100 °C.
[c] The highest and lowest reported DMI values do not necessarily correspond to the extremes of the top NM thickness range.

TABLE VIII. Overview of DMI measurements for CoFeB and Ni/Fe thin films via the equilibrium stripe domain pattern. FM and NM stand for ferromagnetic and nonmagnetic layers, respectively. D is the interfacial DMI constant and $D_s = Dd$, with d the thickness of the ferromagnetic film. Numbers in roman were quoted in the reviewed papers, while numbers in italics were either extracted from figures or calculated using the parameters provided.

FM (nm)	Bottom NM (nm)	Top NM (nm)	$\vert D\vert$ (mJ/m^2)	$\vert D_s\vert$ (pJ/m)	Reference
$[\mathrm{Pt}(3)/\mathrm{Co}_{40}\mathrm{Fe}_{40}\mathrm{B}_{20}(0.8)/\mathrm{MgO}(1.5)]_{20}$	Ta(3)	Ta(2)	1.66	*1.33*	Woo *et al.* (2017)
$[\mathrm{Pt}(2.7)/\mathrm{Co}_{60}\mathrm{Fe}_{20}\mathrm{B}_{20}(0.8)/\mathrm{MgO}(1.5)]_{15}$	Ta(2.3)/Pt(3.7)		1.5	*1.2*	Büttner *et al.* (2017)
$\mathrm{Co}_{40}\mathrm{Fe}_{40}\mathrm{B}_{20}(1.2)$	Ta(5)	$\mathrm{TaO}_x(5)$	0.17	*0.2*	Yu *et al.* (2017)
Ni(6 − 12 MLs)/Fe(1 − 3 MLs)	(001)Cu			0.28 ± 0.14	Meier, Kronseder, and Back (2017)
Ni(9 MLs)/Fe(1 − 3 MLs)/Ni(4 − 14 MLs)				0	
Fe(1 ML)/Ni(6 − 12 MLs)				0.38 ± 0.14	
Fe(1 ML)/Ni(6 − 12 MLs)		Pt(0.4)		0.6 ± 0.2	
$\mathrm{Co}_{20}\mathrm{Fe}_{60}\mathrm{B}_{20}(1.2)$	MgO(1)	Ta(5)	0.65 ± 0.08	*0.78*	Wong *et al.* (2018)
$[\mathrm{Pt}(2.7)/\mathrm{CoFeB}(0.86)\mathrm{MgO}(1.5)]_{15}$	Ta(3.6)/Pt(1)	Pt(2.7)	1.76	*1.51*	Lemesh *et al.* (2018)
$[\mathrm{MgO}(2)/\mathrm{Co}_{20}\mathrm{Fe}_{60}\mathrm{B}_{20}(1)/\mathrm{Ta}(5)]_{15}$		Ta(5)	0.08 ± 0.03	0.08 ± 0.03	Casiraghi *et al.* (2019)
$[\mathrm{MgO}(2)/\mathrm{Co}_{20}\mathrm{Fe}_{60}\mathrm{B}_{20}(0.6)/\mathrm{W}(5)]_{15}$		Ta(5)	0.61 ± 0.03	0.37 ± 0.02	
$[\mathrm{MgO}(1.4)/\mathrm{Co}_{60}\mathrm{Fe}_{20}\mathrm{B}_{20}(0.8)/\mathrm{Pt}(3.4)]_{15}$	Ta(5.7)	Ta(5)	1.0 ± 0.1	0.80 ± 0.08	
$[\mathrm{Pt}(2.5-7.5)/\mathrm{Co}_{60}\mathrm{Fe}_{20}\mathrm{B}_{20}(0.8)/\mathrm{MgO}(1.5)]_{13}$	Ta(3)	Ta(2)	1.6 ± 0.2	*1.28*	Agrawal *et al.* (2019)

domain walls, the DMI can be extracted by comparing the measured domain width to the one obtained using micromagnetic simulations. With the same technique symmetric Pd/Co/Pd samples have also been analyzed (Davydenko *et al.*, 2019; Dugato *et al.*, 2019; Kozlov *et al.*, 2020). The origin of the DMI in such symmetric trilayers is a different residual stress in the top and bottom of the Co/Pd interfaces due to different lattice matching (Davydenko *et al.*, 2019). Dugato *et al.* (2019) were able to optimize the stack with the insertion of W between Co and Pd, resulting in an increase of D, with an optimal size for a W thickness of 0.2 nm and $D_s = 0.65$ pJ/m ($D = 1.3$ mJ/m^2). Kozlov *et al.* (2020) found a strong variation of the estimated D value, when values of the exchange constant in the range $A = 23$–30 pJ/m were used in the numerical model. The range of DMI for different exchange constants increases with an increase in the Co thickness.

Wedges of Ni on top a Fe layer with a Cu(001) substrate were analyzed using threshold photoemission magnetic circular dichroism with photoemission electron microscopy by Meier, Kronseder, and Back (2017). In these samples, the DMI originates at the Ni/Fe interface due to the lack of inversion symmetry, but the D values obtained are small because of the lack of a source of strong SOC. D increases when those bilayers are capped with a Pt layer. Using this method, the dependence of the DMI on temperature was also measured for Pt/Co/Cu multilayers up to a temperature of 500 K (Schlotter, Agrawal, and Beach, 2018). It was found that the DMI has a stronger dependence on temperature than other magnetic properties like magnetocrystalline anisotropy. Polar MOKE was used to measure the variation of D induced by electric fields in Pt(3 nm)/Co(0.49 nm)/AlO$_x$(6 nm) thin films (Schott *et al.*, 2021). The electric field was shown to induce variations of the magnetization, the anisotropy, and the DMI strength. For a field of 133 MV/m D changed by 0.14 (0.26) mJ/m^2, assuming an exchange constant of 7.5 (16) pJ/m.

4. Magnetic stripe annihilation

With this method, the first step is to nucleate two domain walls in a perpendicularly magnetized sample. The two walls are then manipulated with an out-of-plane field to minimize their distance until the two domain walls collapse. This annihilation field and the minimum width of the domain separating the walls before its collapse depend on D. The values of D extracted using this method are shown in Table X. As for the equilibrium stripe domain pattern technique (Sec. II.C.3), this method is based on magnetic imaging. For this purpose, MTXM (Jaiswal *et al.*, 2017; Litzius *et al.*, 2017), STXM (Woo *et al.*, 2016; Woo *et al.*, 2017), and the MOKE (Yu, Upadhyaya *et al.*, 2016) have been used. All the samples are continuous thin films or wide patterned tracks, to allow high number of domains and the manipulation of the walls. In the original study (Benitez *et al.*, 2015), the nucleated domain walls were parallel and were analyzed using a combination of LTEM and the polar Kerr effect. In later studies (Woo *et al.*, 2016; Yu, Upadhyaya *et al.*, 2016; Jaiswal *et al.*, 2017; Litzius *et al.*, 2017; Woo *et al.*, 2017), the annihilation field was studied independently of the shape and boundary of the domains. Benitez *et al.* (2015) measured a value for D of 0.33 mJ/m^2 ($D_s = 0.27$ pJ/m) in a Pt/Co/AlO$_x$ film, but they considered it a lower limit because of a possible underestimation of the annihilation field due to thermally activated processes. A DMI value of $D_s = 0.44$ pJ/m ($D = 0.73$ mJ/m^2) was measured in W/Co$_{20}$Fe$_{60}$B$_{20}$/MgO (Jaiswal *et al.*, 2017), while a smaller value of $D_s = 0.25$ pJ/m ($D = 0.25$ mJ/m^2) was obtained when the same composition was sandwiched between Ta layers (Yu, Upadhyaya *et al.*, 2016).

5. Nucleation field

A reversed domain is nucleated in a perpendicular magnetized material and the out-of-plane nucleation field as a function of the in-plane applied field is analyzed. The latter can be particularly large, up to 1 T as in Kim,

TABLE IX. Overview of DMI measurements for Co and FeCo thin films via the equilibrium stripe domain pattern. FM and NM stand for ferromagnetic and nonmagnetic layers, respectively. D is the interfacial DMI constant and $D_s = Dd$, with d the thickness of the ferromagnetic film. Numbers in roman were quoted in the reviewed papers, while numbers in italics were either extracted from figures or calculated using the parameters provided. This method does not provide the sign. All the D values are absolute values unless otherwise noted.

FM (nm)	Bottom NM (nm)	Top NM (nm)	D (mJ/m^2)	D_s (pJ/m)	Sign	Reference
$Co(0.6)/Pt(1)/[Ir(1)/Co(0.6)/Pt(1)]_{10}$	Pt(10)	Pt(3)	1.6 ± 0.2	*0.96*		Moreau-Luchaire *et al.* (2016)
$Co(0.6)/Pt(1)/[Co(0.6)/Pt(1)]_{10}$	Pt(10)	Pt(3)	0.2 ± 0.2	*0.12*		
$[Pt(3)/Co(0.9)/Ta(4)]_{15}$	Ta(3)		1.5 ± 0.2	*1.35*		Woo *et al.* (2016)
$[Ir(1)/Co(0.6)/Pt(1)]_{20}$	Ta(3)/Pt(10)	Pt(2)	*1.67*	*1*		Soumyanarayanan *et al.* (2017)
$[Ir(1)/Fe(0.2)/Co(0.6)/Pt(1)]_{20}$			*1.8*	*1.44*		
$[Ir(1)/Fe(0.3)/Co(0.6)/Pt(1)]_{20}$			*1.88*	*1.69*		
$[Ir(1)/Fe(0.2)/Co(0.5)/Pt(1)]_{20}$			*1.98*	*1.39*		
$[Ir(1)/Fe(0.4)/Co(0.4)/Pt(1)]_{20}$			*2.1*	*1.68*		
$[Ir(1)/Fe(0.4)/Co(0.6)/Pt(1)]_{20}$			*1.99*	*1.99*		
$[Ir(1)/Fe(0.5)/Co(0.5)/Pt(1)]_{20}$			*1.96*	*1.96*		
$[Ir(1)/Fe(0.6)/Co(0.6))/Pt(1)]_{20}$			*1.82*	*2.18*		
$[Ir(1)/Co(0.6)Pt(1)]_5$	Pt(10)	Pt(3)	2.30	*1.38*	+[a]	Legrand *et al.* (2018)
$[Ir(1)/Co(0.8)/Pt(1)]_5$	Pt(10)	Pt(3)	2.00	*1.6*	+[a]	
$[Co(0.8)/Ir(1)/Pt(1)]_5$	Pt(11)	Pt(3)	1.37	*1.1*	−[a]	
$[Co(0.8)/Ir(1)/Pt(1)]_5$	Ta(5)/Pt(10)	Pt(3)	1.63	*1.3*	−[a]	
$[Co(0.8)/Ir(1)/Pt(1)]_{10}$	Pt(11)	Pt(3)	1.52	*1.22*	−[a]	
$[Co(0.8)/Ir(1)/Pt(1)]_{10}$	Ta(5)/Pt(10)	Pt(3)	2.06	*1.65*	−[a]	
$Co(0.8)/[Pt(1)/Ir(1)/Co(0.8)]_{10}$	Ta(15)	Pt(3)	1.14	*0.91*	+[a]	
$[Pt(1)/Co(0.6)/Al_2O_3(1)]_{20}$	Ta(10)/Pt(7)	Pt(3)	1.29	*0.77*	−[a]	
$[Pt(1)/Co(0.8)/Al_2O_3(1)]_{20}$	Ta(10)/Pt(7)	Pt(3)	1.01	*0.81*	−[a]	
$[Al_2O_3(1)/Co(0.6)/Pt(1)]_{20}$	Ta(10)	Pt(7)	1.94	*1.16*	+[a]	
$[Al_2O_3(1)/Co(0.8)/Pt(1)]_{20}$	Ta(10)	Pt(7)	1.69	*1.35*	+[a]	
$[Pt(2)/Co(1.1)/Cu(1)]_{15}$	Ta(3)	Pt(2)	*1.55 (298 K)* *0.47 (423 K)*	*1.7* *0.52*		Schlotter, Agrawal, and Beach (2018)
$Co(0.6)/Pt(1)/[Ir(1)/Co(0.6)/Pt(1)]_5$	Pt(10)	Pt(3)	1.97 ± 0.02	*1.18*		Baćani *et al.* (2019)
$[Pt(2.5-7.5)/Co(0.8)/Pt(1.5)]_{13}$	Ta(3)	Ta(2)	0 ± 0.1	0		Agrawal *et al.* (2019)
$[Co(0.8)/Pd(2)]_5$	Cu(2)/Pd(3)	Pd(3)	1.6 ± 0.35[b]	*1.28*[b]	−[c]	Davydenko *et al.* (2019)
$[Co(0.8)/Pd(2)]_{10}$			1.85 ± 0.45[b]	*1.48*[b]	−[c]	
$[Co(0.8)/Pd(2)]_{20}$			2.3 ± 0.5[b]	*1.84*[b]	−[c]	
$[Pd(1)/Co(0.5)/Pd(1)]_{15}$			*0.3 ± 0.1*	0.15		Dugato *et al.* (2019)
$[Pd(1)/Co(0.5)/W(0.1)/Pd(1)]_{15}$			*1.1 ± 0.2*	0.55		
$[Pd(1)/Co(0.5)/W(0.2)/Pd(1)]_{15}$			*1.3 ± 0.2*	0.65		
$[Pd(1)/Co(0.5)/W(0.3)/Pd(1)]_{15}$			*0.4 ± 0.1*	0.2		
$[Pd(1)/Co(0.5)/W(1)/Pd(1)]_{15}$			*0.4 ± 0.1*	0.2		

[a] The sign was measured using circular dichroism in x-ray resonant magnetic scattering. The sign convention used here is the opposite of that used in the review.

[b] Values assuming $A = 20$ pJ/m. Other values are also assumed in the review.

[c] The negative sign of DMI is inferred from other experiments.

TABLE X. Overview of DMI measurements of Co and CoFeB thin films via magnetic stripe annihilation. FM and NM stand for ferromagnetic and nonmagnetic layers, respectively. D is the interfacial DMI constant and $D_s = Dd$, with d the thickness of the ferromagnetic film. Numbers in roman were quoted in the reviewed papers, while numbers in italics were either extracted from figures or calculated using the parameters provided.

FM (nm)	Bottom NM (nm)	Top NM (nm)	$\lvert D\rvert$ (mJ/m^2)	$\lvert D_s\rvert$ (pJ/m)	Reference
Co(0.8)	Pt(3)	$AlO_x(3)$	0.33 ± 0.05[a]	*0.27*[a]	Benitez *et al.* (2015)
$[Pt(3)/Co(0.9)/Ta(4)]_{15}$	Ta(3)		1.1 ± 0.2	*1*	Woo *et al.* (2016)
$Co_{20}Fe_{60}B_{20}(1)$	Ta(5)	Ta(0.74 − 0.9)	0.25	*0.25*	Yu, Upadhyaya *et al.* (2016)
$Co_{20}Fe_{60}B_{20}(0.6)$	W(5)	MgO(2)	0.73 ± 0.5	*0.44*	Jaiswal *et al.* (2017)
$[Pt(3)/Co_{40}Fe_{40}B_{20}(0.8)/MgO(1.5)]_{20}$	Ta(3)	Ta(2)	1.35	*1.08*	Woo *et al.* (2017)
$[Pt(3.2)/CoFeB(0.7)/MgO(1.4)]_{15}$	Ta(3)		1.35 ± 0.05	*0.95*	Litzius *et al.* (2017)

[a] Lower limit.

Jang *et al.* (2017). This type of measurement can be divided in two groups: edge nucleation in patterned wires (Pizzini *et al.*, 2014) or asymmetric microstructures (such as triangles) (Han *et al.*, 2016) and bubble nucleation in extended films (Kim, Jang *et al.*, 2017; S. Kim *et al.*, 2018). In all the experiments, the magnetic images were obtained using the MOKE. Han *et al.* (2016) found that the hysteresis loop of asymmetric microstructures measured using wide-field polar Kerr effect shows an asymmetry due to a DMI similar to exchange biasing. This asymmetry is attributed to the asymmetric nucleation when an in-plane field is present and is independent of the structure size. The values obtained for D are presented in Table XI, consisting mostly of single layers of Co (Pizzini *et al.*, 2014; Han *et al.*, 2016; S. Kim *et al.*, 2018) or trilayers of Co/Ni/Co (Kim, Jang *et al.*, 2017). Pizzini *et al.* (2014) obtained a value of $D_s = -1.32$ pJ/m ($D = -2.2$ mJ/m^2) for Pt/Co/AlO$_x$. Han *et al.* (2016) measured the opposite sign for the reversed structure AlO$_x$/Co/Pt with a value of $D_s = 1.62$ pJ/m ($D = 1.43$ mJ/m^2). When the structure was reversed and the AlO$_x$ was replaced by Ir, a value of $D_s = -2.03$ pJ/m ($D = -1.69$ mJ/m^2) was measured, indicating opposite contributions for Pt and Ir. This method was used to obtain the value of D as a function of temperature in a Co layer (S. Kim *et al.*, 2018), obtaining a decrease from 1.18 mJ/m^2 at 100 K to 0.48 mJ/m^2 at 300 K.

6. Domain-wall stray fields

In NV magnetometry, the value of D is obtained by measuring the magnetic stray field generated by a 180° Bloch wall in PMA materials (Tetienne *et al.*, 2015; Gross *et al.*, 2016). The NV magnetometer measures the Zeeman shift in the electronic spin sublevels of a NV defect in a diamond crystal in the presence of a small magnetic field. The diamond nanocrystal is placed on the tip of an atomic force microscope and scanned across the DW at a distance of about 100 nm from the surface; see Fig. 12. The Zeeman shift is proportional to the projection of the external magnetic stray field (arising from the domains adjacent to the wall in the case of a Bloch wall, and of the domains adjacent to the wall and the wall itself in the case of a Néel wall) on the quantization axis of the NV center (B_{NV}). Therefore, Bloch and Néel walls can be easily distinguished from the Zeeman shift profile perpendicular to the wall. Since the stray field depends on several parameters, such as the distance from the surface M_{S} and the DW width, any error in these values reflects in an uncertainty of D. The main source for uncertainty is usually considered to arise from A, the exchange stiffness, but also from inhomogeneities in M_{S} or thickness variations.

7. Domain-wall internal structure imaging

Bode *et al.* (2007) used the SPSTM technique to investigate the role of the DMI in systems with a chiral spin structure. The specific chirality of the moments in single atomic layers of Mn on a W(110) substrate was observed directly, and the different energy contributions of the cycloid structure were calculated by employing DFT with a generalized gradient approximation and full-potential linearized augmented plane waves. The long-range homogeneous spiral structure was accounted for by the generalized Bloch theorem, with spin-orbit coupling added as a perturbation. The SPSTM experiments (see the

TABLE XI. Overview of DMI measurements of Co and Co/Ni thin films via nucleation field dependence. FM and NM stand for ferromagnetic and nonmagnetic layers, respectively. H_{DMI} is the DMI field, D is the interfacial DMI constant, and $D_s = Dd$, with d the thickness of the ferromagnetic film. Numbers in roman were quoted in the reviewed papers, while numbers in italics were either extracted from figures or calculated using the parameters provided. Edge nucleation provides the D sign, while bubble nucleation provides only the magnitude. Values with an asterisk are in accord with the convention used in this review and are the opposite of that in the original manuscript.

FM (nm)	Bottom NM (nm)	Top NM (nm)	$\lvert\mu_0 H_{\mathrm{DMI}}\rvert$ (mT)	D (mJ/m^2)	D_s (pJ/m)	Sign	Nucleation type	Reference
Co(0.6)	Pt(3)	AlO$_x$(2)		2.2*	*1.32**	−	Edge	Pizzini *et al.* (2014)
Co(1.15)	AlO$_x$(2.5)	Pt(4)		1.43* ± 0.06	1.62* ± 0.07	+	Edge	Han *et al.* (2016)
Co(1.2)	Pt(4)	Ir(4)		1.69* ± 0.03	2.03* ± 0.04	−		
Co(0.3)/Ni(0.6)/Co(0.3)	Pt(2)	MgO(1)	228 ± 60	0.45 ± 0.15	*0.54*		Bubble	Kim, Jang *et al.* (2017)
Co(0.5)	Pt(2)	MgO(2)	372 ± 30	*1.18*	*0.59*		Bubble (100 K)	S. Kim *et al.* (2018)
			324 ± 15	*1.03*	*0.52*		Bubble (150 K)	
			245 ± 45	*0.75*	*0.37*		Bubble (200 K)	
			166 ± 50	*0.48*	*0.24*		Bubble (300 K)	

TABLE XII. Overview of DMI measurements of CoFeB thin films by stray field using NV magnetometry. FM and NM stand for ferromagnetic and nonmagnetic layers, respectively, D is the interfacial DMI constant, and $D_s = Dd$, with d the thickness of the ferromagnetic film. Numbers in roman were quoted in the reviewed papers, while numbers in italics were either extracted from figures or calculated using the parameters provided.

FM (nm)	Bottom NM (nm)	Top NM (nm)	D (mJ/m^2)	D_s (pJ/m)	Sign	Reference
Co$_{40}$Fe$_{40}$B$_{20}$(1)	Ta(5)	MgO(2)	0 ± 0.01	*0 ± 0.01*		Gross *et al.* (2016)
Co$_{20}$Fe$_{60}$B$_{20}$(1)	TaN$_{0.7\%}$(4)		0.03 ± 0.01	*0.03 ± 0.01*	+	
	TaN$_{0.7\%}$(1)		0.06 ± 0.02	*0.06 ± 0.02*	+	

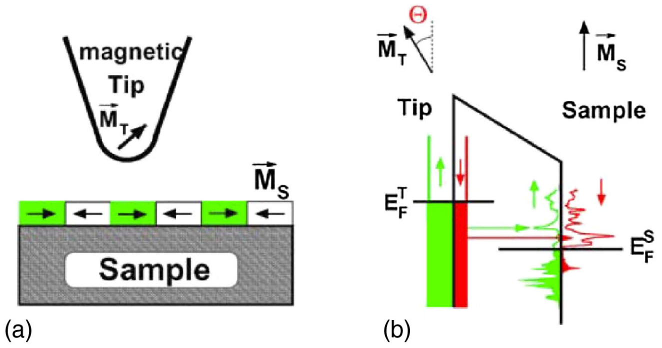

FIG. 15. Schematics of spin-polarized scanning tunneling microscope using a magnetically coated scanning tunneling microscope tip. (a) Geometry of the experimental setup including the magnetization axes of tip $\mathbf{M}_T$ and sample $\mathbf{M}_S$. (b) Electronic structure of the tip and sample. In the case of a perfect parallel alignment of $\mathbf{M}_T$ and $\mathbf{M}_S$, only majority electrons can tunnel into unoccupied majority states, and only minority electrons can tunnel into unoccupied minority states. From Heinze, 2006.

scheme in Fig. 15) were performed in ultrahigh vacuum at $T = 13 \pm 1$ K in constant current mode. For spin resolved measurements Cr- and Fe-covered W tips were used. The tunneling current I is sensitive to the relative orientation of the magnetization of the tip ($\mathbf{M}_T$) and the sample ($\mathbf{M}_S$), according to $I = I_0 + I_{sp}\mathbf{M}_T \cdot \mathbf{M}_S$, where I_{sp} is the spin-polarized part of I. This allows for an atomic scale imaging of magnetic nanostructures (Heinze, 2000). This work was continued by Ferriani *et al.* (2008) and yielded a nearest-neighbor DMI of 4.6 meV and $D_s = 2.33$ pJ/m, with an approximate lattice constant of that of W (3.165 Å). Heinze *et al.* (2011) studied Fe monolayers on Ir(111) and found similar values. Double layers of Mn were studied by Yoshida *et al.* (2012), and Fe islands on Cu(111) were studied by Fischer *et al.* (2017). Similar studies exploiting SPSTM were also presented by Meckler, Mikuszeit *et al.* (2009), who found that the DMI is too weak to destabilize the single domain state, but that it can define the sense of rotation and the type of the cycloidal spiral once the single domain state is destabilized by the dipolar interaction. More recent SPSTM studies were completed by Hsu *et al.* (2018), who investigated the effect of loading double layers of Fe with hydrogen, by Perini *et al.* (2018), who studied epitaxial films of Co/Ir(111) and Pt/Co/Ir(111) by making use of DFT and showed that in the latter the DMI comes almost only from the interface with Pt, and by Romming *et al.* (2018), who studied Rh/Fe atomic bilayers on Ir(111) by showing that higher-order exchange interactions may compete with interfacial DMIs.

In addition to the previously mentioned results obtained with SPSTM, the SPLEEM technique has also yielded a number of quantitative studies of DMIs in layered systems. In this experimental approach, spin-polarized, low-energy electrons are projected toward the sample surface through an illumination column and reach the sample at normal incidence (Rougemaille and Schmid, 2010). A magnetic beam splitter is exploited to separate the incoming electrons from the backscattered ones, and a magnified image of the magnetic surface is obtained by passing the backscattered beam through an imaging column similar to that found in electron microscopes (a schematic is shown in Fig. 16). This technique is extremely surface sensitive since it employs electrons of few eV energy that do not penetrate more than a few atomic layers, while the lateral resolution is of the order of several nanometers. Therefore, SPLEEM requires *in situ* analysis of samples prepared in ultrahigh vacuum, and it is usually not suitable for samples prepared elsewhere. By a careful comparison of SPLEEM images on films of different thicknesses, the film-thickness-dependent transition from chiral Néel walls (dominated by the DMI) and nonchiral Bloch walls (dominated by the stray field) can be directly analyzed, so one can quantify the DMI relying on the fact that the DMI energy and the stray field energy are comparable near the transition thickness. Thus, the DMI strength can be quantified by calculating the stray field energy for a wall structure with a given film thickness. This approach has been followed in a number of quantitative studies that are collected in Table XIII.

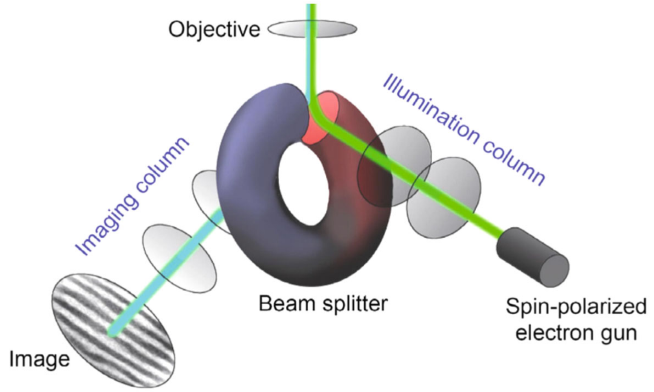

FIG. 16. Schematics of a SPLEEM microscope. Spin-polarized electrons, photoemitted from a GaAs photocathode, are injected into a spin manipulator where azimuthal and polar orientation of the polarization is adjusted. The electron beam then passes through an illumination column before being decelerated in the objective lens. Electrons finally hit the surface with normal incidence. Electrons that are backscattered elastically are collected in an imaging column and focused on a phosphorous screen, where a magnified image of the surface is obtained. The incoming and reflected electron beams are separated in a magnetic beam splitter using the Lorentz force. From Rougemaille and Schmid, 2010.

As for Lorentz TEM microscopy, it was exploited to derive the value of the DMI (Garlow *et al.*, 2019) looking at the mixed Bloch-Néel chiral spin textures in Co/Pd multilayers. An analysis of the observed intensities under varied imaging conditions coupled to corroborative micromagnetic simulations permitted different magnetic parameters, including the domain-wall width, the exchange stiffness, and the DMI, to be quantified. Finally, SEMPA was also used to quantify the DMI in thin film systems. For instance, Corredor *et al.* (2017), using the experimentally determined wall angle and width parameter, derived a span for the DMI strength of $0.8\ \mathrm{meV/Co} < d < 4.3\ \mathrm{meV/Co}$, which was in agreement with previous *ab initio* calculations for this system. In addition, in a recent SEMPA study of $\mathrm{Fe_3GeTe_2}$ films (Meijer, Lucassen, Duine *et al.*, 2020) a lower bound of $D > 0.09-0.2\ \mathrm{mJ/m^2}$ for the DMI term was found. A more refined and quantitative result was achieved by Kloodt-Twesten *et al.* (2019), who studied the domain-wall profiles of Co/Ir(111) films as a function of Co thickness using SEMPA. They found that below a cobalt thickness of 8.8 MLs, the magnetic domain walls are purely Néel oriented and show a clockwise sense of rotation. For larger thicknesses the plane of rotation changes and the domain walls show a significant Bloch-like contribution, allowing one to calculate the strength of the DMI from energy minimization. In particular, from the angle between the plane of rotation and the domain-wall normal $D_s = -1.07 \pm 0.05$ pJ/m was determined (in our convention a clockwise sense of rotation corresponds to a positive value of the DMI, and we have thus adopted the positive sign in Table XIII).

The pioneering approach of these methods was among the first allowing an experimental determination of the DMI and directly observing its influence on the magnetic structure. Therefore, the area remained active and substantial progress toward a quantitative determination of the DMI was achieved; see Table XIII.

D. Advantages and limitations

In general, methods based on domain walls require an accurate estimation of several magnetic parameters in order to evaluate the interfacial DMI; see Eq. (2.1). Among these, the exchange stiffness A, which enters into the expressions of both the DMI field and the DW energy, is notoriously difficult to measure for ultrathin films leading to an uncertainty in the quantification of D. Han *et al.* (2016) pointed out that in the nucleation method a variation of A from 5 to 15 pJ/m for Co results in a 25% difference for D obtained using the intermediate value 10 pJ/m. This is not the case for methods based on spin waves (see Sec. III), where A is not needed to extract the interfacial DMI. Furthermore, methods that rely on domain walls can be applied to measure D only in perpendicularly magnetized materials, while methods based on spin waves (see Sec. III) are also able to quantify D for systems with in-plane magnetization. We later review the main strengths and weaknesses of all methods discussed in this section.

Measurements of both current-driven and field-driven DW dynamics in the presence of an in-plane magnetic field allow one to quantify not only the magnitude of D but also its sign, which gives information on the DW chirality. On the other hand, in the creep regime, the dependence of the DW velocity on the in-plane field does not always follow the simple linear dependence when it is driven by the current (see Fig. 4), or the symmetric shape with a well-defined minimum in the field-driven case (see Fig. 7). Deviations from these simple theoretical predictions are in fact quite common (see Fig. 8 for an example), and there is no consensus on a general model able to predict and fit all the observed cases. Several models predict that the minimum velocity does not correspond to the

TABLE XIII. Overview of DMI measurements by domain-wall internal structure imaging. The measurements from Chen *et al.* (2013, 2017, 2020), Chen, Ma *et al.* (2013), and Yang *et al.* (2018) were performed using SPLEEM, those from Meckler, Mikuszeit *et al.* (2009) were completed using SPSTM, those from Garlow *et al.* (2019) were performed using LTEM, and those from Kloodt-Twesten *et al.* (2019) were completed using SEMPA. FM and NM stand for ferromagnetic and nonmagnetic layers, respectively, D^* is the DMI value given in meV/atom, D is the interfacial DMI constant, and $D_s = Dd$, with d the thickness of the ferromagnetic film. Thicknesses are given in either nanometer or atomic monolayers (MLs). Numbers in roman were quoted in the reviewed papers, while numbers in italics were either extracted from figures or calculated using the parameters provided. Signs with $*$ are in accord with the convention used in this review and are the opposite of that in the original manuscript.

FM	Bottom NM	Top NM	D^* (meV/atom)	D (mJ/m^2)	D_s (pJ/m)	Sign	Reference
Fe(1.7 MLs)	(110)W				1.2	+*	Meckler, Mikuszeit *et al.* (2009)
Ni(2 MLs)/Fe(2.5 MLs)	(001)Cu		0.12–0.17	0.08–0.12		−	Chen *et al.* (2013)[a]
Ni(2 MLs)/[Co(1 ML)/Ni(2 MLs)]$_2$	(111)Pt		1.05	0.44		−	Chen, Ma *et al.* (2013)[a]
	(111)Ir		0.12	0.14		+	
	(111)Pt/Ir(0.6 − 3 MLs)		0.47–0.12	0.28–0.14		from − to +	
Ni(15 MLs)/Fe(3.3 MLs)	(110)W		0.53	0.32		+	Chen *et al.* (2017)[a]
Co(2.4 MLs)	(0001)Ru		0.05	0.18		+	Yang *et al.* (2018)[a]
Co(3.9 − 8.4 MLs)		Graphene	0.11	0.25		−	
Co(0.7 nm)[Pd(0.5 nm)/Co(0.7 nm)]$_{10}$	MgO(2 nm)/Pt(4 nm)	Pt(4 nm)		1.05			Garlow *et al.* (2019)
Co(3.5 − 9.7 MLs)	(111)Ir				1.07	+*	Kloodt-Twesten *et al.* (2019)
Co(3 ML)/Ni(2 ML)/[Co(1 ML)/Ni(2 ML)]$_8$	(111)Pd		1.44	0.54		−	Chen *et al.* (2020)[a]
Co(3 ML)/Ni(1 ML)	(110)W/Pd(2.6 MLs)	O(0.2 ML)	0.63	0.4		+	
Co(3 MLs)/Ni(1 ML)	(110)W/Pd(2.1 MLs)	H(0.6 ML)	0.01	0.01		+	Chen *et al.* (2021)[a]

[a] The values for D given in mJ/m^2 were provided by the authors of the original paper. In some cases the sign or thickness values were corrected with respect to the original work.

DMI field, but agreement on its calculation is still missing and can lead to a significantly different determination of the D value. The main reason for this is that a full and general microscopic description of the domain-wall dynamics is still under investigation. While some systems seem to follow the quenched Edwards-Wilkinson equation (Grassi *et al.*, 2018; Albornoz *et al.*, 2021), there is also experimental evidence that other systems are better described by a quenched–Kardar-Parisi-Zhang equation having different exponents and critical dynamics. The consequences on the DMI estimation of these two universality classes are still unknown.

Overall, current-driven DW motion is a more complex technique to determine the interfacial DMI, both for the experimental realization and for an interpretation of the results. A standard lithography process is required to pattern films into wires of appropriate geometry, and high in-plane fields (especially for samples with a large DMI) need to be applied and properly aligned. Furthermore, the torque generated by large applied currents can also result in a tilt of the DW (Emori *et al.*, 2014). Concerning the interpretation of the results, a clear definition of H_{DMI} might be hard due to the interplay present in complex systems between different current-induced spin torques (STT, SHE SOT, ISGE torque), whose collective effect on DW dynamics is still not fully understood.

Field-driven DW motion has the advantage of being a relatively simple method to implement experimentally, as it allows the measurement of interfacial DMI in continuous films without the need for any lithographic patterning. However, the application of high in-plane fields, particularly for samples with a significant DMI, requires a perfect alignment of the in-plane field, with no out-of-plane components. Indeed, in the creep regime any unwanted component of the field perpendicular to the sample plane would influence the DW velocity in an exponential manner; see Eq. (2.5). Several precautions should be taken into account to achieve an optimal alignment of the in-plane field (Je *et al.*, 2013; Lavrijsen *et al.*, 2015; Soucaille *et al.*, 2016; Cao, Zhang *et al.*, 2018). A perpendicular stray field component may still arise in MOKE setups due to the crosstalk between in-plane and perpendicular electromagnets or due to not completely nonmagnetic objectives, which would alter the field distribution in a manner that is difficult to account for.

Regarding measurements of DW velocities in the flow regime, the main difficulty there lies in the generation of large and short magnetic-field pulses. The determination of the DMI constant from the Walker DW velocity (or the saturation velocity after the Walker field) does not require knowledge of the exchange constant [see Eq. (2.10)] but, on the other hand, may not be accessible when hidden in the creep regime.

Among the methods that are based on the DW energy to evaluate the interfacial DMI, imaging the equilibrium stripe domain pattern is particularly straightforward due to its experimental simplicity. Indeed, this method is compatible with a magnetic imaging technique like Kerr microscopy or MFM (which has to be chosen according to the expected domain width) and does not require the application of perpendicular or in-plane fields. On the other hand, imaging the equilibrium domain configuration does not provide information on the sign of D. For multilayer samples with a large DMI, small A, or any situation that yields small values of the left-hand side of Eq. (2.12), high-resolution imaging is needed to precisely resolve the small domain widths. In patterned systems, the domain-wall width, the domain size, and the configuration may depend on the geometry, due to confinement and dipolar effects, adding discrepancies with respect to analytical formulations. Other disadvantages include the fact that the simple analytical model to extract D may not work for overly thick samples that yield neither Néel nor Bloch wall types (hybrid wall with Néel caps and Bloch core), although the DMI is expected to be low in these systems.

From the experimental point of view, the measured domain widths may differ for samples demagnetized with in-plane and out-of-plane fields up to 20% (Legrand *et al.*, 2018; Davydenko *et al.*, 2019; Kozlov *et al.*, 2020). For this reason, the in-plane demagnetized configuration is preferred, as it is closer to the parallel stripes described by the initial analytical theories, while the real domain configuration may consist of rounded meandering structures. In principle, these problems may be solved using the proper theoretical model. Moreover, refined expressions for the DW energy may yield slightly different values for the DMI (Lemesh, Büttner, and Beach, 2017). This disagreement in the modeling complicates the extraction of DMI and the interpretation of the experimental results.

Similar considerations hold for the method based on magnetic stripe annihilation. Here too it is possible to extract information only on the absolute value of D not on its sign. From an experimental point of view, the original application of this technique requires the presence of parallel DWs, a condition that may not apply to the case of materials with irregular wall profiles. Another drawback is that, as the domain walls are closer together, the corresponding energy barrier for thermally induced domain-wall annihilation is reduced and is also affected by the presence of defects, which can yield an error in the determination of the DMI value.

Since it relies on the nucleation of a reversed domain, the process of bubble nucleation to extract the interfacial DMI is intrinsically a statistical process, and several repetitions of the same experiment need to be carried out to achieve a reliable measurement of the nucleation field. In contrast, imaging the equilibrium domain configuration in a film can automatically provide averaged information of the domain width, from which the DMI is quantified if a large enough area is imaged. Bubble nucleation experiments can be performed both at the edge of patterned structures, such as nucleation pads or wires, and in continuous films. In the former case, the method can be used to determine both the absolute value of D and its sign. Specifically, the sign of D is related to the nucleated bubble position with respect to the direction of the applied in-plane field. On the other hand, bubble nucleation measurements in continuous films provide only the absolute value of D.

Concerning the methods based on domain and domain-wall imaging, it has been shown in different magnetic systems (see Table XIII) that SPSTM and SPLEEM (and, to a lesser extent, SEMPA and LTEM) can be used to achieve a quantitative estimation of the DMI strength, looking at the domain structure or at the transition from Néel to Bloch wall as a function of thickness. One should consider that SPSTM and SPLEEM require a complex apparatus with ultrahigh vacuum

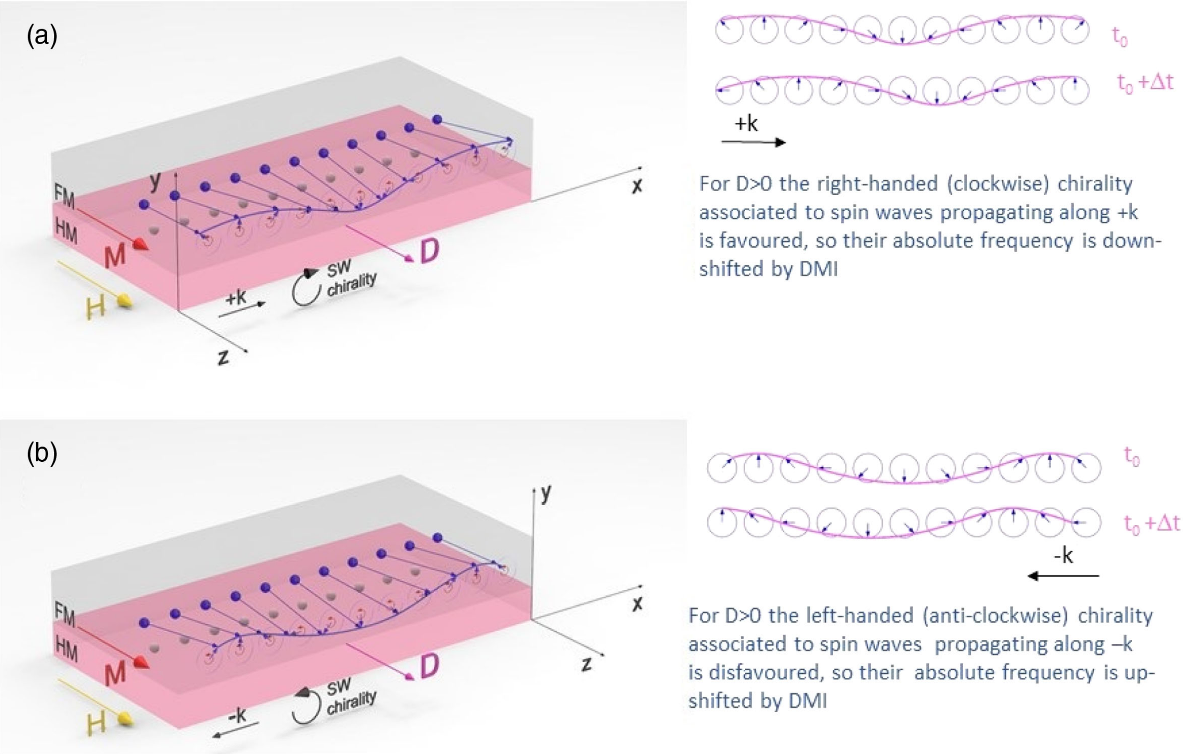

For D>0 the right-handed (clockwise) chirality associated to spin waves propagating along +k is favoured, so their absolute frequency is down-shifted by DMI

For D>0 the left-handed (anti-clockwise) chirality associated to spin waves propagating along –k is disfavoured, so their absolute frequency is up-shifted by DMI

FIG. 17. (a) Sketch of a spin wave in the Damon-Eshbach configuration propagating toward the positive x direction, with a $+k$ wave vector, in the FM film. All the individual magnetic moments (blue arrows) are precessing counterclockwise around the z axis, i.e., around the direction of the static magnetization and of the external field H. Owing to the phase delay from one spin to the next (moving from left to right), the chirality associated with the SW is clockwise, that is, favored by a positive DMI (magenta D vector). In thin bilayer FM/HM films, the latter couples two neighboring spins via a three-site exchange mechanism with the underlying atom of the HM (white atoms). As a consequence, the absolute frequency of $+k$ spin waves is down-shifted in frequency. (b) SWs propagating along the negative x direction, i.e., with a $-k$ wave vector, are characterized by an counterclockwise chirality, that is disfavored by a positive D, resulting in an up-shift of their absolute frequency.

and *in situ* operation since they are sensitive to the first atomic layers, so they cannot be employed for samples grown elsewhere and the sample has to be perfectly clean. The use of DFT or Monte Carlo simulations may help in refining the extraction of DMI but requires substantial computational effort. However, the main advantage of these methods is the direct determination of the structure and chirality of the DW.

III. SPIN-WAVE METHODS

A. Method overview

Since their formation and propagation depend on the magnetic energies present in a material or a thin film, spin waves (SWs) are used as a sensitive tool to extract magnetic properties such as susceptibility, anisotropy, Gilbert damping, and exchange stiffness. These properties, together with the geometry of the sample and the excitation, determine the spin-wave frequency, linewidth, relative amplitude, and attenuation length. The DMI modifies not only the equilibrium magnetic ground state (Bak and Jensen, 1980) but also the spin-wave dynamics (Melcher, 1973; Kataoka, 1987; Zheludev *et al.*, 1999). SWs propagating in opposite directions have opposite chiralities, so the DMI contribution to the SW energy may either decrease or increase the SW frequency and results in an intrinsic nonreciprocity of the SW propagation.[11] This is illustrated in Fig. 17. Note that, unlike the case of the domain walls analyzed in Sec. II, where the static magnetization is usually normal to the film plane, here the static component of the magnetization is forced to be in-plane by the external magnetic field. Therefore, in the BLS community it is popular to assume a different reference frame, as we do in this section, where both the applied field H and the static magnetization lie along the z direction, as shown in Fig. 17 while the dynamic component of the magnetization (the small blue arrows in Fig. 17) exhibit a chirality that can be either the same as or the opposite of the DMI-favored chirality, depending on the propagation direction of the SWs. For magnetic films this DMI-induced nonreciprocity was theoretically investigated for the first time by Udvardi and Szunyogh (2009), and a series of other theoretical investigations followed (Costa *et al.*, 2010; Cortés-Ortuño and Landeros, 2013; Moon *et al.*, 2013; Kostylev, 2014). Experimentally, the relatively strong asymmetry in the spin-wave dispersion is of interest since the frequency of spin-wave spectra can be measured with high

---

[11] This does not occur for arbitrary directions of DMI vector and spin-wave propagation, as further explained, and special experimental geometries have to be realized.

accuracy. A pioneering investigation of DMI-induced nonreciprocity in spin-wave propagation was performed by analyzing SWs with large wave number (Zakeri *et al.*, 2010) by spin-polarized electron loss spectroscopy (SPEELS). Although a high wave number k is advantageous,[12] leading to large DMI-induced frequency changes, the most versatile and exploited technique to determine DMI-related effects on SW propagation is BLS, which relies on the inelastic scattering of photons by spin waves with micrometric or submicrometric wavelengths. BLS is becoming increasingly popular thanks to the good compromise between sensitivity to SWs in a wide range of k vectors and relatively simple experimental apparatuses. Two techniques that have also been applied to the study of SW propagation are the time resolved magneto-optical Kerr effect (TRMOKE) and propagating spin-wave spectroscopy (PSWS). In the following we first recall some theoretical background on the influence of DMI on SW characteristics and review the main results achieved by the four aforementioned experimental techniques while comparing their advantages and limitations.

B. Theory and models

In the literature we find basically two theoretical approaches to describe spin-wave spectra in thin film samples with a DMI. One is based on the classical theory of magnetostatic spin waves [see Gallardo, Cortés-Ortuño, Troncoso, and Landeros (2019)], and this is the approach mainly utilized for analyzing experimental results obtained by BLS, PSWS, or TRMOKE. The other is based on the quantum spin-wave theory, which is more suitable for high k measurements in ultrathin films, such as those done in SPEELS, where the exchange interaction dominates the spin-wave dispersion (Udvardi and Szunyogh, 2009; dos Santos *et al.*, 2018; dos Santos, Dias, and Lounis, 2020). In most experimental cases, the two formalisms are equivalent and slight differences derive only from the choice of energy terms. Some researchers even use a mixed approach that calculates the spin-wave spectra using a quantization of the linearized Landau-Lifshitz equation (Udvardi *et al.*, 2003). The models used to analyze the experimental results (Moon *et al.*, 2013) typically derive the dispersion relation and do not consider the specific sensing technique, so they are applicable to all four techniques presented in Sec. III.C.

1. Quantum spin-wave theory

The usual quantum formalism for spin waves uses the Holstein-Primakoff method (Holstein and Primakoff, 1940) and starts directly from the Schrödinger equation with a Hamiltonian in a crystal lattice of spins $\vec{S}_j$ that considers the Heisenberg exchange energy at a spin site j with the nearest neighbors at position $j+\delta$ and the Zeeman energy in a magnetic field $B_0\hat{z}$,

$$\mathcal{H} = -2\frac{J}{\hbar^2}\sum_{j,\delta}\vec{S}_j\cdot\vec{S}_{j+\delta} - \frac{g\mu_B B_0}{\hbar}\sum_j S_{j_z}, \tag{3.1}$$

where J is the exchange constant, g is the Landé factor, and μ_B is the Bohr magneton. As Stamps and Hillebrands (1991) described, using the spin raising and lowering operators one can analytically obtain the eigenstates and energies in certain simplified cases (such as low temperature approximations) by employing the Holstein-Primakoff transformation and using the Fourier transform of the harmonic oscillator raising and lowering operators as creation and annihilation operators for the quantized spin waves (magnons). For $ka \ll 1$ in a cubic lattice of spins s with lattice constant a, and considering only nearest-neighbor interactions, one obtains the known quadratic dispersion relation

$$\hbar\omega_k = g\mu_B B_0 + 4Jsa^2k^2. \tag{3.2}$$

As mentioned in the Introduction, in a microscopic approach the DMI is considered a generalized exchange interaction leading to a noncollinear spin configuration described by $\vec{D}\cdot(\vec{S_1}\times\vec{S_2})$, where the direction of $\vec{D}$ depends on the crystal symmetry. This leads to an additional term in the Hamiltonian (Zheludev *et al.*, 1999; Moon *et al.*, 2013),

$$\mathcal{H}_{\mathrm{DMI}} = 2\frac{D}{\hbar^2}\sum_j \hat{z}\cdot(\vec{S}_j\times\vec{S}_{j+1}), \tag{3.3}$$

where $\hat{z}$ is perpendicular to the axis of symmetry breaking. The related term that has to be added in the spin-wave dispersion [Eq. (3.2)] is linear in k:

$$\hbar\omega_{\mathrm{DMI}} = 4Dsak. \tag{3.4}$$

The first study of a DMI in bulk $Ba_2CuGe_2O_7$, an antiferromagnet with a weak helimagnetic distortion (Zheludev *et al.*, 1999), was performed in 1999 using the quantum approach and showed low-energy spin-wave spectra. This approach does not consider the sample geometry but instead only crystal symmetry, so it is suitable for bulk materials. In the case of ultrathin films, it was shown theoretically about ten years later that the chiral degeneracy of the magnons can be lifted due to the presence of the DMI (Udvardi and Szunyogh, 2009). The employed method, based on relativistic first principles calculations of the magnetic ground state similar to those given by Bode *et al.* (2007) and Ferriani *et al.* (2008), was able to identify domain-wall chirality. Therefore, it was proposed to exploit this spin-wave asymmetry for measuring DMIs in ultrathin films. Although it had been known for a decade that the DMI stabilizes chiral spin structures in bulk materials with a certain crystal symmetry (Crépieux and Lacroix, 1998; Bogdanov and Rößler, 2001), the work of Udvardi and Szunyogh (2009) was stimulated by the discovery of homochirality of domain walls in two monolayers of Fe on W(110) (Kubetzka *et al.*, 2003; Heide, Bihlmayer, and Blügel, 2008).

A quantum approach was also used by Costa *et al.* (2010), who, going back to the microscopic origin of the DMI, studied the effects of SOC on spin-wave spectra. It was shown that the DMI leads to a linear term in k in the dispersion relation and that the linewidth of spin-wave modes is increased by the spin-orbit coupling. The method used there, which goes beyond the

---

[12] As we later show, the DMI-induced frequency shift is linear with the wave vector k of the involved spin waves.

adiabatic approximation and operates directly in the wave vector space, avoided calculations in real space and took into account large numbers of neighbor shells. The starting point is the multiband Hubbard model with a Hamiltonian (Costa, Muniz, and Mills, 2003), where a spin-orbit interaction is added. The spin-wave dispersion is then obtained from the dynamic susceptibility. In essence, the quantum approach shows the microscopic origin based on SOC and derives an additional k-linear term in the spin-wave dispersion relation for certain relative orientations of spin-wave propagation and the direction of the DMI vector.

2. Classical spin-wave theory

Since in most experimental investigations (as in BLS) the wavelength of the detected SWs ranges from a few microns to a few hundred nanometers, one can ignore the discrete nature of the spins. Therefore, a classical formulation, assuming a continuum medium, is more suitable. Traditionally, spin waves in magnetic thin films are treated as magnetostatic spin waves, with the exchange interaction neglected (Prabhakar and Stancil, 2009). Considering different geometries and their related boundary conditions, one obtains either forward volume for perpendicular-to-plane magnetization or backward volume and surface or Damon-Eshbach (DE) waves for in-plane magnetization. The latter, where the wave vector $\vec{k}$ is perpendicular to the applied static field $\vec{H}$, is the preferred configuration when spin waves are excited via antennas due to their more efficient transduction. However, as pointed out in the literature, for typical samples with DMIs the simple magnetostatic solution is not sufficient, and anisotropy energy or exchange energy often has to be considered (Kalinikos, 1981; Kalinikos and Slavin, 1986; Gurevich, 1996). Here the complete problem is solved in the thin film limit for the magnetization $\vec{M}$, including the magnetostatic and dynamic regime using mixed boundary conditions and going beyond the plane-wave approximation. The exchange term is often neglected when theory is compared to experiments, with the argument that that the wave number k obtained in the experimental conditions is low. However, to be precise, the spin-wave modes obtained in nanostructured films require the complete solution, as they are in the transition range from magnetostatic to exchange spin waves (dipole-exchange spin waves). One of the critical energy terms is the dipolar field term, which can be obtained from this approach by adding the exchange boundary conditions to the electrodynamics boundary conditions. As Moon *et al.* (2013) noted, the dipolar field term contains local and nonlocal contributions and can be divided into a stray field term related to the dipolar interactions between the spins in the SW and a dipole or magnetostatic field term related to the demagnetizing field. In most cases, such as that given by Moon *et al.* (2013), the dipolar term for unpinned exchange at the film surface [i.e., $(\partial/\partial y)\vec{m} = 0$ at the FM film surface] is applied (Kalinikos, 1994). However, Kostylev (2014) pointed out that the DMI pins the circular components of the magnetization at the surface (interface) of the magnetic film and mixed boundary conditions have to be used, which requires a numerical solution.

Considering a sample geometry such as that shown in Fig. 17 (static component of the magnetization aligned along the z direction, i.e., parallel to the applied field H), the dispersion relation for small amplitude spin waves is derived from the linearized Landau-Lifshitz (LL) equation,

$$\frac{\partial \vec{M}}{\partial t} = -\gamma \mu_o (\vec{M} \times \vec{H}_{\mathrm{eff}}). \tag{3.5}$$

The vector $\vec{M}$ has to be decomposed in one large static component of modulus M_s directed along the z axis and two small dynamic components that describe the precession around the equilibrium direction: $\vec{M} = M_s \hat{m}(\vec{x}, t) = M_s(m_x, m_y, 1)$, with $|m_x|, |m_y| \ll 1$ and the y axis perpendicular to the sample plane according to Fig. 17. The effective field to be considered in the LL equation consists of different contributions, reflecting the different energy terms

$$\vec{H}_{\mathrm{eff}} = -\frac{1}{\mu_0}\frac{\delta E_{\mathrm{tot}}}{\delta \vec{M}} = H\hat{z} + J\nabla^2 \vec{m} + \vec{H}_{\mathrm{dip}} + \vec{H}_{\mathrm{ani}} + \vec{H}_{\mathrm{DMI}}, \tag{3.6}$$

where $J = 2A/\mu_0 M_s$ is the exchange constant. In the case of unpinned exchange boundary conditions, the dipolar field for a thin film can be written as (Kalinikos, 1994; Arias and Mills, 1999)

$$\vec{H}_{\mathrm{dip}} = -M_s m_x P(kd)\hat{x} - M_s m_y [1 - P(kd)]\hat{y}, \tag{3.7}$$

$$\text{with} \quad P(kd) = 1 - \frac{1 - e^{-|kd|}}{|kd|}, \tag{3.8}$$

which, in the case of ultrathin films with thickness d, where $kd \ll 1$, reduces to $P(kd) = |kd|/2$ when a series expansion of the exponential function is performed. The anisotropy field written for the case of a uniaxial perpendicular anisotropy constant K_u out of plane is $\vec{H}_{\mathrm{ani}} = (2K_u/\mu_0 M_s) m_y \hat{y}$.

The correct expression for the DMI field H_{DMI} in the continuum theory is not straightforward to obtain, as it depends on the considered crystal symmetry. For bulk materials, the first approach from a spin to a continuum model was performed by Dzyaloshinskii himself (Dzyaloshinskii, 1958), who calculated a thermodynamic potential for certain crystal symmetry classes. This approach was later used by Bak and Jensen (1980) for MnSi and FeGe, and by Bogdanov and Hubert (1994) and Bogdanov and Rößler (2001), who used the Lifshitz invariants $\vec{\mathcal{L}}(\vec{M}, \nabla \times \vec{M})$, where the kth component of $\vec{\mathcal{L}}$ is $\mathcal{L}_{ij}^{(k)} = M_i \partial M_j/\partial x_k - M_j \partial M_i/\partial x_k$. The DMI energy can be described as a combination of Lifshitz invariants, depending on the crystal symmetry (Crépieux and Lacroix, 1998; Cortés-Ortuño and Landeros, 2013). For certain symmetry classes, such as the rotational tetrahedral[13] **T** (for instance, MnSi), the energy density due to DMI is a combination of Lifshitz invariants with a single coefficient D. Only in these cases is the DMI strength sufficiently described by a scalar. Another

---

[13] Schoenflies notation.

example is the cyclic class $\mathbf{C}_{nv}$. Its Lifshitz invariants are a suitable choice for planar systems (bilayers) with perpendicular anisotropy, where symmetry breaking occurs only along the perpendicular axis and only gradients in plane contribute to the DMI-induced chirality (Bogdanov and Yablonskii, 1989; Bogdanov and Rößler, 2001). For a planar geometry in the x-z plane with perpendicular anisotropy along y, the DMI energy can be described using

$$E_{\mathrm{DMI}} = D(\mathcal{L}_{xy}^{(x)} + \mathcal{L}_{zy}^{(z)}). \tag{3.9}$$

With $\vec{M} = M_s \hat{m}(\vec{x}, t) = M_s(m_x, m_y, 1)$ the DMI field can then be obtained as

$$\vec{H}_{\mathrm{DMI}} = -\frac{1}{\mu_0}\frac{\delta E_{\mathrm{DMI}}}{\delta \vec{M}} = \frac{2D}{\mu_0 M_s}\left(\frac{\partial m_y}{\partial x}, -\frac{\partial m_x}{\partial x}, 0\right). \tag{3.10}$$

The dispersion relation is then given by

$$\begin{aligned}\omega(k) &= \gamma\mu_0\sqrt{[H_0 + Jk^2 + M_s P(kd)\sin^2\varphi_k]\{H_0 + Jk^2 - H_{\mathrm{ani}} + M_s[1 - P(kd)]\}} + \omega_{\mathrm{DMI}} \\ &= \omega_0 + \omega_{\mathrm{DMI}},\end{aligned} \tag{3.11}$$

which is also valid for values of φ_k other than $\pi/2$, as shown in Fig. 18. Moreover, it can be shown that the general expression of ω_{DMI} for an interfacial DMI is given by (Gallardo, Cortés-Ortuño, Troncoso, and Landeros, 2019)

$$\omega_{\mathrm{DMI}} = \frac{2\gamma D}{M_s} k \sin\varphi_k \cos\varphi_M, \tag{3.12}$$

where the angles are as defined in Fig. 18. This means that, like the previously mentioned results for the quantum approach, the DMI leads to a shift of the dispersion relation, linear in k and depending on the sign of the wave vector, i.e., a frequency nonreciprocity due to DMI; see Fig. 19. This nonreciprocity depends on the directions of both the sample magnetization and the spin-wave propagation and is absent for $k = 0$, i.e., the condition for ferromagnetic resonance (FMR). In this respect, Cortés-Ortuño and Landeros (2013) had already suggested using BLS measurements for determining the DMI constant and pointed out that the largest effect can be observed by applying a sufficiently large external field H, such that the magnetization lies in plane ($\varphi_M = 0$), using the DE geometry ($\varphi_k = \pi/2$).

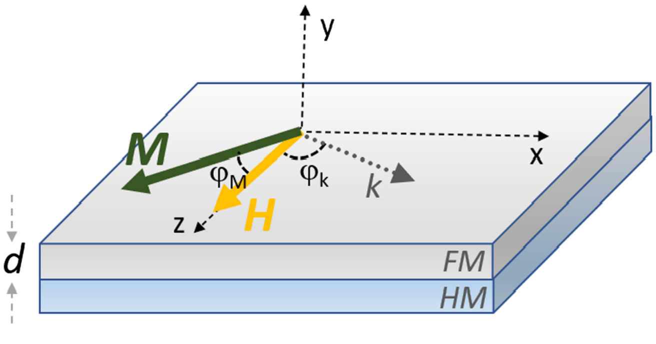

FIG. 18. Schematic diagram of the used geometry and notation. k is the wave vector and indicates the propagation direction of the spin wave, H is the applied in-plane field, and M is the equilibrium magnetization, pointing slightly out of plane. The DMI frequency depends on the angles φ_k and φ_M, as given in Eq. (3.12).

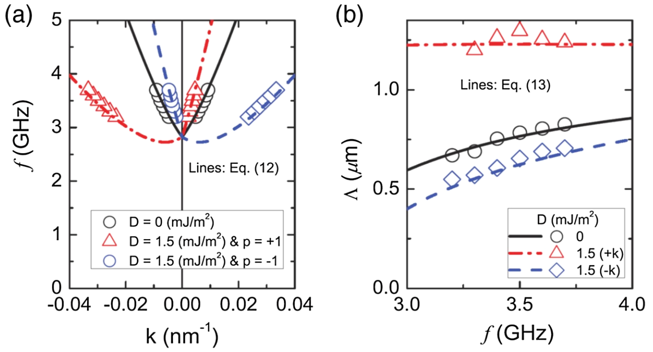

FIG. 19. DMI-induced asymmetric spin-wave propagation in the small-k limit. (a) Dispersion relation. (b) Attenuation length as a function of the frequency f. From Moon *et al.*, 2013.

Note that the previous dispersion relation is valid up to a certain threshold of the DMI strength, above which the dispersion relation reaches zero, reflecting the instability of the ground state, which is no longer uniform but rather chiral, and the theory may not be applicable. With numerical calculations it was shown that the asymmetry regards not only frequency but also amplitude and attenuation length (Kostylev, 2014; Körner *et al.*, 2015).

Also notice that the previous description is valid only for a film consisting of a single monolayer. An attempt to take the finite film thickness correctly into account using mixed exchange boundary conditions at the surface was shown by Kostylev (2014).[14] The resulting boundary conditions then are similar but not equal to the ones derived for a uniaxial surface anisotropy (Soohoo, 1963). Different surface anisotropies at the two interfaces of the magnetic film result in an intrinsic nonreciprocity of DE spin waves (Hillebrands, Baumgart, and Güntherodt, 1987). In this case the two contributions are difficult to distinguish. In fact, Crépieux and Lacroix (1998) interpreted the presence of a DMI as a contribution to the surface anisotropy. To analyze the different contributions in a more rigorous way, film thickness dependencies have to be studied, as Gladii *et al.* (2016) and Lucassen *et al.* (2020) discussed.

---

[14] Note that the DMI constant given by Kostylev (2014) is defined as the DMI constant in the first atomic layer and is therefore given by $\tilde{D} = Dd\sqrt{2}/a$, where a is the lattice constant.

TABLE XIV. Overview of DMI measurements for Co thin films via BLS (publication years 2015–2018). FM and NM stand for ferromagnetic and nonmagnetic layers, respectively. D is the interfacial DMI constant and $D_s = Dd$, with d the thickness of the ferromagnetic film. Numbers in roman were quoted in the reviewed papers, while numbers in italics were either extracted from figures or calculated using the parameters provided. Signs with asterisks are rendered according to the convention used in this review and are the opposite of that in the original manuscript.

FM (nm)	Bottom NM (nm)	Top NM (nm)	D (mJ/m^2)	D_s (pJ/m)	Sign	Reference
Co(0.6 – 1.2)	Ta(3)/Pt(3)	AlO_x/(2)Pt(3)	2.7–1.6	1.6–1.9	–	Belmeguenai *et al.* (2015)
Co(1 – 2)	Pt(4)	AlO_x(2)	*1.2–0.9*	*1.2–1.8*		Cho *et al.* (2015)
Co(1)	Pt(5)	GdO_x(2 – 5)/Al(2)	*1.6*	1.6	–	Vaňatka *et al.* (2015)
Co(1 – 1.7)	Pt(4)	AlO_x(2)	*1.2–0.8*	*1.2–1.4*	–*	Kim, Han *et al.* (2015)
Co(1.3 – 1.8)	Ta(4)/Pt(4)		*1.6–1.3*	*2.1–2.3*	–*	
Co(1.06)	Ta(3)/Pt(3)	MgO(2)/Ta(2)	2.05	2.17	–	Boulle *et al.* (2016)
Co(1.3 – 2.9)	Ta(4)/Ir(4)	AlO_x(2)	*0.7–0.35*	*0.9–1*		Kim *et al.* (2016)
Co(2)	Ta(4)	Pt(4)	0.7	*1.4*	+	Cho *et al.* (2017)
	Pt(4)	Ta(4)	0.92	*1.84*	–	
Co(1.6)	Ta(4)/Pt(0.8)	AlO_x(2)/Pt(1)	0.43	*0.7*	–	Kim, Han *et al.* (2017)
	Ta(4)/Pt(4.8)		1.57	*2.51*	–	
Co(2.5)	Pt(5.4)	Au(2.5)/Pt(2.6)	0.60	1.51	–	Rowan-Robinson *et al.* (2017)
		Ir(2.5)/Pt(2.6)	0.60	1.51	–	
Co(1)	Ta(5)	MgO(2)/Ta(2)	*0.08*	0.08	+	Ma *et al.* (2018)
	W(5)		*0.11*	0.11	+	
	Ir(5)		*0.34*	0.34	–	
	Pt(5)		*1.59*	1.59	–	
	Au(5)		*0.22*	0.22	–	
Co(3)	MgO(2)/Pt(6)	Ru(3)	0.43[a]	1.3[a]	–	Bouloussa *et al.* (2018)
			0.33[b]	1[b]	–	
Co(1)	Ta(5)/Pt(2)	$\mathrm{Ir}_{20}\mathrm{Mn}_{80}$(1.1)	1.14	1.14	–	Khan *et al.* (2018)
		$\mathrm{Ir}_{20}\mathrm{Mn}_{80}$(1.7)	1.14	1.14	–	
		$\mathrm{Ir}_{20}\mathrm{Mn}_{80}$(2.4)	1.22	1.22	–	
		$\mathrm{Ir}_{20}\mathrm{Mn}_{80}$(5)	1.11	1.11	–	
Co(0.6)	Ta(5)/Pt(2)	$\mathrm{Fe}_{50}\mathrm{Mn}_{50}$(1)	1.5	1.35[c]	–	Khan *et al.* (2018)
		$\mathrm{Fe}_{50}\mathrm{Mn}_{50}$(2.6)	1.44	1.3[c]	–	
$[\mathrm{Co}(0.2)/\mathrm{Ni}(0.6)]_2/\mathrm{Co}(0.2)$	Pt(1.2)	Ta(0.8)/TaN(6)	*0.49*	*0.88*	–	Lau *et al.* (2018)
	Ir(1.2)		*0.05*	*0.09*	–	
	$\mathrm{Pt}_{0.4}\mathrm{Ir}_{0.6}$(1.2)		*0.19*	*0.34*	–	
	$\mathrm{Pt}_{0.6}\mathrm{Ir}_{0.4}$(1.2)		*0.24*	*0.43*	–	

[a] The sample is a stripe sample with a stripe width of 300 nm and a spacing of 100 nm.

[b] Stripe width, 100 nm; spacing 100 nm.

[c] For the D_s calculation, a monolayer of Fe from the Co/FeMn interface was added to the effective thickness of the FM layer.

In summary, we point out that the complete solution in the continuum theory for the bilayer system is not trivial and requires assumptions concerning the boundary conditions. Care especially has to be taken if one wants to take all contributions to the spin-wave dispersion nonreciprocity (such as surface anisotropies) into account correctly. However, in most cases the theory required for modeling experimental results is simplified by the fact that the DMI-related term in the spin-wave dispersion relation is directly determined by subtraction (as later explained).

C. Experimental results

1. Brillouin light scattering

The most popular and widely employed technique for the measurement of the DMI constant from the nonreciprocal spin-wave propagation is BLS (Carlotti and Gubbiotti, 1999). As shown in Tables XIV–XVII, more than 40 papers reporting the value of the DMI constant in samples where a FM material (usually Co or CoFeB) is in contact with a HM material (Pt, W, Ta, etc.) have been published since 2015. One of the first BLS experimental works reporting values of the DMI constant determined by BLS was done on Co/Ni multilayers (Di *et al.*, 2015a, 2015b; Zhang *et al.*, 2015). In the same year a series of publications of DMI measurements by BLS on Py, Co, and CoFeB followed (Belmeguenai *et al.*, 2015; Cho *et al.*, 2015; Kim, Kim *et al.*, 2015; Nembach *et al.*, 2015; Stashkevich *et al.*, 2015; Vaňatka *et al.*, 2015), and the research continues to be active.

BLS is a classical tool for studying spin-wave dispersion in general, and nonreciprocity in particular. As sketched in Fig. 20 in a BLS experiment, a monochromatic light beam is focused on the surface of the specimen under investigation by an objective lens. The light that is backscattered within a solid

TABLE XV. Overview of DMI measurements for Co thin films via BLS (publication years 2019–2021). FM and NM stand for ferromagnetic and nonmagnetic layers, respectively. D is the interfacial DMI constant and $D_s = Dd$, with d the thickness of the ferromagnetic film. Numbers in roman were quoted in the reviewed papers, while numbers in italics were either extracted from figures or calculated using the parameters provided. Signs with asterisks are rendered according to the convention used in this review and are the opposite of that in the original manuscript.

FM (nm)	Bottom NM (nm)	Top NM (nm)	D (mJ/m^2)	D_s (pJ/m)	Sign	Reference
Co(1 − 2)	Ta(3)/Pt(3)	Ir(3)	0.8–0.3	0.8	−	Belmeguenai *et al.* (2019)
		Cu(3)	0.9–0.4	1.05	−	
		MgO(1)	0.9–0.4	0.95	−	
		Pt(3)	0	0		
[Pt(1.5)/Co(1–2)/W(1.5)]$_1$			0.2–0.3	0.55	−	Benguettat-El Mokhtari *et al.* (2019)
[Pt(1.5)/Co(1–2)/W(1.5)]$_3$			1.1–0.6	0.85	−	
[Pt(1.5)/Co(1–2)/W(1.5)]$_7$			1.2–0.6	0.90	−	
Co(0.6)	Pt(3)	HfO$_2$(3)	0.9	*0.54*	−	Diez *et al.* (2019a)
Co(0.9)	Ta(5)/Pt(1.5)	Ti(2.5)/Pt(2.5)	1.42	*1.28*		D.-Y. Kim *et al.* (2019)
		Cu(2.5)/Pt(2.5)	0.87	*0.78*		
		W(2.5)/Pt(2.5)	1.25	*1.13*		
		Ta(2.5)/Pt(2.5)	0.99	*0.89*		
		Al(2.5)/Pt(2.5)	0.92	*0.83*		
		Pt(2.5)/Pt(2.5)	0.02	*0.02*		
Co(1.4)	Ta(5)/Pt(5)	MgO(2)/Ta(3)	1.20	*1.68*		W.-Y. Kim *et al.* (2019)
		Cu(2)/Ta(3)	1.05	*1.47*		
Co(0.8)	Ta(2)/Pt(2.2)	Ir(0 − 2)/Ta(4)	*1.8–0.88*	*1.64–0.7*	−*	Shahbazi *et al.* (2019)
[Pt(3)/Co(1.1)/Ta(4)]$_{12}$			0.78	*0.86*	−	Saha *et al.* (2019)
Co(1.2)	Ta(2.5)/Pt(0.4 − 2.2)[a]	Pt(2)	0.27–0.42	*0.32–0.5*	+	Gusev *et al.* (2020)
Co(0.8 − 2.5)	Ta(3)/Pt(3)	Ir(3)	*0.95–0.3*	0.76	−	Benguettat-El Mokhtari *et al.* (2020)
Co(0.9 − 2.5)	Ta(3)/Pt(3)[b]	Ir(3)	0.6–0.2	0.53	−	
Co(1.1 − 3.1)	Ta(3)/Ir(3)[b]	Pt(3)	0.88–0.32	1.05	+	
Co(1 − 2.6)	Ta(3)/Ir(3)[c]	Pt(3)	0.8–0.3	0.77	+	
Co(0.8 − 2.5)	Ta(3)/Pt(3)[b]	Cu(3)	*1.31–0.42*	1.05	−	
Co(1 − 2.2)	Ta(3)/Pt(3)[b]	MgO(1)	1–0.5	0.95	−	
Co(1.5 − 2.1)	Ta(3)/Pt(3)[c]	MgO(1)	0.8–0.6	1.17	−	
Co(1.2 − 10)	Pt(3)	TaO$_x$(0.8)/Al(0.5)	1–0.15	1.25[d]	−	Benguettat-El Mokhtari, Roussigné *et al.* (2020)
Co(1.2)	Pt(3)	TaO$_x$(0.7–0.9)/Al(0.5)	1.2–1.5	*1.44–1.8*	−	
Co(1.2)	Pt(3)/Cu(0 − 2.4)	TaO$_x$(0.8)/Al(0.5)	1.3–0	*1.56–0*	−	
Co(0.7)	Pt(5)	Ni$_x$O$_y$(15)	1.75[e]	1.3	−	Kolesnikov *et al.* (2021)
[W(1)/Co(0.6)/Pt(1)]$_{10}$			2.65	1.83	+	Jena *et al.* (2021)
[W(1)/Co(0.6)/Pt(1)]$_{20}$			2.49	1.72	+	

[a] On a glass substrate.
[b] Annealed at 300 °C.
[c] As grown.
[d] This value was extracted from a fit of the experimental data of all samples with various Co thicknesses.
[e] Sample deposited with Ar pressure of 0.13 Pa.

angle is collected by the same lens and analyzed in frequency by a high-resolution spectrometer, usually a Sandercock-type, multipass tandem Fabry-Perot interferometer (Mock, Hillebrands, and Sandercock, 1987). The physical mechanism of BLS relies on the inelastic scattering of photons by spin waves that are naturally present within the medium under investigation, thanks to either the creation (Stokes process) or the annihilation (anti-Stokes process) of a magnon. This implies that a redshift or a blueshift is observed in the scattered light with respect to the incident beam. In wave vector space, magnons experiencing Stokes or anti-Stokes scattering processes correspond to either a positive or a negative wave vector. As a consequence, the nonreciprocity caused by the presence of a DMI interaction leads to an asymmetry in the frequency shift of the peaks corresponding to the Stokes or the anti-Stokes process, as anticipated; see Fig. 20. A wide range of k vectors is available, up to about 2.2×10^5 rad/cm. The specific value of k can be easily varied by changing the angle of the incident beam of light, while reversing the applied magnetic field permits one to cross-check for the sign of the DMI constant. The frequency resolution is limited by the instrumental characteristics to about 0.1 GHz because the finesse of the Fabry-Perot interferometer (the ratio between the free spectral range and the passband window) has an upper limit of about 100 (Carlotti and Gubbiotti, 1999). This implies a lower limit for the minimum values of the DMI constant that can be measured

TABLE XVI. Overview of DMI measurements for CoFeB thin films via BLS. FM and NM stand for ferromagnetic and nonmagnetic layers, respectively. D is the interfacial DMI constant and $D_s = Dd$, with d the thickness of the ferromagnetic film. Numbers in roman were quoted in the reviewed papers, while numbers in italics were either extracted from figures or calculated using the parameters provided. Numbers with asterisks indicate that a magnetic dead layer was taken into account. Signs with asterisks are rendered according to the convention used in this review and are the opposite of that given in the original manuscript.

FM (nm)	Bottom NM (nm)	Top NM (nm)	D (mJ/m^2)	D_s (pJ/m)	Sign	Reference
$Co_{48}Fe_{32}B_{20}$(1.6–3)	Pt(4)	AlO_x(2)	*0.8–0.4*	*1.2–1.3*		Cho *et al.* (2015)
$Co_{40}Fe_{40}B_{20}$(0.8)	MgO(2)/Pt(2)	MgO(2)/SiO_2(3)	1	*0.8*	−	Di *et al.* (2015a)
$Co_{20}Fe_{60}B_{20}$(0.85, 1, 1.5, 2, 3)	W(2)	SiO_2(2)	*0.25–0.08*	*0.21–0.24*		Chaurasiya *et al.* (2016)
$Co_{20}Fe_{60}B_{20}$(1)	W(2)	MgO(1)/Ta(1)	0.25	*0.25*	+*	Soucaille *et al.* (2016)
	W(3)		0.27	*0.27*	+*	
	$Ta_{48}N_{52}$(1)		0.31	*0.31*	+*	
	Hf(1)		0.15	*0.15*	+*	
$Co_{20}Fe_{60}B_{20}$(1)	Ta(5)	Pt($0.12-0.27$)/MgO(2)	*0.07–0.015*	*0.07–0.015*	+	Ma *et al.* (2016)
$Co_{20}Fe_{60}B_{20}$(2)	$Ir_{22}Mn_{78}$($1-7.5$)	MgO(2)/Ta(2)	0.02–0.13	*0.04–0.26*	−	Ma *et al.* (2017)
$Co_{20}Fe_{60}B_{20}$($0.8-2$)	$Ir_{22}Mn_{78}$(5)		*0.15–0.07*	*0.12–0.14*	−	
$Co_{20}Fe_{60}B_{20}$(1.2)	Ir(5)		*0.17*	*0.2*	+	
$Co_{40}Fe_{40}B_{20}$(2)	Si/SiO_2	Pt(2)/Cu(3)	0.45[a]	*0.9*	+	Tacchi *et al.* (2017)
$Co_{40}Fe_{40}B_{20}$(2)	Pt(4)	Ta(4)	0.51	*1.02*	−	Cho *et al.* (2017)
	Ta(4)	Pt(4)	0.43	*0.86*	+	
	Ta(4)	Ta(4)	0.15	*0.3*	−	
	Pt(4)	Pt(4)	0.01	*0.02*	−	
$Co_{20}Fe_{60}B_{20}$(1.12)	Ta(3)/Pt(3)	Ru(0.8)/Ta(3)	0.84	*0.94*	−	Belmeguenai *et al.* (2017)
	Pt(3)/Ru(0.8)	MgO(1)/Ta(3)	0.3	*0.37*	−	
$Co_{20}Fe_{60}B_{20}$(1)	Ta(5)	MgO(2)/Ta(2)	*0.04*	0.04	+	Ma *et al.* (2018)
	W(5)		*0.07*	0.07	+	
	Ir(5)		*0.21*	0.21	+	
	Pt(5)		*0.97*	0.97	−	
	Au(5)		*0.17*	0.17	−	
$[Pt(5)/Co_{20}Fe_{60}B_{20}(1)/Ti(1)]_1$	Ti(5)	Pt(5)	0.81	*0.81*		Karakas *et al.* (2018)
$[Pt(5)/Co_{20}Fe_{60}B_{20}(1)/Ti(1)]_{10}$			0.79	*0.79*		
$[Pt(5)/Co_{20}Fe_{60}B_{20}(1)/Ti(1)]_{15}$			0.67	*0.67*		
$[Pt(5)/Co_{20}Fe_{60}B_{20}(1)/Ti(1)]_{60}$			0.71	*0.71*		
CoFeB(1)	Ta(5)/Pt($0.7-4$)	MgO(1)/Ta(1)	*0–0.87*	*0–0.87*	−	Chen, Zhang *et al.* (2018)
$Co_{40}Fe_{40}B_{20}$(0.9)	W($1-13$)	MgO(1)/Ta(2)	*0.25–0.7*	*0.23–0.63*		G. W. Kim *et al.* (2018)
$Co_{20}Fe_{60}B_{20}$(0.9)	Ta(3)	TaO_x(1)	*0.08*	*0.05**	+	Srivastava *et al.* (2018)
$Co_{20}Fe_{60}B_{20}$(1.5)	Ta(1)	Cu($0-2.4$)/Pt(4)	0.52–0.14	*0.78–0.21*	+	Benguettat-El Mokhtari, Ourdani *et al.* (2020)
		Ta($0-2.4$)/Pt(4)	0.52–0	*0.78–0*	+	
		MgO($0-1.8$)/Pt(4)	0.55–0	*0.78–0*	+	
$Co_{20}Fe_{60}B_{20}$($1.5-6$)		Pt(4)	0.7–0.2	1.25[b]	+	
$Co_{20}Fe_{60}B_{20}$(2)	TiO_2-BTO	Pt(4)	0.45	*0.9*	+	Lin *et al.* (2020)
	$BaO-BTO$	Pt(4)	0.56	*1.12*	+	

[a] For $d_{Pt} > 2$ nm.

[b] D_s is obtained from the linear fit of D vs $1/d$ for $d > 1.5$ nm (d is the FM thickness).

with this technique. One should also consider that several tens of milliwatts of light are usually focused on the measurement spot, so the real temperature[15] of the probed sample region may be lifted above room temperature, which can have an influence on the values of the measured magnetic parameters, including D. Here we adopt the reference frame presented in Figs. 17 and 20, where the z axis is aligned with the static magnetization, the x axis coincides with the propagation direction of the SWs, and the film normal (y axis) is oriented upward with respect to the free surface of the FM film. With this choice, the frequency shift of the BLS peaks is

$$f_{\mathrm{DMI}} = \omega_{\mathrm{DMI}}/2\pi = \gamma D k/\pi M_s. \tag{3.13}$$

For the case of a FM/HM bilayer, as sketched in Fig. 20, a negative (positive) value of f_{DMI}, i.e., of D, indicates that a

---

[15] Note that the real temperature depends on the thermal properties of the material under investigation (including the substrate material), as well as the numerical aperture of the exploited lens (which determines the size of the focused light spot).

TABLE XVII. Overview of DMI measurements for various FM materials via BLS. FM and NM stand for ferromagnetic and nonmagnetic layers, respectively. YIG, GGG, and Py stand for yttrium iron garnet, gadolinium gallium garnet, and NiFe, respectively.D is the interfacial DMI constant and $D_s = Dd$, with d the thickness of the ferromagnetic film. Numbers in roman were quoted in the reviewed papers, while numbers in italics were either extracted from figures or calculated using the parameters provided. The value indicated with $*$ was given for the thickest FM film.

FM (nm)	Bottom NM (nm)	Top NM (nm)	D (mJ/m^2)	D_s (pJ/m)	Sign	Reference
Co(1.6)/Ni(1.6)	Pt(4)	MgO(2)/SiO_2(3)	0.44	*1.4*	−	Di *et al.* (2015b)
$Ni_{80}Fe_{20}$(4)	Si substrate	Pt(6)	*0.056*[a]	*0.34*	+	Stashkevich *et al.* (2015)
Co(1.6)/Ni(1.6)	MgO(2)/Pt(4)	MgO(2)/SiO_2(3)	0.44	*1.4*	−	Zhang *et al.* (2015)
$Ni_{80}Fe_{20}$(1 − 13)	Ta(3)/Pt(6)	SiN	*0.15–0.025*	*0.15–0.33*	−	Nembach *et al.* (2015)
Co_2FeAl(0.9 − 1.8)	Ta(2)/Ir(4)	Ti(2)	*0.5–0.3*	0.37*	−	Belmeguenai *et al.* (2018)
Fe(3)	SiO_2 MgO(5)	Pt(4)	0.22 0.35	*0.67* *1.05*	+ +	Zhang *et al.* (2018)
Py(5)		$Cu_{1-x}Pt_x$(6)[b]	0–0.05	*0–0.27*	+	Belmeguenai *et al.* (2019)
$Co_{90}Fe_{10}$(1)/oxide[c]	Ta(3)/Pt(6) Ta(3)/Cu(6)	Cu(3)/Ta(2)	*1.29–1.65* −0.02–0.26	*2.52* *0.4*[d]	− −	Nembach *et al.* (2020)
YIG(10)	GGG substrate		0.01	*0.1*		Wang *et al.* (2020)
[Py(1)/Pt(1)]$_{10}$	Ta(5)/Pt(6)	Au(3)	0.032	*0.032*	−	Ahmadi *et al.* (2020)
Fe(3)	SiO_2(4) SiO_2(4)/Pt(4) SiO_2(4)/Au(4) SiO_2(4) SiO_2(4)/Au(4) SiO_2(4)/Pt(4)	Pt(4) SiO_2(4) SiO_2(4) Au(4) Pt(4) Au(4)	0.25 0.33 0.07 0.07 0.4 0.17	*0.75* *1* *0.21* *0.21* *1.2* *0.51*	+ − + + + −	Zhang *et al.* (2021)

[a] This value was calculated according to the definition of D used in this review from the original value $\overline{D}$ by $D = \bar{D}a/(\sqrt{2}d)$, where $a = 0.248$ nm is the lattice constant of Py.

[b] $x = 0\%$, 6.6%, 28%, 45%, 75%, and 100%.

[c] Oxidation is 0–1000 s at 99% Ar and 1% O_2.

[d] The value refers to the longest oxidation of 1000 s.

left-handed (right-handed) handed chirality is favored by the DMI. This means that, in the presence of a positive (negative) value of D, in the measured BLS spectra the absolute frequency of the anti-Stokes (Stokes) peak is higher (lower) than that of the Stokes (anti-Stokes) one, and as a consequence f_{DMI} assumes positive (negative) values, as illustrated in the lower panels of Fig. 20. Please note that if the direction of the applied magnetic-field is reversed, f_{DMI} changes sign due to the reversal of the SW chirality.

Comparisons of the values and the signs of the DMI constants measured using BLS for Co, CoFeB, and a collection of different magnetic materials are reported in Tables XIV–XVII. When the values were not explicitly given in the original publication, we have calculated or extracted them from the figures and reported them in italics. Note that the signs in the tables are consistent with the conventions of the axis, field, D, k vector, and frequency difference described in Figs. 17 and 20. If the authors used a different coordinate system and/or method of calculating the frequency asymmetry, we recalculated the sign according to our convention.

Many have discussed the dependence of the DMI constant as a function of the ferromagnetic layer thickness (Belmeguenai *et al.*, 2015; Stashkevich *et al.*, 2015; Chaurasiya *et al.*, 2016; Kim, Kim, and Choe, 2016) and a possible correlation with surface anisotropy (Stashkevich *et al.*, 2015) or Heisenberg exchange (Nembach *et al.*, 2015). Theoretically, a $1/d$ dependence of the DMI constant is predicted (Kostylev, 2014), as is the case for all interface phenomena, and this makes it difficult to distinguish among the different phenomena. Sometimes a change in slope of the DMI constant versus $1/d$ is observed (Cho *et al.*, 2015; Belmeguenai *et al.*, 2016, 2018; G. W. Kim *et al.*, 2018). Belmeguenai *et al.* (2018) discussed different origins of this change. The first is a coherent-incoherent growth mechanism transition at a certain thickness accompanied by magnetoelastic anisotropy changes. Others are changes in surface roughness that are causing in-plane demagnetizing magnetic fields. Another is interdiffusion and mixing at the interfaces, which reduces the interface anisotropy. According to the experimental results, we conclude that the first hypothesis is the most probable.

Similarly, the dependence of the DMI on the heavy metal thickness has been studied for both Co (Kim, Han *et al.*, 2017) and CoFeB (Tacchi *et al.*, 2017; Chen, Zhang *et al.*, 2018) films in contact with a Pt layer. For both systems the DMI intensity was found to increase with the Pt thickness d_{Pt}, reaching a saturation value when d_{Pt} approaches the Pt spin diffusion length (about 2 nm). This behavior has been explained by analytical calculations assuming that several Pt atoms belonging to different layers in the heavy metal can contribute to the strength of the interfacial DMI (Tacchi *et al.*, 2017). On the contrary, Ma *et al.* (2017) observed the DMI

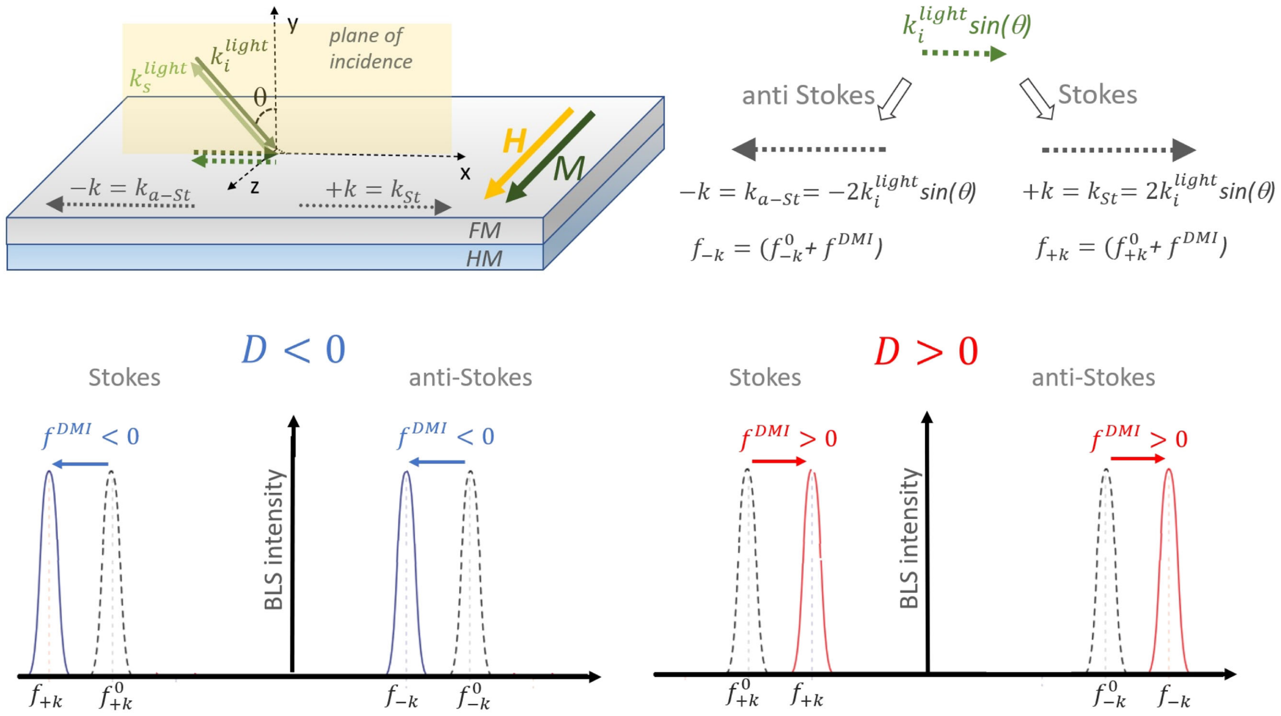

FIG. 20. Schematic diagram of the BLS interaction geometry. k_i^{light} and k_s^{light} represent the wave vectors of the incoming and the backscattered light. Owing to the conservation of the wave vector component parallel to the surface of the specimen, the length of the wave vector of the SW involved in the scattering process is $2k_i^{\mathrm{light}}\sin(\theta)$, as shown in the upper right panel. SWs propagating along the $+k$ $(-k)$ direction correspond to those involved in the Stokes (anti-Stokes) process, i.e., in the generation (annihilation) of a magnon. Bottom panels: typical BLS spectra in the absence of a DMI (dashed line) and with a DMI (solid line) for positive or negative values of D (i.e., of f_{DMI}), respectively.

strength in the IrMn/CoFeB system to increase even for IrMn layers thicker than the IrMn spin diffusion length (about 0.7 nm). They claimed that this DMI enhancement can be ascribed to the reduction of the thermal fluctuations of the antiferromagnetic (AFM) spin arrangement when the IrMn thickness increases, suggesting a different microscopic origin with respect to HM/FM systems.

The sign of the DMI constant was investigated for several material combinations by changing both the stacking order and the multilayer composition (Cho *et al.*, 2017). In systems with a Pt (W) underlayer, negative (positive) values of the DMI constant have been found with an overall agreement, indicating that a left-handed (right-handed) chirality is favored. In agreement with the theoretical calculations, it has also been observed that the sign of the DMI is reversed when the stacking order is inverted, while its value becomes negligible in symmetric structures where a FM film is sandwiched between two identical HM layers. On the contrary, the DMI sign induced by other materials, such as Ir or IrMn, is still the subject of controversial debate in the literature; see Ma *et al.* (2017), Belmeguenai *et al.* (2018), and Ma *et al.* (2018). However, most experimental work contradicts the theoretical prediction of Ir, leading to opposite DMI signs with respect to Pt (Yang *et al.*, 2015). Recently the influence of electric fields on DMI strength has been investigated in Ta/FeCoB/TaO_x trilayers (Srivastava *et al.*, 2018). A strong variation of the D value has been observed and attributed to the dependence of the DMI at the CoFeB/oxide interface on its oxidation state, which can be electrically tuned. In one of the Co articles, Khan *et al.* (2018) investigated the effect of exchange bias with an AFM overlayer on Co and confirmed that a DMI is not influenced by exchange bias or the AFM spin order. Finally, the sinusoidal dependence of the frequency nonreciprocity as a function of the angle between the sample magnetization and the SW wave vector, which was theoretically predicted by Cortés-Ortuño and Landeros (2013), has been experimentally verified for different multilayer structures (Zhang *et al.*, 2015; Kim, Kim, and Choe, 2016; Cho *et al.*, 2017; Tacchi *et al.*, 2017; Belmeguenai *et al.*, 2018).

Notice that several studies were able to correlate the presence of a sizable DMI not only to the frequency position of the BLS peaks but also to their linewidth, i.e., to the damping that affects spin waves. Di *et al.* (2015b) previously studied the interfacial DMI in an in-plane anisotropic Pt(4 nm)/Co(1.6 nm)/Ni(1.6 nm) film using Brillouin spectroscopy, showing that the measured linewidths of counterpropagating magnons are different, with the difference being more pronounced for larger wave vectors. This could be ascribed to a DMI-induced term that is antisymmetric in the wave vector. Moreover, analytical calculations showed that, owing to the existence of the DMI, the magnon linewidth is no longer a monotonic function of frequency. Chaurasiya *et al.* (2016) observed asymmetry in the peak frequency, peak intensity, and magnon lifetimes in W/CoFeB/SiO_2. In addition, in this case the linewidth for spin-wave propagation in the $+k$ direction is smaller than that for spin-wave propagation in the $-k$ direction, indicating different lifetimes of magnons propagating in opposite directions induced by the DMI. More recently a correlation between the DMI strength and the SW damping was demonstrated by combined FMR and BLS investigations in different kinds of systems, such as $[\mathrm{Pt}(1.5\ \mathrm{nm})/\mathrm{Co}(d)/\mathrm{W}(1.5\ \mathrm{nm})]_N$ multilayers (Benguettat-El Mokhtari *et al.*, 2019), $\mathrm{Py}(5\ \mathrm{nm})/\mathrm{Cu}_{1-x}\mathrm{Pt}_x$ bilayers (Bouloussa *et al.*, 2019), and He^+ irradiated Ta/CoFeB/MgO films (Diez *et al.*, 2019b).

Recently W.-Y. Kim *et al.* (2019), Arora, Shaw, and Nembach (2020), Lin *et al.* (2020), and Nembach *et al.* (2020) reported that a sizable interfacial DMI can also arise at the interface between an oxide layer and a ferromagnetic one. Arora, Shaw, and Nembach (2020) and Nembach *et al.* (2020) demostrated that both the magnitude and the sign of the interfacial DMI can be tuned by changing the thickness and the composition of the oxide layer adjacent to the ferromagnetic film. Moreover, Lin *et al.* (2020) showed that in the $\mathrm{BaTiO_3}$ (BTO)/CoFeB system the DMI strength is affected by the termination of the oxide layer ($\mathrm{TiO_2}$ vs BaO). In particular, a higher value of the DMI constant was found for a $\mathrm{TiO_2}$-BTO substrate, and this finding was attributed by first principles calculations to the different electronic states around the Fermi level at the oxide/FM interfaces.

In summary, BLS has rapidly become the most used technique for measuring DMIs using spin waves. A reasonable complexity of the experimental setup and a high accuracy in the determination of the spin-wave dispersion (together with the fact that no external excitation is needed for this technique, which relies on thermal excitation) contributes to the success and increasing use of this technique.

2. Time resolved magneto-optical imaging

TRMOKE allows propagating spin waves to be detected in real space and as a function of time, enabling the determination of the spin-wave k vector and decay. TRMOKE was employed by Körner *et al.* (2015) in order to determine the DMI in a Pt/Co/Py/MgO multilayer; see Table XVIII. For imaging spatially and time-dependent spin-wave signals, a focused laser pulse (spot size ≤ 300 nm) of $\lambda = 400$ nm and a pulse length of ≈ 200 fs (repetition rate 80 MHz) is used. The laser pulses are phase locked to a microwave generator connected to a coplanar wave guide (CPW) or microwave antenna deposited on top of the thin film sample, as shown in Fig. 21. The excited k vectors are in the range of $2 - 10\ \mu\mathrm{m}^{-1}$. The dynamic out-of-plane magnetization is detected via the MOKE along the direction normal to the CPW up to a distance of 5 μm from the center of the CPW. The spin-wave dispersion is determined using the expression given by Moon *et al.* (2015). The Co film is 0.4 nm thick and has a PMA. During the measurement it is magnetized in plane parallel to the CPW. Owing to its low damping, the 5 nm Py film on top of Co facilitates the SW propagation. Damon-Eshbach modes are detected at various distances from the CPW. Therefore, it is possible to detect with this technique not only frequency and amplitude nonreciprocity but also a nonreciprocity in attenuation length of the spin waves, as predicted by theory.

TABLE XVIII. Overview of DMI measurements of various FM materials via spin-wave methods other than BLS. Körner *et al.* (2015) used TRMOKE, Zakeri *et al.* (2010) and Tsurkan and Zakeri (2020) used SPEELS, Küß *et al.* (2020) used MASW spectroscopy, and all the others employed PSWS. FM and NM stand for ferromagnetic and nonmagnetic layers, respectively. D is the interfacial DMI constant and $D_s = Dd$, with d the thickness of the ferromagnetic film. Numbers in roman were quoted in the reviewed papers, while numbers in italics were either extracted from figures or calculated using the parameters provided. Signs with $*$ are given according to the convention used in this review and are the opposite of that in the original manuscript.

FM (nm)	Bottom NM (nm)	Top NM (nm)	D (mJ/m^2)	D_s (pJ/m)	Sign	Reference
Fe(2 MLs)[a]	W(110) single crystal		3.95 ± 0.6[b]	*1.36 ± 0.2*[c]	+	Zakeri *et al.* (2010)
Co(0.4)/Py(5)	Ta(2)/Pt(2)	MgO(5)	0.16	0.89	−	Körner *et al.* (2015)
Co(14 − 20)	Ta(3)/Pt(3)	MgO(1.8)/Ta(3)	*0.19–0.26*	*3.62–4.08*	−	Lee *et al.* (2016)
	Ta(3)/MgO(1.8)	MgO(1.8)/Ta(3)	*0.03*	*0.54*	−*	
	Ta(3)/MgO(1.8)	Pt(3)/Ta(3)	*0.11–0.17*	*2.1–2.55*	+*	
Py(6)	$\mathrm{Al_2O_3}$(21)	$\mathrm{Al_2O_3}$(5)	*0.007*	0.04	−	Gladii *et al.* (2016)
Co(20)	Ta(2)/Pt(3)	MgO(2)	0.45	*9*	−*	Kasukawa *et al.* (2018)
Co(4 − 26)	Ta(4)/Pt(4)	Ir(3)/Pt(2)	…	1.0 ± 0.2	−	Lucassen *et al.* (2020)
	Ta(4)/Pt(4)	Pt(3)/Pt(2)		0.1 ± 0.04	−	
	Ta(4)/Ir(4)	Pt(3)/Pt(2)		1.0 ± 0.2	+	
Py(4 − 20)	Ti(5)	Pt(5, 10)		0.25	+	Gladii *et al.* (2020)
YIG(10)	GGG substrate		0.0099 ± 0.0019	*0.1*		Wang *et al.* (2020)
Fe/Co (ML)[a]	W(110) single crystal		6.55 ± 0.7	2.25 ± 0.25[c]	+	Tsurkan and Zakeri (2020)
$\mathrm{Co_{40}Fe_{40}B_{20}}$(2)	$\mathrm{LiNbO_3}$	Pt(3)	0.424 ± 0.001	*0.85 ± 0.002*	+*	Küß *et al.* (2020)

[a] ML, atomic monolayer.

[b] The value in SI units was taken from the Supplemental Material of Tsurkan and Zakeri (2020), while the original work reports D in meV.

[c] The value was obtained assuming a ML thickness of 1.72 Å.

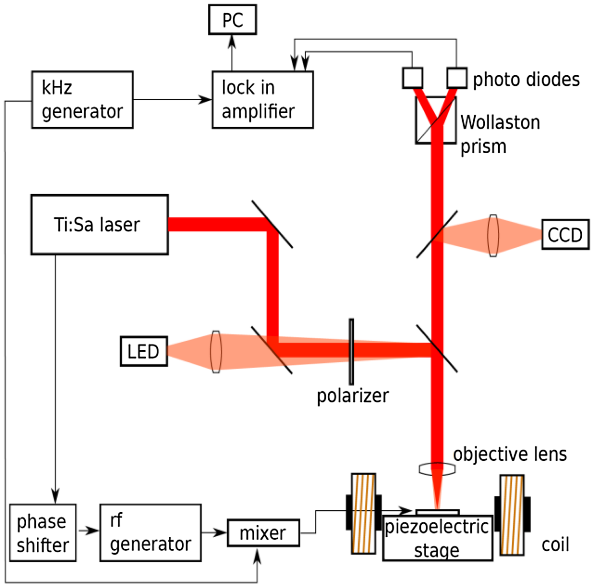

FIG. 21. Scheme of a time resolved magneto-optic Kerr effect experiment. The pulse train of a femtosecond laser system is synchronized to the sinusoidal excitation field that is generated by sending a microwave current through a coplanar wave guide. The change of polarization of the reflected light is analyzed in an optical bridge and sent to a lock-in analyzer synchronized to a microwave mixer or chopper.

Apart from the necessity of a pulsed laser system, the complexity of a TRMOKE experiment is comparable to BLS as far as the optical signal acquisition is concerned. However, SWs need to be excited by a CPW, which has to be prepared by lithography directly on top of the sample. The k vectors that can be excited are limited by the CPW geometry. Broadband excitation can be obtained with a single line [as done by Ciubotaru *et al.* (2016)], with the drawback being that the amplitude is reduced with respect to a monochromatic excitation. Since high k values are preferable, the CPW lines have to be narrow (<1 μm), which requires electron beam lithography (EBL). Boundary conditions for the generation of plane waves have to be taken into account, and it is preferable to have stripes of magnetic material; see the Supplemental Material of Chauleau *et al.* (2014). The Gilbert damping strongly limits the technique (Bauer *et al.*, 2015) since the attenuation length with a large damping parameter becomes too small for the SW to be detectable, which is a significant drawback with respect to BLS.

3. Propagating spin-wave spectroscopy

PSWS is a tool to characterize spin waves excited in magnetic thin films by measuring the dispersion relation and group velocity all electrically using a standard high-frequency (HF) instrument, a vector network analyzer (VNA) (Schilz, 1973; Stamps and Hillebrands, 1991; Bailleul *et al.*, 2001). It was widely applied in the field of magnonics (Neusser *et al.*, 2010). As depicted in Fig. 22, the VNA emits HF signals in antenna 1 and receives the transmitted and reflected signals in antennas 2 and 1, respectively (and vice versa). The mutual inductance spectra are obtained from the transmission and reflection coefficients. The inductance spectra show a shift in frequency in the presence of a DMI (see Fig. 23) from which D is directly obtained through Eq. (3.12). To date there are only a few published experimental works that have applied PSWS to measure the DMI constant; see Table XVIII.

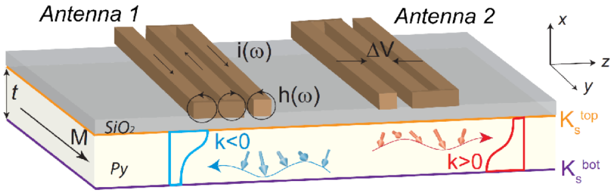

FIG. 22. Scheme of the PSWS measurement. The two antennas are emitting and receiving HF signals from a VNA, which generates spin waves with an antenna specific k-vector distribution. Applying an in-plane magnetic field parallel to the antenna and focusing on spin waves with k perpendicular to it, one observes an absorption in the signal due to the Damon-Eshbach (surface) modes that travel preferentially on one of the film surfaces contributing with different anisotropies (K_s^{bot} and K_s^{top}). From Gladii *et al.*, 2016.

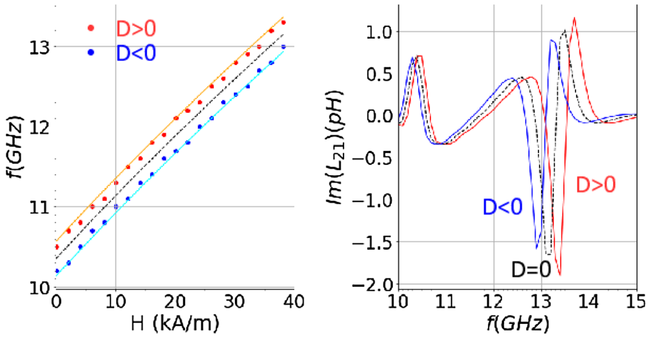

FIG. 23. Left panel: frequency shift with respect to the applied magnetic field. The black dashed line is the calculated Damon-Eshbach frequency with $D = 0$. Right panel: shift of the mutual inductance spectra with D. The plot was obtained from numerical calculations based on the Landau-Lifshitz-Gilbert approach with the use of the surface permeability (Emtage, 1978) on a magnetic film (saturation magnetization $\mu_0 M_s = 1.70$ T, damping $\alpha = 0.012$, film thickness $d = 10$ nm, and $D = \pm 0.5$ mJ/m^2) for an antenna with an excitation maximum for a wave vector of $k_{\mathrm{max}} = 10.4$ μm^{-1}.

Lee *et al.* (2016), who were among the first to apply PSWS, excited spin waves by a meander-shaped CPW [similar to that discussed by Vlaminck and Bailleul (2010)] and detected them in a second CPW at a certain distance, and thus measured the spin-wave dispersion and group velocity using a VNA (Bailleul, Olligs, and Fermon, 2003). The measured magnetic multilayers are chosen as Pt/Co/MgO, MgO/Co/Pt, and MgO/Co/MgO in order to compare samples with positive and negative DMI constants to one with a vanishing DMI. The films were patterned into 8-μm-wide stripes, and a 40-nm-thick AlO$_x$ layer for electric insulation was deposited on top. The CPW consisted of Ti(5 nm)/Au(150 nm) and was realized with a primary spatial period of 800 nm ($k = 7.85$ μm^{-1}) and a subsidiary spatial period of

2250 nm ($k = 2.8\ \mu\mathrm{m}^{-1}$). The Co thickness d was changed from 14 to 20 nm. The DMI constant is considered here to be a pure interface effect with a characteristic length $\lambda = 0.25$ nm, so the interfacial DMI D_i is calculated to be $D = D_i\lambda/d$. Assuming that $D_i\lambda$ remains constant, Lee *et al.* (2016) obtained a value $D = 1.8\ \mathrm{mJ/m^2}$ for a Co thickness of 2 nm.

Kasukawa *et al.* (2018) investigated a similar film Ta(2 nm)/Pt(3 nm)/Co(20 nm)/MgO(2 nm) for electric field effects. Modulations of spin-wave frequency were obtained by the gate electric field and the electric field dependence of the DMI was calculated to be 2 ± 0.93 fJ/V m. The interfacial DMI was obtained at zero electric field and calculated to be $0.45 \pm 0.15\ \mathrm{mJ/m^2}$. The value calculated for D_s, as defined in this review, is high compared to other techniques. They reasoned that the measured frequency shifts are not caused by the effects of different interfacial anisotropies at the Pt/Co and MgO/Co interface, since no magnetic-field dependence was observed. Therefore, they attributed the entire Δf to the interfacial DMI. However, it appears that the measured value is overestimated in this way.

Lucassen *et al.* (2020) investigated Ta(4 nm)/X(4 nm)/Co(d)/Y(3 nm)/Pt(2 nm) stacks with $d = 4$–26 nm and $(X, Y) = (\mathrm{Pt, Ir}), (\mathrm{Ir, Pt})$ by meander-type CPWs with wave vectors $k = 4, 5.5, 7, 8.5, 10\ \mu\mathrm{m}^{-1}$. Changing the Co thickness in such a wide range leads to a gradual transition between different Co phases, and therefore a change in volume anisotropy in the different samples has to be considered. A detailed analysis of the frequency nonreciprocity due to DMI considering surface anisotropy and changes in volume anisotropy is performed. In addition, Gladii *et al.* (2016, 2020) (see Fig. 24) performed an analysis of the influence of a difference in surface (interface) anisotropy on both sides of a Permalloy film on the SW dispersion. They calculated the frequency nonreciprocity due to different surface anisotropies while revisiting the approach of Kalinikos and Slavin (1986). The important result of the paper is that the frequency nonreciprocity due to a difference in surface anisotropies scales as d^2, where d is the thickness of the FM film, while the contribution due to DMI scales with d^{-1}. In this approach, the exchange spin waves play an important role, and a purely magnetostatic approach would lead to unrealistic modal profiles. Gladii *et al.* (2020) additionally measured the spin-wave relaxation rate using two CPWs as emitter and detector at different distance. An injected dc current in the Pt layer induced STT via the spin Hall effect and linearly altered the spin-wave relaxation time. From this it was possible to obtain additional information such as the spin Hall conductivity.

Recently Wang *et al.* (2020) investigated interfacial DMI at an oxide-oxide interface, here yttrium iron garnet (YIG)/gadolinium gallium garnet (GGG). This so-called Rashba- (or ISGE-) induced DMI was recently observed by Avci *et al.* (2019) and Ding *et al.* (2019). There YIG films with thicknesses 7,10, 20, 40, and 80 nm on a GGG substrate were measured using PSWS, and the DMI constant was calculated from the asymmetric group velocities. The values were comparable to the ones obtained from BLS.

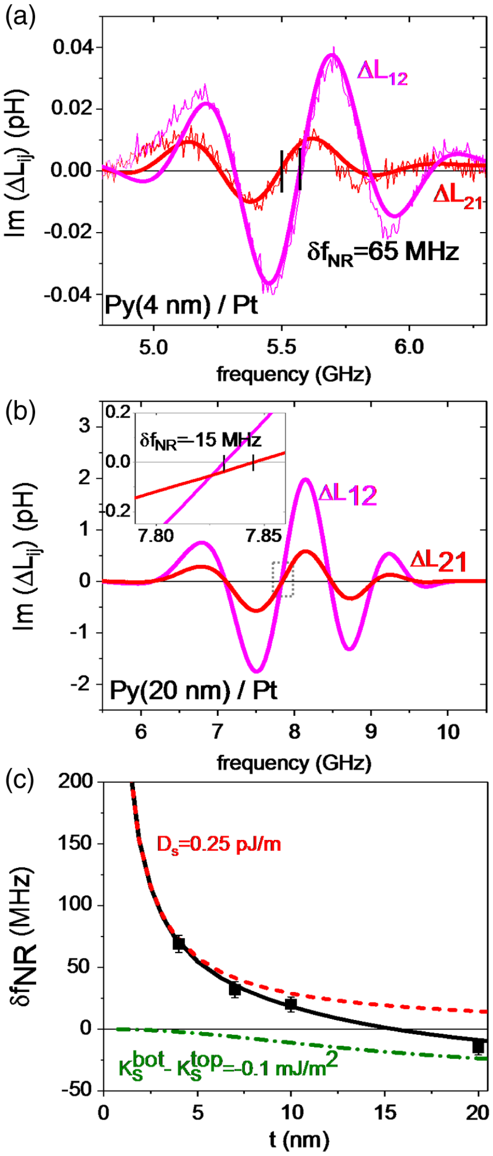

FIG. 24. (a),(b) Mutual inductance spectra of Py/Pt bilayers measured at $\mu_0 H = 37$ mT for spin waves with $k < 0$ and $k > 0$. The frequency of the left-moving spin wave is shifted with respect to the frequency of the right-moving one with a difference δf_{NR}. (c) Frequency nonreciprocity as a function of the Py thickness. The dashed and dash-dotted lines are the frequency nonreciprocity contributions induced by the DMI and magnetic anisotropy asymmetry, respectively. From Gladii *et al.*, 2020.

Küß *et al.* (2020) recently employed a technique that, as in PSWS, exploits the SW nonreciprocity in the presence of a DMI; see Table XVIII. The magnetoacoustic spin-wave (MASW) measurement is experimentally similar to PSWS using a VNA for the detection of the MASW absorption, although it was based on a slightly different physical principle. Via antennas connected to the VNA, surface acoustic waves (SAWs) are excited in LiNbO$_3$/CoFeB(1.4–2 nm)/Pt(3 nm) heterostructures which couple to the SWs and generate MASWs with frequencies depending on the DMI; see Fig. 25. As in a PSWS experiment the D value is obtained from the frequency shift between SWs traveling in opposite directions. The nonreciprocity in the resonant field is caused by the DMI as well as the reduced coupling efficiency

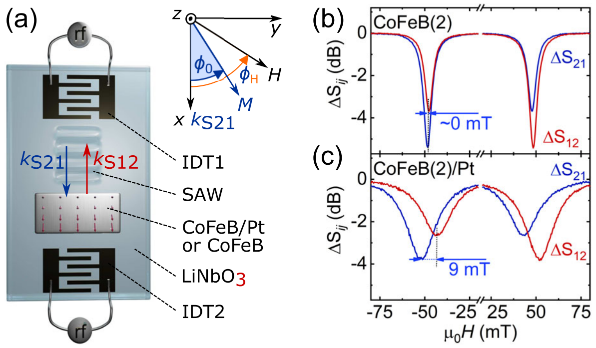

FIG. 25. (a) Scheme of the experimental setup, the sample, and the coordinate system of the magnetoacoustic spin-wave (MASW) measurement. The transmission coefficients S_{21} and S_{12} for the oppositely propagating surface acoustic waves (SAWs) with wave vectors k_{S21} and k_{S12} are measured by a VNA. (b) SAW transmission signal of CoFeB(2 nm). (c) SAW transmission signal of CoFeB(2 nm)/Pt. CoFeB(2 nm)/Pt shows nonreciprocities both in the transmission amplitude at resonance and in the resonant magnetic field. From Küß *et al.*, 2020.

due to the SAW-SW helicity mismatch for opposite propagation directions.

In summary, the electric SW measurement is straightforward and only commercially available equipment is required. Among the SW techniques it has a good frequency resolution of a few megahertz. As in the TRMOKE experiments, the excitation of SWs is performed by CPWs, which have to be prepared by EBL in order to obtain high wave numbers and, therefore, larger DMI signals. Usually only a few wave vectors are available since each wave vector requires its own CPW geometry and values are limited to about 10 $\mu\mathrm{m}^{-1}$ using conventional techniques. Only sophisticated techniques allow higher values to be reached (Liu *et al.*, 2018). A second CPW is used for detecting the spin-wave signal and the signal-to-noise ratio is generally low, so only thick FM films (>20 nm) give a clear, easily measurable signal. However, the resonance frequency can also be extracted well from a noisy signal. More problematic is the analysis of an amplitude nonreciprocity. Since the FM films are thick, using $D_s = Dd$ gives much larger values than other techniques. This may be due to the fact that D_s is not well estimated, since large differences of surface properties might occur. To avoid the D_s concept, Lee *et al.* (2016), like Kostylev (2014), attributed the measured DMI value D_i only to a thin layer (monolayer or layer of a characteristic length) close to the interface. This delivers values for an effective D value comparable to other techniques but depends on the arbitrary choice of the characteristic length. However, while it is shown in several works that the $1/d$ dependence does not hold for thicker samples [see Nembach *et al.* (2015)], the PSWS method particularly confirms this, first because ultrathin films are difficult to be measured, and second because the surface character of the Damon-Eshbach waves might play a role.

4. Spin-polarized electron energy loss spectroscopy

Following the theoretical work of Udvardi and Szunyogh (2009), the spin-wave dispersion asymmetry due to DMI was first measured by SPEELS on a double layer of Fe(110) grown on a W(110) single crystal (Zakeri *et al.*, 2010); see Table XVIII. A monochromatized spin-polarized electron beam is scattered from the sample and the energy loss or gain as a function of in-plane momentum transfer is measured. Minority electrons create surface SWs through a virtual spin flip scattering process and lose energy, while majority electrons may annihilate thermally excited SWs and gain energy. One measures a peak in the minority spin channel in the energy loss region and a peak in the majority spin channel in the energy gain region (analogous to the Stokes and anti-Stokes peak in BLS) (Zakeri, 2017). At an electron energy of 4.163 eV (resolution, 19 meV) a wave vector of $\pm 0.5-1$ Å^{-1} is employed by changing the angle of the incident beam. A small SW dispersion asymmetry is expected due to Damon-Eshbach surface modes of about 0.1 meV. The energy difference for $\pm k$ is evaluated by inverting the magnetization direction. The modulus of the DMI vector is 0.9 meV for first neighbors and 0.5 meV for second neighbors. With an interatomic distance of $a = 3.16$ Å and a monolayer thickness of 1.72 Å, a value of $D = 3.95 \pm 0.6$ mJ/m^2 is obtained. Recently Tsurkan and Zakeri (2020) took up the technique again to investigate Co/Fe bilayers with $\mathbf{C}_{2v}$ symmetry on W(110) and compared their findings to the previous results. The fundamental role of the crystal symmetry is demonstrated, resulting in an extraordinarily high DMI. With a thickness of 2×1.72 Å, a value of $D = 6.55 \pm 0.7$ mJ/m^2 is obtained.

The main advantage of SPEELS is that the wave vector $k = 500 - 1200$ $\mu\mathrm{m}^{-1}$ is hundreds of times larger than it is for the previously mentioned techniques, thereby allowing one to explore exchange-based spin waves. Since the energy difference of spin waves with opposite k vectors grows linearly with k, the asymmetry detected is about 100 times larger, so even small D constants can be measured. On the other hand, one can recall the necessity of ultrahigh-vacuum conditions and the impossibility of applying magnetic fields. Furthermore, spin-wave energies typically calculated from a Heisenberg model have to take into account the itinerant character of the spins in ferromagnetic metals by effective exchange constants. A quantitative estimation of the effective exchange constants (isotropic J as well as anisotropic D) requires complex *ab initio* approaches combined with spin dynamic simulations (Bergqvist *et al.*, 2013). This is especially valid for monolayers or bilayers of ferromagnets on a heavy metal, as were investigated by SPEELS, where changes in the interlayer and intralayer distances have a nontrivial influence on the exchange parameters (Zakeri, 2017).

D. Advantages and limitations

The main advantage of spin-wave methods for determining the DMI constant is the simple expression for the measurable frequency difference that occurs when the sign of k is changed, as seen in Eq. (3.11). This also means that not only the size but also the sign of the constant can be easily determined, provided that the geometry of the experiment and the polarity of the applied field are specified. However, attention has to be paid to several aspects.

As is the case for DW methods, the saturation magnetization should first be determined by external means, such as vibrating sample magnetometry or superconducting quantum interference device magnetometry. The gyromagnetic factor and the anisotropy constants can then be obtained by either FMR or BLS measurements as a function of the intensity and the direction of the external field. Furthermore, the thickness of the magnetic active layer has to be evaluated correctly in the derivation of D_s from the measurement of ω_{DMI}. It does not always coincide with the nominal layer thickness due to interlayer mixing (dead layer) (Belmeguenai *et al.*, 2018) or proximity effects (Rowan-Robinson *et al.*, 2017). Finally, ω_0 in Eq. (3.11) is considered to be independent of the sign of k. This is generally the case, but when comparing different samples (such as those with different thicknesses), this might be not completely true, for example, due to different surface-interface anisotropies at both sides of the magnetic film that influence differently the $\pm k$ spin waves and lead to $\Delta\omega_0 = \omega_0(k) - \omega_0(-k) \neq 0$. Therefore, such a difference is necessarily reflected in the measured frequency asymmetry. This problem stems from the fact that DE waves travel on opposite surfaces in opposite k directions (Camley, 1987), and therefore any difference in magnetic properties at the two surfaces, such as surface anisotropy, will be reflected in a nonreciprocity of the spin-wave spectra. Through comparisons with theoretical models and the correct measurement procedure, their contribution has to estimated as well as possible. For example, the asymmetry due to differences in surface anisotropy or asymmetry in saturation magnetization M_s was evaluated by Di *et al.* (2015b) by additionally measuring a Pt/Co/Ni sample, a Co/Ni, and a Co/MgO/Ni sample. While in the latter $\Delta\omega_0$ is negligible (meaning that the contribution due to asymmetry in M_s is negligible), the former shows an opposite sign of $\Delta\omega_0$ with respect to the Pt/Co/Ni sample. This means that the two interfaces have different contributions from either anisotropy or the DMI, but that a major role is played by the Pt/Co interface with an opposite sign with respect to the Co/Ni interface.

Surface effects usually scale as $1/d$ (Hillebrands, 1990; Stamps and Hillebrands, 1991), which might make one question how to distinguish DMI-related nonreciprocity from other surface or interface effects. However, the frequency shifts due to DMI and surface anisotropy are intrinsically different. As Gladii *et al.* (2020) showed, they have different dependencies on d, as the first is proportional to $1/d$ and the second is proportional to d^2. Furthermore, the first depends linearly on k, while the second has a more complex dependence but usually decreases with k (Gladii *et al.*, 2016). The wave vector dependence of the frequency shift due to the surface anisotropy is stronger for thicker films, while the one induced by the DMI is larger for thinner films; see the Supplemental Material of Lucassen *et al.* (2020). This creates the possibility of distinguishing among the different contributions depending on the value of k, having available films of different thickness.

It was shown by numerical calculations and experimentally by Stashkevich *et al.* (2015) that for thin films ($d_{\mathrm{Py}} < 8$ nm) the SW nonreciprocity due to the surface anisotropy is negligible with respect to that induced by DMI, while for thicker films both contributions have to be considered. On the basis of these arguments, in the literature it is usually thought that at $kd \ll 1$ any dependence of ω_0 on the sign of k can be neglected (Nembach *et al.*, 2015) and that, in the absence of a DMI, the $\pm k$ spin waves are subjected to an average magnetic energy that is equal at both sides of the magnetic film (Soohoo, 1963).

Care has to be taken with respect not only to frequency nonreciprocity but also to amplitude nonreciprocity. In addition, here there might be effects due to different boundary conditions at the interfaces of the ferromagnetic film. For example, a metallic boundary condition at one side would strongly attenuate the spin wave traveling close to it. Furthermore, methods such as PSWS show an amplitude nonreciprocity due to the fact that the CPW couples more to one wave vector than to the other due to the symmetry of the CPW (Serga, Chumak, and Hillebrands, 2010).

Probably the strongest experimental limitation of the methods based on spin waves is that the sample has to be magnetized in plane in order to be able to detect DE modes. Therefore, for samples with strong out-of-plane anisotropy (that is, PMA) it is necessary to apply a sufficiently high in-plane field, which can be experimentally difficult. Furthermore, ultrathin PMA films give rise to a low signal-to-noise ratio, due not only to their thickness but often also to the high damping, so fitting procedures may have large uncertainties. This sets a lower limit to the values of D that may be measured by spin-wave methods, and therefore these may be considered reliable for either magnetic film thicknesses above a certain threshold or with low damping or a high DMI constant.

IV. SPIN-ORBIT TORQUE METHOD

A. Method overview

When a charge current is applied to a HM/FM bilayer, spin-torque effects occur due to the strong spin-orbit interaction at the interface. A charge current J_e flowing in the HM along the x axis will generate a transverse spin accumulation $\vec{\sigma}$ along the y direction through the spin Hall effect and/or the inverse spin galvanic effect (Manchon *et al.*, 2019). The spin accumulation acts on the magnetic moment $\vec{M}$ and results in an effective dampinglike magnetic field $\vec{H}_{\mathrm{eff}} \approx \vec{\sigma} \times \vec{M}$. Of particular interest is the out-of-plane effective magnetic field $H_{\mathrm{eff},z}$ induced at the Néel DW (Pai *et al.*, 2016). As shown in Fig. 26, $H_{\mathrm{eff},z}$ depends on the angle φ between the DW moment and the x axis and can be quantitatively written as $H_{\mathrm{eff},z} = \chi_{\mathrm{DL}} J_e \cos\varphi$ [which effectively represents Eq. (2.2)], where the charge-to-spin conversion efficiency (effective dampinglike field per unit current density) $\chi_{\mathrm{DL}} = \hbar\xi_{\mathrm{DL}}/2e\mu_0 M_S d$. Here ξ_{DL}, M_S, and d are the effective dampinglike torque efficiency, the saturation magnetization of the FM, and thickness of the FM layer.

B. Theory and models

Pai *et al.* (2016) first proposed a method to simultaneously determine the spin-torque efficiency and DMI field H_{DMI} in HM/FM with PMA based on current assisted DW propagation model. As shown in Fig. 26(a), in the case of a homochiral Néel DW the total field $H_{\mathrm{eff},z}$ acting on the DW magnetization is expected to be zero due to the opposite signs of $H_{\mathrm{eff},z}$ for

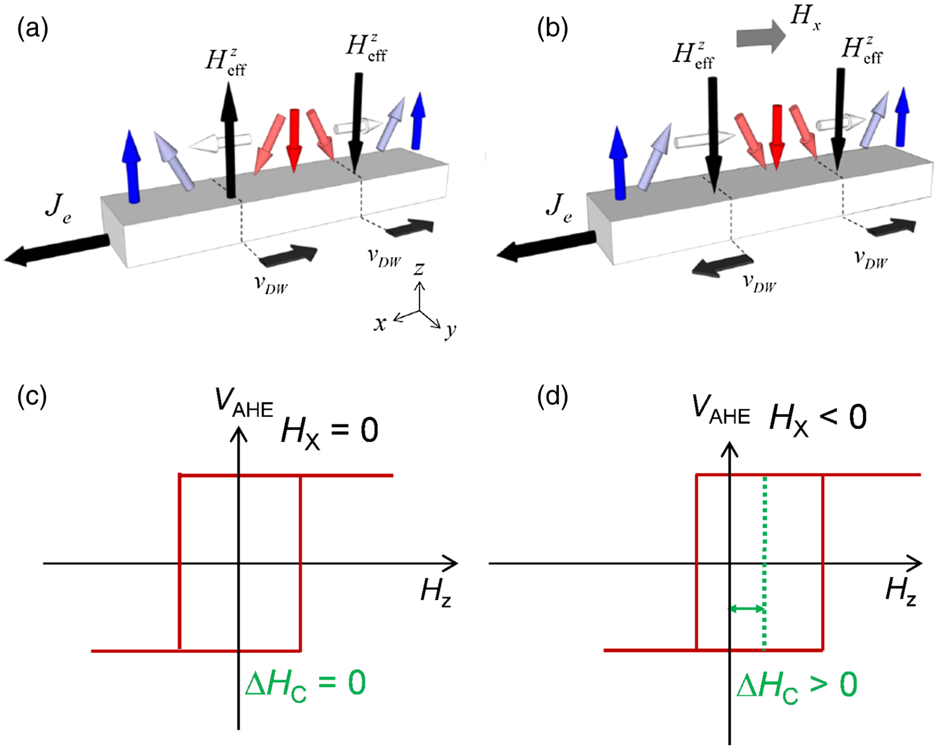

FIG. 26. (a) Schematics of the current-induced effective magnetic field $H_{\mathrm{eff},z}$ at the Néel chiral domain wall in a HM/FM bilayer with perpendicular magnetic anisotropy. In the absence of an external magnetic field, $H_{\mathrm{eff},z}$ at the DW points in the opposite direction ($H_{\mathrm{eff},z} = 0$). Thus, the motion of a domain wall v_{DW} is in the $-x$ direction, and there is no domain expansion. (b) In the presence of an external magnetic field H_x large enough to align the Néel DW alongside H_x, the induced $H_{\mathrm{eff},z}$ points in the same direction, which leads to domain expansion due to the domain-wall motion in opposite directions. (a),(b) From Pai *et al.*, 2016. (c) In the absence of H_x, there is no shift of the anomalous Hall loop. (d) However, a shift of the anomalous Hall loop is expected with the application of H_x, which provides a measure of the DMI and the spin-torque efficiency.

up-to-down ($\cos\varphi = 1$) and down-to-up ($\cos\varphi = -1$) DWs. In this case, the opposite $H_{\mathrm{eff},z}$ at the DWs move the domain in the same direction and there is no domain expansion. However, when an external in-plane magnetic field H_x is applied that is large enough to overcome H_{DMI}, the magnetization in the walls align parallel to H_x as shown in Fig. 26(b), and the resulting total $H_{\mathrm{eff},z}$ points in the same direction for both the up-to-down and down-to-up DWs. This leads to the expansion or contraction of domains. The magnitude and the polarity of $H_{\mathrm{eff},z}$ depends on H_x and J_e, i.e., $H_{\mathrm{eff},z}(H_x, J_e)$. Since $H_{\mathrm{eff},z}$ acts as an effective magnetic field for the entire device, it is thus expected that the out-of-plane hysteresis loop of the bilayer can be shifted by $H_{\mathrm{eff},z}$. Therefore, by measuring the shift of the hysteresis loop as a function of H_x and J_e, one can determine the magnitude of H_{DMI} as well as χ. Specifically, H_{DMI} is determined when the DW is fully aligned by H_{sat}, i.e., $H_{\mathrm{DMI}} = H_{\mathrm{sat}}$, and $\chi_{\mathrm{DL}} = H_{\mathrm{eff},z}(H_{\mathrm{sat}}, J_e)/J_e$.

As shown in Fig. 27(a), an anomalous Hall effect (AHE) loop, i.e., an anomalous Hall voltage versus out-of-plane magnetic field, is measured by changing both the magnitude and the polarity of I_e and H_x. Under an in-plane bias field of 0.25 T the AHE loop shifts to the opposite direction at ±6 mA, which indicates an opposite sign of the induced $H_{\mathrm{eff},z}$ due to the SOT. The I_e dependence of the up-to-down switching field $H_{\mathrm{SW,up\text{-}to\text{-}down}}$ and the down-to-up switching field $H_{\mathrm{SW,down\text{-}to\text{-}up}}$ is summarized in Fig. 27(c). Two current-related effects should be considered to explain the switching fields, i.e., the effect of Joule heating and $H_{\mathrm{eff},z}$. Joule heating reduces the coercivity H_C that is proportional to I_e^2, i.e., $H_C(I_e^2)$, while $H_{\mathrm{eff},z}$ is expected to show a linear behavior with respect to I_e, i.e., $H_{\mathrm{eff},z}(I_e)$. Thus, for a fixed I_e the switching field can be written as $H_{\mathrm{SW,up\text{-}to\text{-}down}} = H_{\mathrm{eff},z} + H_C$ for up-to-down switching and $H_{\mathrm{SW,down\text{-}to\text{-}up}} = H_{\mathrm{eff},z} - H_C$ for down-to-up switching. By eliminating the effect of Joule heating, the magnitude of $H_{\mathrm{eff},z}$ can be easily obtained as $H_{\mathrm{eff},z} = (H_{\mathrm{SW,up\text{-}to\text{-}down}} + H_{\mathrm{SW,down\text{-}to\text{-}up}})/2$. As shown in Fig. 27(c), $H_{\mathrm{eff},z}$ scales linearly with I_e, indicating that $H_{\mathrm{eff},z}$ is indeed induced by current-induced spin accumulation due to the interfacial spin-orbit interaction. One can quantify the conversion efficiency using the slope $\chi(H_x, J_e) = dH_{\mathrm{eff},z}/dJ_e$, and Fig. 27(d) shows the magnitude and polarization of χ as a function of the in-plane bias magnetic field along the x and y directions. One can see that χ remains zero with the application of H_y, but χ increases linearly with H_x and saturates at $\mu_0 H_{\mathrm{sat}} = 0.5$ T. This observation is in agreement with the domain expansion picture, where the DW magnetization changes from an average value of $\langle\cos\varphi\rangle = 0$ at $H_x = 0$ to $\langle\cos\varphi\rangle = 1$ when H_x fully aligns with the DW moment, which provides a measure of H_{DMI} with $H_{\mathrm{DMI}} = H_{\mathrm{sat}}$. Moreover, the magnitude of χ_{DL} is obtained when χ saturates, from which one can determine the charge-to-spin conversion efficiency ξ_{DL}.

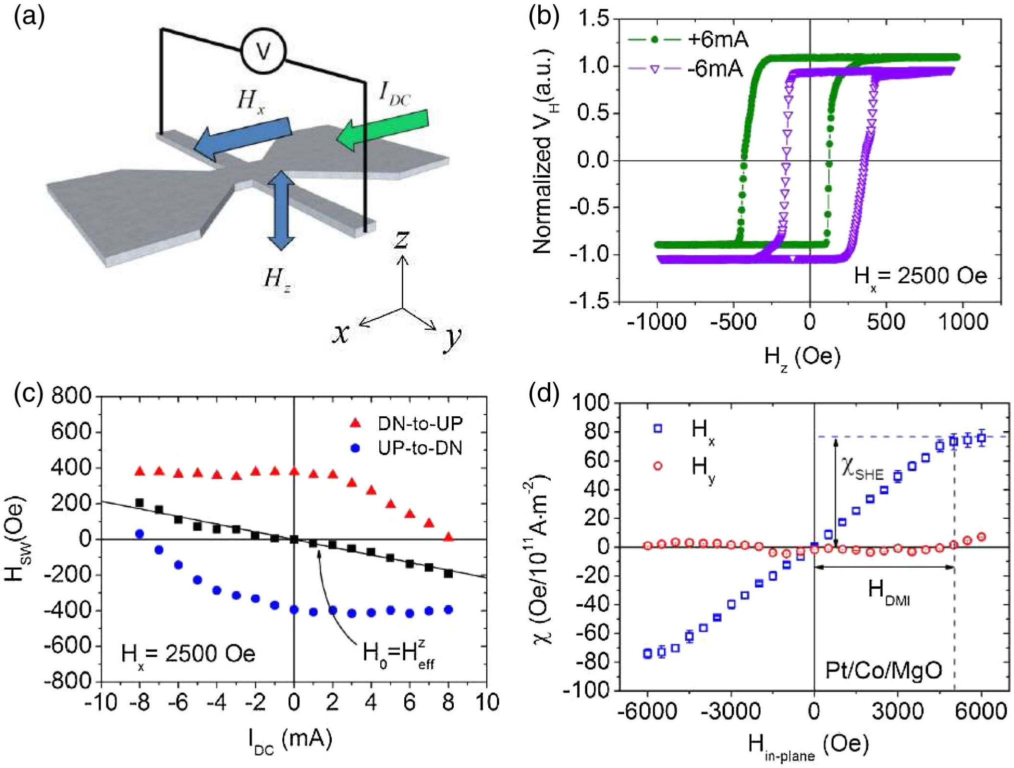

FIG. 27. (a) Schematics of the measurement of the DMI field utilizing the anomalous Hall effect (AHE). (b) AHE loops for Pt(4 nm)/Co(1 nm)/MgO(2 nm) with $I_e = \pm 6$ mA [note that for consistency in the main text we use I_e (J_e) instead of the $I_{\rm dc}$ used in the figure] and an in-plane bias magnetic field $H_x = 0.25$ T. For clarity, slight offsets are introduced for both AHE loops. (c) Switching fields $H_{\rm SW}$ for down-to-up (red triangles) and up-to-down (blue circles) magnetization reversal as a function of I_e. $H_0 = H_{{\rm eff},z}$ represents the average value of the switching fields. (d) Charge-to-spin conversion efficiency as a function of the in-plane bias field for Pt(4 nm)/Co(1 nm)/MgO(2 nm). The blue squares and red circles represent the data obtained with an in-plane magnetic field along the x and y directions, respectively. Note that we use $\chi_{\rm DL}$ in the text instead of $\chi_{\rm SHE}$. From Pai *et al.*, 2016.

C. Experimental results

Data of DMI constants determined using the SOT method are reported in Table XIX. Initially, Pai *et al.* (2016) quantified the magnitude of $H_{\rm DMI}$ in Pt/Co/MgO, Pt/CoFeB/MgO, and Ta/CoFeB/MgO multilayers and demonstrated opposite signs of the spin Hall angle for Pt and Ta. They also showed that a sizable DMI exists in wedged Pt/Co(wedge)/MgO samples, where an additional spin-orbit torque appears due to the lateral structure asymmetry and that can be used for in-plane bias magnetic-field free switching. By inserting a Pt spacer between a Ta and CoFeB interface, Chen, Zhang *et al.* (2018) found that both the spin-torque efficiency and the DMI constant D gradually decrease as the Pt thickness increases to 1 nm. Ishikuro *et al.* (2019) demonstrated that the DMIs at Ir/Co and Pt/Co interfaces show comparable magnitudes with the same sign, leading to a reduced DMI in Pt/Co/Ir trilayers, in agreement with several measurements using BLS and DW methods. Khadka, Karayev, and Huang (2018) showed that the DMI in Pt/Co/Ru trilayers is comparable to Pt/Co/Ir. Yang *et al.* (2021) measured the spin-orbit torque and DMI in [Ni-Co]/Ir heterostructures. By alloying Cr into Pt, Quan *et al.* (2020) recently found that both the spin-torque efficiency and the DMI can be modulated, reaching a maximum at a Cr concentration of about 25%.

Pai *et al.* (2016) found that $H_{\rm DMI}$ in a Pt(4 nm)/Co(1 nm)/MgO(2 nm) stack and a Pt(4 nm)/CoFeB(1 nm)/MgO(2 nm) stack differ by a factor of 2. Since DMI is an interfacial effect, the magnitude of $H_{\rm DMI}$ is expected to be inversely proportional to the thickness of the FM layer. However, no clear experimental results with the SOT method follow this trend, indicating that the DMI can have a complicated relation to the FM thickness. It has been shown in W/FM/MgO structures (FM = CoFeB, FeB) that $H_{\rm DMI}$ changes sign upon increasing the FM thickness (Dohi *et al.*, 2019), indicating that there could be competing mechanisms contributing to the DMI as well as to the interfacial spin-orbit interaction (Cao, Chen *et al.*, 2018; Chen, Chan *et al.*, 2018; Yun *et al.*, 2018).

Recently measurements have demonstrated the presence of DMI in heavy metal/magnetic insulator heterostructures, where the DMI is strong enough to stabilize skyrmions (Ding *et al.*, 2019; Shao *et al.*, 2019) and for fast domain motion (Avci *et al.*, 2019). Ferrimagnetic insulators are attractive due to their lower Gilbert damping in comparison with ultrathin ferromagnetic metals. Using SOT, Ding *et al.* (2019) quantified the DMI in thulium iron garnet TmIG/Pt bilayers and showed that the magnitude of the DMI constant is about 1 to 2 orders smaller than in metallic heterostructures. They also showed that the magnitude of the DMI constant is inversely proportional to the TmIG thickness, indicating that the DMI in

TABLE XIX. Overview of DMI measurements of various FM materials by a spin-orbit-torque-induced effective field under an in-plane bias magnetic field. FM and NM stand for ferromagnetic and nonmagnetic layers, respectively. D is the interfacial DMI constant and $D_s = Dd$, where d is the thickness of the FM. Numbers in roman were quoted in the reviewed papers, while numbers in italics were either extracted from figures or calculated using the parameters provided.

FM (nm)	Bottom NM (nm)	Top NM (nm)	$\lvert\mu_0 H_{\rm DMI}\rvert$ (mT)	$\lvert D\rvert$ (mJ/m^2)	$\lvert D_s\rvert$ (pJ/m)	Reference
Co(1)	Pt(4)	MgO(2)	500	3.0	*3.0*	Pai *et al.* (2016)
CoFeB(1)	Pt(4)		250	1.8	*1.8*	
CoFeB(1)	Ta(6)		25	0.6	*0.6*	
Co(0.65)	Pt(4)		110	1.45	*0.94*[a]	
Co(0.80)	Pt(4)		200	1.99	*1.59*[a]	
Co(0.92)	Pt(4)		290	2.12	*1.95*[a]	
Co(1.00)	Pt(4)		400	2.64	*2.64*[a]	
Co(1.10)	Pt(4)		450	2.91	*3.20*[a]	
Co(1.23)	Pt(4)		310	2.49	*3.06*[a]	
Co(1.43)	Pt(4)		160	1.62	*2.32*[a]	
Co(1.52)	Pt(4)		100	1.37	*2.08*[a]	
Co(0.5)	Pt(4)	Ta(2)	110 ± 10	1.01 ± 0.12	*0.51 ± 0.06*	Yun *et al.* (2018)
		Ta(4)	110 ± 10	0.75 ± 0.09	*0.38 ± 0.05*	
		Ta(6)	80 ± 10	0.70 ± 0.09	*0.35 ± 0.05*	
		Ta(8)	190 ± 10	1.4 ± 0.12	*0.7 ± 0.06*	
Co(1.2)	Pt(4)	Ir(1)	65 ± 6	1.09 ± 0.14	*1.31 ± 0.17*	Khadka, Karayev, and Huang (2018)
Co(1.2)	Pt(4)	Ir(2)	81 ± 8	1.42 ± 0.18	*1.7 ± 0.22*	
Co(1)	Pt(4)	Ir(1)	130 ± 13	2.06 ± 0.26	*2.06 ± 0.26*	
Co(1)	Pt(4)	Ru(2)	140.4 ± 14	2.66 ± 0.33	*2.66 ± 0.33*	
Co(0.8)	Pt(4)	Ru(2)	212 ± 21	2.40 ± 0.3	*1.92 ± 0.24*	
Co(0.8)	Pt(4)	Ru(3)	218 ± 22	2.30 ± 0.29	*1.84 ± 0.23*	
Co(0.8)	Pt(4)	Ru(4)	238.6 ± 24	2.56 ± 0.32	*2.05 ± 0.26*	
[Pt(1)/Co(0.8)/Ru(1.3)]$_2$	Pt(3)		220 ± 22	2.07 ± 0.26	*1.66 ± 0.21*	
CoFeB(1.0)	Ta(5)/Pt(0)	MgO(1)	45	0.21	*0.21*	Chen, Zhang *et al.* (2018)
	Ta(5)/Pt(0.3)			0.15	*0.15*	
	Ta(5)/Pt(0.7)			0.08	*0.08*	
	Ta(5)/Pt(1.0)			0.05	*0.05*	
CoFeB(1.4)	Mo(4)	MgO(2)	20	0.35	*0.49*	Chen, Chan *et al.* (2018)
FeB(0.96)	α-W(4)	MgO(1.6)	25			Dohi *et al.* (2019)
FeB(0.86)			30			
FeB(0.76)			18			
FeB(0.56)			50			
[Pt(0.6)/Co(0.9)/Ir(0.6)]$_3$	Pt(2)	MgO(2)	80	0.4	*0.36*	Ishikuro *et al.* (2019)
[Pt(0.6)/Co(0.9)/Cu(0.6)]$_3$	Pt(2)	MgO(2)	180	1.8	*1.62*	
[Pt(0.6)/Co(0.9)/Ir(0.6)]$_1$	Pt(2)	MgO(2)	110	0.7	*0.63*	
Co(0.9)	Ir(7)	MgO(2)	220	1.6	*1.44*	
Co(0.9)	Pt(2)/Ir(1)	Ru(1)	150	1.1	*0.99*	
TmIG[b](2.9)	Pt(7)		20 ± 1	0.036 ± 0.02	*0.1 ± 0.06*	Ding *et al.* (2019)
TmIG[b] (2.9–16)	GGG[c] substrate	Pt(7)	*22–1.5*	*0.035–0.003*	*0.13*[d]	Ding *et al.* (2020)
TmIG[b] (5.4)		Pt(0.5 − 7)		*0.024–0.029*	*0.13*[e]	
		W(5)/Cu(3)		*0.025*	*0.135*	
		Cu(3)/Pt(1.5)		*0.025*	*0.135*	
Co(0.8)	Cr$_{0.25}$Pt$_{0.75}$(8)/Pt(0.4)	AlO$_x$(2)	100	0.87	*0.70*	Quan *et al.* (2020)
[Ni(0.34)/Co(0.16)]$_2$	Cu(2.5)	Ir(4)	17.4	0.82	*0.82*	Yang *et al.* (2021)

[a] Note that the $1/t$ dependence is not observed.
[b] Thulium iron garnet.
[c] Gd$_3$Ga$_5$O$_{12}$.
[d] The value was obtained from a linear fit over all TmIG thicknesses.
[e] The value was obtained from averaging over all Pt thicknesses.

a TmIG/Pt bilayer is indeed an interfacial effect. Ding, Baldrati *et al.* (2020) attributed the origin of the DMI in TmIG/HM bilayers on Gd garnet (GGG) substrates could be attributed to the GGG/TmIG interface by investigating the FM and HM thickness-dependent DMI and SOT.

D. Advantages and limitations

Unlike the methods based on DW motion and asymmetric spin-wave propagation, the method based on current-induced shifts of the anomalous Hall loops is a straightforward way

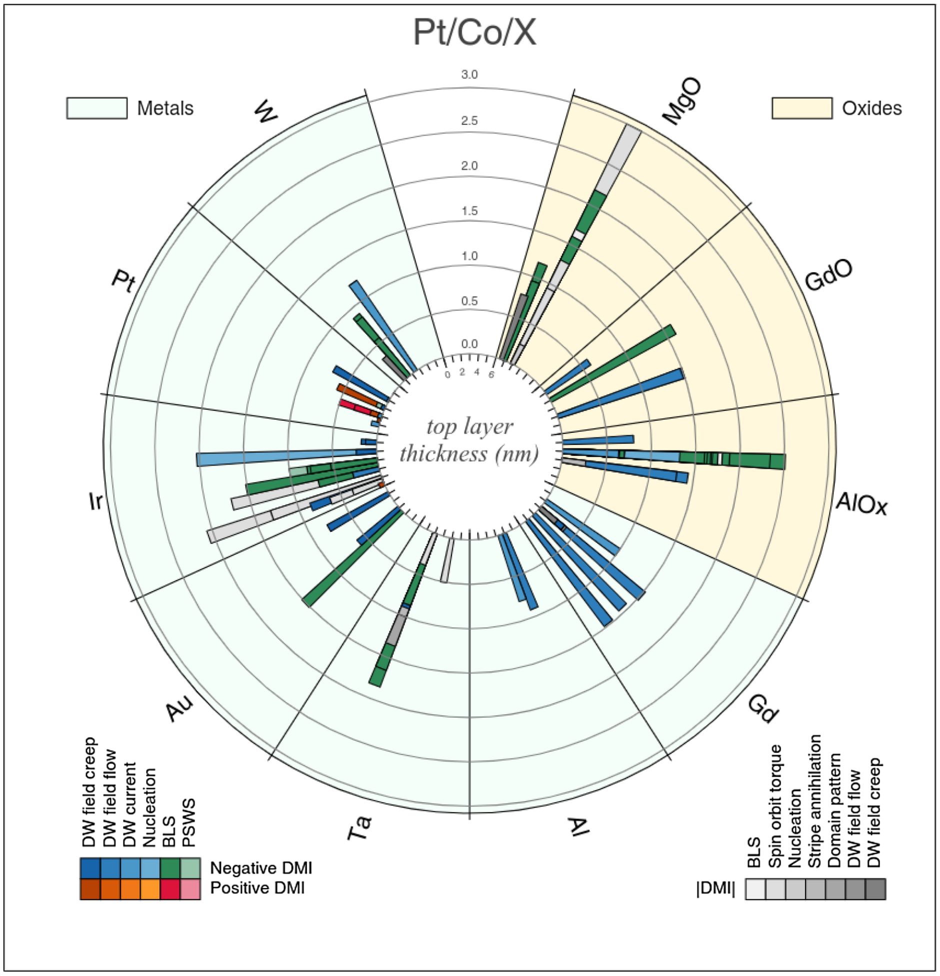

FIG. 28. Literature data of the DMI constant D_s for the Pt/Co/X thin films, where the top layers $X = (\mathrm{MgO}, \mathrm{GdO}, \mathrm{AlO}_x$, $\mathrm{Al}, \mathrm{Ta}, \mathrm{Au}, \mathrm{Ir}, \mathrm{Pt}, \mathrm{W})$ can be metals (light green) or oxides (light yellow). The blue-green and orange-red palettes are for experimental methods where the signs are known (negative and positive, respectively), while the gray palette is for data where only the magnitude of D_s is available. The thickness of the bottom layer of Pt varies between 0.8 and 30 nm, with about 70% of the data between 3 and 5 nm. The top layer thickness (in nm) is shown as internal ticks (up to 6 nm). The large circles are the scale of D_s (up to 3 pJ/m).

for determining the DMI field without involving complicated mathematical models. However, this method requires perpendicular magnetic anisotropy of the ferromagnetic material. Nonsquare shapes of the AHE loops also lead to inaccuracies in the determination of H_{DMI}. To determine the DMI constant, one requires a numerical value for the exchange stiffness; an assumed value is usually used. Moreover, this method is not capable of determining the sign of the DMI.

V. COMPARISON OF THE METHODS AND DISCUSSION OF PROBLEMS IN THE DETERMINATION OF THE DMI CONSTANT

A. Comparing the DMI constants obtained by the different methods

When comparing the DMI constant D measured by different methods, it becomes clear that the values sometimes do not coincide within the measurement uncertainty, or are even vastly different (as shown in Figs. 28 and 29[16]), even if the measured stacks are nominally the same. Taking as examples the data shown in Fig. 28, there is disagreement on the D_s values that are found for the Pt/Co/Ir stacks (absolute range 0.20–2.0 measured by nucleation, DW creep, and BLS), Pt/Co/Ta stacks (absolute range 0.38–1.84 measured by BLS, domain pattern, stripe annihilation, and SOT) or Pt/Co/AlO_x (absolute range 0.50–2.50 measured by the DW current, BLS, SOT, and nucleation), and Pt/Co/MgO (absolute range 0.2–3 measured by BLS and DW flow). Therefore, it is important to consider not only the advantages and limitations of each individual method, which influence their applicability, but also their intrinsic differences, which might influence the measurement result.

---

[16] The electronic versions of Figs. 28 and 29 are available at https://github.com/gdurin/DMI_plots from the GitHub repository, enabling one to get the full description of each data point (stack composition, DMI value, reference) by manipulating the mouse over the bars.

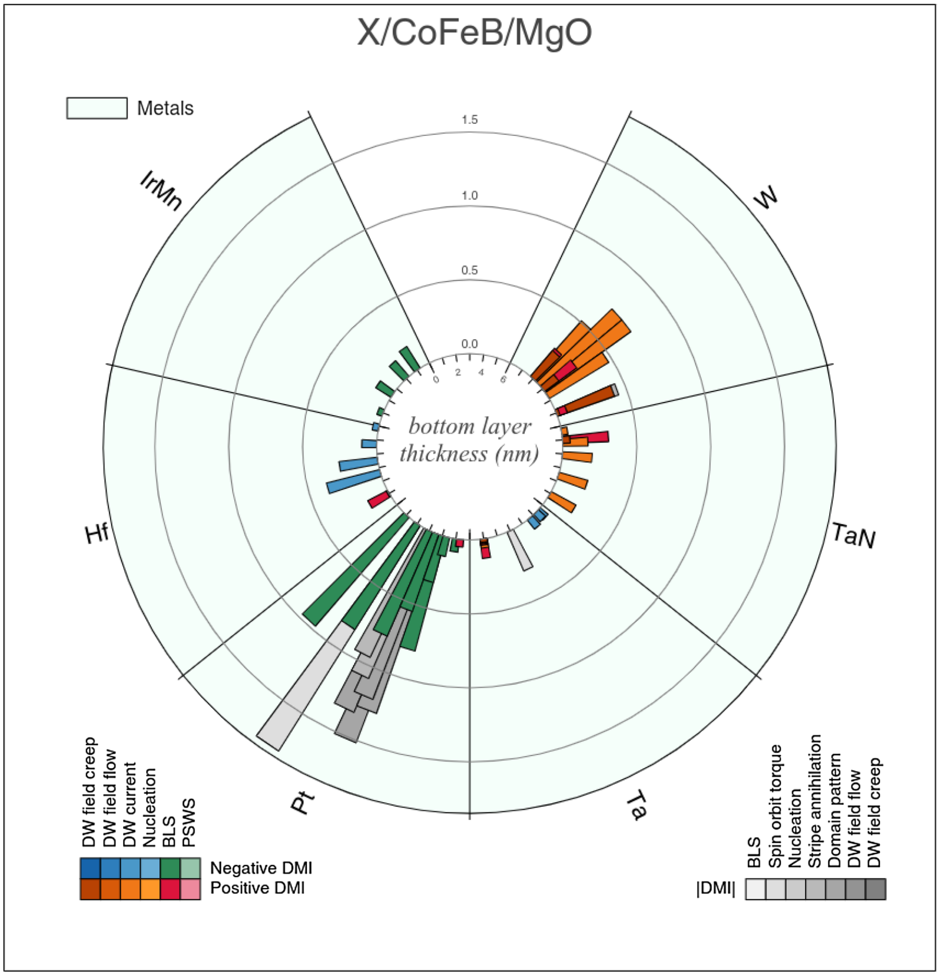

FIG. 29. Literature data of the DMI constant D_s for the X/CoFeB/MgO thin films, where the bottom layers $X = (\mathrm{IrMn, Hf, Pt, Ta, TaN, W})$ are the most popular metals in the literature. The blue-green and orange-red palettes are for experimental methods where the signs are known (negative and positive, respectively), while the gray palette is for data where only the magnitude of D_s is available. Most of the data ($>70\%$) are for a MgO thickness of 2 nm, with nearly 20% for 1 nm. The bottom layer thickness (in nm) is shown as internal ticks (up to 6 nm). The large circles are the scale of D_s (up to 1.5 pJ/m).

In this respect, one should keep in mind that the results are strongly influenced by the material properties and layer combinations, as well as by the specific layer thickness and substrate chosen (Soucaille *et al.*, 2016; Shahbazi *et al.*, 2019). In fact, since in the thin film systems DMI is an interface effect, details concerning the structural and chemical quality of the materials, particularly of the interfaces, play a crucial role and should be stated in the publications as much as possible. Furthermore, to judge the relative accuracy and reliability of different methods it would be desirable to compare measurements performed on identical samples, and a more intense research effort should respond to this need. However, systematic studies comparing the various methods are rare and the disagreement between results obtained by different techniques is not often discussed (Magni *et al.*, 2022).

In general, methods based on domain walls are affected by the fact that pinning influences the DW properties. For instance, quasistatic methods based on imaging usually rely on observing the DW or a number of domains in a certain position, which are therefore close to those pinning sites. They depend on the local energy landscape at a pinning site, which may differ from that far from the pinning site, and the result of the measurement may vary even from spot to spot in a single sample due to the distribution of inhomogeneities and defects. Analytical models and simulations usually do not take these imperfections into account and use average parameters, which may lead to intrinsic errors. In addition, strain in the thin films might play a role, as shown by several recent works investigating defect- or strain-induced DMIs (Fernández-Pacheco *et al.*, 2019; Michels *et al.*, 2019; Deger, 2020). Therefore, a statistical assessment across a sample, measured at many different locations, could help one to understand more about defect-related differences in the measurements but is currently lacking in the literature.

In methods based on DW motion in the creep regime, DWs move due to thermal activation from one pinning site to the next. These measurements show good agreement for small DMI values with static methods, such as the stray field measurements by NV center magnetometry and BLS (Gross *et al.*, 2016; Soucaille *et al.*, 2016; Cao, Zhang *et al.*, 2018; Belmeguenai *et al.*, 2019). As detailed in Sec. II.B, measurements in the creep regime require simplified models of the domain-wall dynamics, which evaluate the domain velocity profile and extract the DMI field. In this respect, one problem is connected with the fact that the DW speed minimum may not correspond to H_{DMI}. Moreover, the evaluation of the DMI constant depends on the DW width or the DW energy, parameters known only up to a certain accuracy. They are often calculated from the exchange stiffness that should be determined experimentally, which requires a substantial additional effort.

SW methods have the advantage of a more straightforward evaluation of the DMI constant by measuring a frequency shift, which is possible with high accuracy, in an in-plane saturated sample. Concerning the model used to analyze the experimental data, only the gyromagnetic ratio γ and the saturation magnetization M_s have to be known [the exchange constant has a negligible influence on the frequency of long wavelength SWs, as seen in Eq. (3.11)], parameters that are more easily accessible experimentally. The most widely employed, direct, and effective method is BLS, as it does not require any external spin-wave transduction or any kind of patterning, contrary to TRMOKE and PSWS. Pinning sites usually do not influence the dispersion relation of SWs directly, but instead affect only the measured SW decay length that is reflected in the linewidth in domain methods. Moreover, SW methods are rather insensitive to the presence of defects, grain boundaries, inclusions, and surface roughness. In this respect, one has to consider that the revealed SWs have wavelengths ranging from half a micron to a few microns and that measurements average over a large sample area. In the cases of BLS and TRMOKE the typical spot size is on the order of $1-10\ \mu$m, and in the case of PSWS a typical CPW is also about 10 μm long, while DWs have a width on the order of 10 nm. Moreover, the propagation distance of SWs, even for thermal SWs detected by BLS, is of the order of several microns, and the influence of nanometric inhomogeneities is averaged out (for instance, they may result in a broadening of the BLS peaks, with a minor influence on the mean frequency). Another simplification of SW methods might be that the measurement does not generally require measuring (and evaluating by a model) the spin-wave dispersion $\omega(k)$ itself, but instead only the difference $\omega(k)-\omega(-k)$, and is therefore a kind of differential method. Concerning methods that determine the DMI field under the influence of a current (such as current-induced DW motion and SOT field measurements), the main difficulty is the interpretation of the results, taking into account the different contributions of spin-orbit torques. Dampinglike and fieldlike torques may have different origins as the SHE and the ISGE, and both contribute to the observed dynamics. Furthermore, in metallic stacks the current flow in the plane is not well defined, as it is partly in the FM and partly in the HM material, depending on the relative resistances and the interface scattering and transparency (Stejskal *et al.*, 2020).

The differences in applicability of the various methods explain why a direct comparison on the same sample is rarely reported in the literature. Only a few papers (Vaňatka *et al.*, 2015; Pham *et al.*, 2016; Soucaille *et al.*, 2016; Lau *et al.*, 2018; D.-Y. Kim *et al.*, 2019; Shahbazi *et al.*, 2019) reported a quantitative comparison of the values of D, measured by both BLS- and DW-based methods. In general, reasonable agreement is attained for the different systems if BLS results are compared to those extracted from an analysis of DW motion in the flow regime. Instead, when DW motion is measured in the creep regime, the values obtained by DW-based methods are generally significantly higher or lower than those obtained by BLS.

An attempt to classify the applicability of three methods (BLS, SOT efficiency, and DW velocity) according to DMI strength and FM layer thickness was performed by D.-Y. Kim *et al.* (2019). According to their scheme, BLS is best applied to larger D values and FM film thicknesses. Meanwhile, DW methods are suitable for smaller values, while SOT applies to small values of D, but higher FM layer thicknesses. In an intermediate range all three methods are applicable, and a direct comparison of the methods on the same sample is possible. In fact, for the samples $\mathrm{Pt}(2.5\ \mathrm{nm})/\mathrm{Co}(0.9\ \mathrm{nm})/X(2.5\ \mathrm{nm})$ ($X=\mathrm{Ti},\mathrm{Ta},\mathrm{Al},\mathrm{Pt}$) they found an excellent agreement within a 5% difference. In contrast, in the case of Pt/Co/W, a 10% difference between DW-based and SW-based methods occurs, and Pt/Co/Cu presents a much larger 40% difference. D.-Y. Kim *et al.* (2019) argued that the limitation of BLS for measuring low DMI values is the interferometer resolution, while measurements of FM films thinner than about 1 nm are limited by the high in-plane magnetic field necessary to overcome the PMA.

DW velocity and SOT methods are limited in measuring high DMI values by the maximum in-plane field that can be applied. D.-Y. Kim *et al.* (2018) claimed that the DW velocity is limited by chiral damping in smaller film thicknesses with respect to the SOT method.

The previously mentioned considerations are corroborated by a synoptic view of the tables of results and Figs. 28 and 29 that is discussed later: one may find that, in several examples of nominally similar systems, different groups obtained markedly different results. In this context, even if BLS seems at the moment the most popular and efficient method to determine DMI in layered systems, more systematic multitechnique investigations of the DMI on the same samples for different material combinations and layer thicknesses (including a cross-check concerning the mutual consistency of results relative to different regions on the same sample) would be highly desirable.

B. Comparing the DMI constants in different materials

The two most common material combinations investigated in the literature are heterostructures consisting of (a) HM/CoFeB/MgO multilayers and (b) Co films in contact with a Pt top or bottom layer. In Fig. 28 we focus on $\mathrm{Pt}/\mathrm{Co}/X$ heterostructures, with the top layer $X=$ W, Pt, Ir, Au, Ta, Al, Gd, AlO_x, GdO, and MgO. When the sign of D_s is not available a gray scale is used; otherwise, a positive sign is indicated by an orange-red palette and a negative sign is indicated by a blue-green one. The sign is mostly negative because it is dominated by the Pt/Co interface, which gives a negative sign (according to the conventions used in this paper). The largest negative DMI is found with oxides on top, AlO_x, GdO, and MgO (Boulle *et al.*, 2016), with the record of $|D_s| = 3\,\mathrm{pJ/m}$ in Pt(4 nm)/Co(1 nm)/MgO(2 nm) thin films measured using the spin-orbit torque method (Pai *et al.*, 2016). Chaves *et al.* (2019) showed by investigating oxide wedge samples that the effective DMI strength in the Pt/Co/MO$_x$ trilayers ($M = \mathrm{Al, Gd}$) varies with the oxidation degree of the Co/MO$_x$ interface. This strongly suggests that the Co/MO$_x$ interface gives a distinct contribution to the total DMI, adding to that of the Pt/Co interface. The other elements as top layers show a spread of results, as for Ta, Pt, and Ir. The Pt/Co/Ir/X stacks show a large variety in magnitude and sign, for instance. Note that the introduction of an Ir thin layer in Pt/Co/Ir/Pt reduces the magnitude of D_s and changes the sign for thicker Ir (Hrabec *et al.*, 2014). In Ir/Co/MgO a negative value for D_s was found with BLS, suggesting that a Ir bottom (top) layer gives rise to a negative (positive) DMI, so it would be possible to increase the DMI by fabricating Pt/Co/Ir trilayers, as found in several studies (Fig. 28). Another interesting system is Pt/Co/W. Here, even though W contributes with opposite sign to the DMI with respect to Pt and its contribution to the DMI strength in general is higher than that for FM/oxide interfaces, the total DMI of Pt/Co/W stacks is found to be smaller than that of Pt/Co/oxide stacks.

In the Pt/Co/Pt stack, with two Pt films of the same thickness a perfect or nearly perfect compensation for the top and bottom contributions has been found in a few cases (Pham *et al.*, 2016; D.-Y. Kim *et al.*, 2018, 2019; Agrawal *et al.*, 2019; Belmeguenai *et al.*, 2019; Géhanne *et al.*, 2020) (not shown in Fig. 28), and more generally small values of DMI are found, both positive and negative, as shown in Fig. 28. Additionally, current-induced motion experiments in Pt/Co/Pt samples show negative values regardless of the thickness of the top or bottom layer (Franken *et al.*, 2014), while creep regime experiments give mostly positive values. In summary, Fig. 28 emphasizes the strong influence of film preparation, differences in interface properties between the top and bottom layers, etc., on the DMI, which explains the high variability in the magnitude and sign of D_s.

A summary of experimental data for the X/CoFeB/MgO heterostructures ($X = $ IrMn, Hf, Pt, Ta, TaN, W) is shown in Fig. 29.[17] As in Fig. 28, methods in which the sign is not able to be determined are shown with a gray palette, while positive signs are indicated with an orange-red palette and negative signs are reflected with a blue-green color scheme. In general, the different methods give values comparable in magnitude, with the exception of Pt/CoFeB/MgO, where BLS and domain pattern–spin-torque methods diverge. The CoFeB/MgO bilayer sputtered directly on the substrate has a small positive $D_s = 0.13$ pJ/m (Chen, Zhang *et al.*, 2018). This value is compensated in the case of Pt and IrMn bottom layers showing a negative D_s for the largest thickness (up the maximum value of about -1.75 pJ/m for the Pt layer, measured using spin-torque methods). Conversely, W and TaN increase the positive value of D_s, up to about 0.7 pJ/m for the W layer. Less clear is the contribution of Hf and Ta. Hf leads to a negative D obtained by current-induced domain-wall motion measurements for a film thickness larger than 2 nm, while a positive D_s is obtained in the creep regime and using BLS for a 1-nm-thick layer. Note that the negative value is decreasing as the Hf becomes thicker, while for Pt or IrMn D_s increases for thicker films. Ta gives a variation of D_s from negative to positive when the thickness is increased, as measured by current-induced domain-wall motion (Torrejon *et al.*, 2014), which is in contrast with the positive value for the stack without a bottom layer. Furthermore, Karnad *et al.* (2018) reported different signs when measuring by creep regime and by current-induced domain-wall motion, which is not surprising given the relatively small value of D_s in those Ta samples.

Despite all these difficulties, a few conclusions can be reached concerning the strength and sign of the DMI. The highest absolute values of D_s are obtained for Pt/FM interfaces in combination with oxide top layers. If the order of the stack is reversed, then one finds a reversal of the sign by symmetry. The strength of the DMI may be different due to the different growth conditions of a reversed stack, but the sign reversal is effectively verified as in Pt/Co/Ta and Ta/Co/Pt trilayers measured using BLS (Cho *et al.*, 2017). When the sign convention used in this review is employed, BLS experiments are consistent with a negative (positive) value of D_s for a Pt bottom (top) layer regardless of the FM composition, as verified for CoFeB, Co, Co/Ni, and Ni$_{80}$Fe$_{20}$, and independent of whether the top layer is an oxide or another heavy metal. This result is also consistent with the sign detected for current-induced domain-wall motion and field-driven motion in the flow regime. Moreover, a positive sign is found for TaN and W bottom layers in contact with a Co film. Instead, for small DMI values (as for the Pt/Co/Pt samples in Fig. 28) a clear sign trend is not observed, and for nominally equally thick bottom and top Pt layers the DMI is in general not compensated. In X/CoFeB/MgO systems (Fig. 29) an increase (decrease) of DMI strength with the Pt (Hf) thickness is found. On the contrary, a nonmonotonic dependence is observed for W with a maximum value for an intermediate thickness.

C. Influence of growth conditions on the DMI constant

Owing to the large spread of materials used, the investigation of the influence of growth condition on DMI has not yet been conclusive. Wells *et al.* (2017) studied the effect of sputter-deposition conditions on DMIs in Pt/Co/Pt structures. They found that the growth temperature modifies the interfacial roughness. The differing qualities of the top Pt/Co interface and the lower Co/Pt one introduces a structural inversion asymmetry, which results in a net DMI field in this nominally symmetric structure. This explains the discrepancies of the sign of D for Pt/Co/Pt stacks, as mentioned in Sec. II.C.2.

Regarding the effect of postannealing, Khan *et al.* (2016) studied the influence of annealing on DMI in Ta/CoFeB/MgO. Here the DMI field H_{DMI} is determined by magnetic-field-driven domain motion in the creep regime. They found that both H_{DMI} and the DMI constant D vary with annealing temperature, reaching a peak at 230 °C and then decreasing as the temperature is further increased. They also found that the

---

[17] Note that the figure contains both compositions of CoFeB, mostly Co$_{20}$Fe$_{60}$B$_{20}$ (70% of the data) and Co$_{40}$Fe$_{40}$B$_{20}$ (15%), with the remaining data (15%) unspecified.

dependence of the interfacial perpendicular magnetic anisotropy field H_{ani} on annealing temperature follows a similar trend as DMI, suggesting a connection between these parameters. They suggested that the increase of H_{DMI} and H_{ani} is due to an improved ordering of atoms at the Ta/CoFeB interface. A higher annealing temperature leads to diffusion of B atoms out of CoFeB as well as intermixing at the interface, which significantly reduces H_{DMI} and H_{ani}. Cao, Chen *et al.* (2020) reported a similar trend involving the annealing temperature dependence of H_{DMI} in Pt/Co/X/MgO structures ($X = \mathrm{Mg}$ or Ta) investigated by magnetic-field-driven domain motion. A maximum H_{DMI} is obtained at an annealing temperature of 300 °C, which is independent of the MgO thickness. Like Khan *et al.* (2016), they proposed that the enhanced H_{DMI} is due to the improved crystalline quality upon annealing. However, Furuta *et al.* (2017) used current-driven domain-wall motion to study the effect of annealing on H_{DMI} in Pt/[Co/Ni] structures. They showed that annealing causes a significant reduction of H_{DMI}, domain-wall velocity, perpendicular magnetic anisotropy, and spin-orbit torques, which is attributed to the diffusion of Co atoms across the Pt/Co interface.

D. Outlook and conclusion

In this review more than 100 articles measuring interfacial DMI have been analyzed. Interest in this topic is still growing, as illustrated by the rapidly increasing number of publications and citations. It may be surprising that only in recent years has the topic of chiral magnetism gained such relevance in the research community, as parity breaking and chirality is intrinsic to magnetic systems.

New opportunities have recently been foreseen, shifting the focus away from traditional HM/FM bilayers to synthetic antiferromagnets (SAFs) and oxides. SAFs exploit the Ruderman-Kittel-Kasuya-Yosida exchange interaction between two ultrathin FM layers separated by a nonmagnetic spacer layer, which can be tuned using the spacer layer thickness (Duine *et al.*, 2018). In these systems, with a HM as the spacer layer, it was shown that the DMI is enhanced by the dipolar field between the FM layers (Fernández-Pacheco *et al.*, 2019; Meijer, Lucassen, Kloodt-Twesten *et al.*, 2020). Besides having the advantages of antiferromagnets, such as negligible stray fields and stability against magnetic fields (Baltz *et al.*, 2018), these SAFs exhibit asymmetric DWs and spin-wave dynamics. The possibility of tailoring DMIs in SAFs makes them extremely interesting for applications of chiral magnetism and topological spin structures (Legrand *et al.*, 2020; Vedmedenko *et al.*, 2020). Since this topic goes beyond the scope of this review, it is not included in the tables; however, the increasing interest in SAFs is notable (Fernández-Pacheco *et al.*, 2019; Han *et al.*, 2019; Bollero *et al.*, 2020; Meijer, Lucassen, Kloodt-Twesten *et al.*, 2020; Tanaka *et al.*, 2020; Tsurkan and Zakeri, 2020).

A second topic that has come up recently, and that brings us to the microscopic origin of DMI, is DMIs in FM oxides (Wang *et al.*, 2020) and oxidized metallic FM (Nembach *et al.*, 2020), which is not yet fully understood but might be related to local charge transfer at the interfaces. With a comparison of systems comprising Pt/$\mathrm{Co_{90}Fe_{10}}$/oxide and Cu/$\mathrm{Co_{90}Fe_{10}}$/oxide, Nembach *et al.* (2020) showed how oxidation of the metallic FM interface can enhance the DMI, which increases with oxidation time and eventually reaches saturation. For the Pt/$\mathrm{Co_{90}Fe_{10}}$ system this increase is due to the fact that the DMIs on both interfaces promote left-handed chirality, and the enhanced DMI is suggested to be caused by an electric dipole moment induced by hybridization and charge transfer at the oxygen/FM metal interface (Belabbes *et al.*, 2016). This ISGE-induced DMI (Kim *et al.*, 2013) was also observed for a Co/graphene interface (Yang *et al.*, 2018). In both cases DFT calculations were fundamental to interpreting the results, and the calculations showed that the DMI originates from the FM layer, not the HM layer (Yang *et al.*, 2018; Yang, Boulle *et al.*, 2018). However, the fact that hybridization at the interface plays an essential role makes the analysis complex and categorizing materials or stacks according to their DMI strength becomes almost impossible. Interface intermixing, interface roughness, dead layers, and proximity effects have all been known to affect the DMI. In fact, a detailed interface characterization should be performed in order to obtain a complete picture. Although certain materials give higher DMIs than others, the interfacial DMI may depend on the interface properties more than the material properties themselves. For example, annealing may change the DMI value by about 20%–30% (Benguettat-El Mokhtari *et al.*, 2020), while the exchange of top and bottom layers by Cho *et al.* (2017) led to changes of about 30%. The ISGE-induced DMI is closely related to materials for spin-to-charge conversion that have recently attracted attention (Chen *et al.*, 2016; Rojas-Sánchez and Fert, 2019; Ding *et al.*, 2020). A key feature is again that the mechanism of SOC (but not necessarily a material with strong SOC such as HM) is required, but SOC can also be induced at the interface by the ISGE. As with other SOC-related phenomena (such as spin-orbit torques), the origin of the DMI, from either bulk SOC or SOC at the interface, is impossible to disentangle and has to be treated in a common theoretical approach. The DMI was first described using a phenomenological thermodynamic theory, but it now appears to be fundamental, for developing materials designed for future applications, that the microscopic origin of the DMI has to be understood in more detail.

A third new emerging topic investigates the possibility to stabilize chiral spin textures in centrosymmetric magnetic insulators, where high DW speeds (up to 400 $\mathrm{ms^{-1}}$) are reached with minimal currents of 10^6 $\mathrm{A/cm^2}$ (Vélez *et al.*, 2019). In systems like TmIG a small DMI on the order of a few μJ/m has been detected in DW racetracks and confirmed by scanning nitrogen-vacancy magnetometry. In particular, TmIG thin films grown on $\mathrm{Gd_3Sc_2Ga_3O_{12}}$ exhibit left-handed Néel chirality, changing to an intermediate Néel-Bloch configuration upon Pt deposition. Similarly, Lee *et al.* (2020) showed that Pt, W, and Au induce strong interfacial DMIs and the topological Hall effect, while Ta and Ti cannot, thus providing insight into the mechanism of electrical detection of spin textures in these magnetic insulator heterostructures.

A fourth and important research field is that related to the search for systems with large and tailored DMIs, paving the way to the stabilization and exploitation of topological spin structures such as spirals, helices, merons, skyrmions, and antiskyrmions at temperatures well above room temperature and supporting high-frequency dynamics (Finocchio *et al.*, 2016). It would represent a clear advantage to move toward applications, where nonequilibrium operation is needed to achieve fast switching and information processing. In this respect, the stabilization of topological magnetic objects and the control of their dynamical properties can be made more efficient and reliable by patterning periodic arrays of two-dimensional dots or antidots. These systems are also the battleground of the rising and intriguing field of magnonics, where information is carried and manipulated by spin waves propagating in periodically modulated media, i.e., artificial magnonic crystals. The integration of DMIs into magnonic crystals is expected to create unexplored possibilities due to the appearance of a sizable asymmetry in the magnonic band structure, enabling the possibility of unidirectional energy transfer and magnetic damping tuning (Gallardo, Cortés-Ortuño, Schneider *et al.*, 2019). In this context, the concept of topologically protected chiral edge spin waves existing in the band gap of a topological magnetic material and propagating in a certain direction with respect to the bulk magnetization direction appears to be promising (Wang, Zhang, and Wang, 2018). Based on this idea, reconfigurable topological spin-wave diodes, beam splitters, and interferometers can in principle be designed and realized for new information and communication technology devices.

Finally, although this review was focused on experimental methods and results, new challenges and advances in this research field, and also in terms of the functionality and engineering of materials, are connected with the achievement of a better understanding of the microscopic origin of DMIs, relying on quantum mechanical and atomistic calculations (Yang *et al.*, 2015) and integrating them into a multiscale modeling chain whose uppermost level is the micromagnetic simulations able to mimic the behavior of real devices. One necessary step for this goal will be to shorten the gap existing between research communities that use classical physics and those that use quantum physics so as to set up efficient computer codes, operating in a multiscale framework, capable of providing quantitative predictions and recipes for the next generation of materials and devices. In terms of experiments, characterizing the atomic scale details of real interfaces is a great but important challenge that must be met in order to tease out the ultimate causes of the variations in DMIs observed in the disparate reports to date.

ACKNOWLEDGMENTS

We thank G. Chen, A. Schmid, and T. P. Ma for the unit conversion of the *D* values in Table XIII. M. K. thanks H. T. Nembach, J. M. Shaw, and A. Magni for the fruitful discussions. We also thank P. Landeros for a critical reading of the manuscript and useful suggestions. Project No. 17FUN08-TOPS has received funding from the EMPIR program cofinanced by the participating states and by the European Union's Horizon 2020 research and innovation program. F. G.-S. acknowledges support from Project No. PID2020117024GB-C41, which was funded by the Ministerio de Ciencia e Innovación of the Spanish Government. L. C. and C. H. B. acknowledge support from the DFG through SFB 1277. C. H. M. acknowledges support from the EPSRC (Grant No. EP/T006803/1). G. D. acknowledges support from the European Union H2020 Program (MSCA ITN 860060).

REFERENCES

Agrawal, Parnika, Felix Büttner, Ivan Lemesh, Sarah Schlotter, and Geoffrey S. D. Beach, 2019, "Measurement of interfacial Dzyaloshinskii-Moriya interaction from static domain imaging," Phys. Rev. B **100**, 104430.

Ahmadi, Khadijeh, Loghman Jamilpanah, Seyed Ali Seyed Ebrahimi, Abbas Olyaee, Mohammad Mehdi Tehranchi, and Seyed Majid Mohseni, 2020, "Observation of the Dzyaloshinskii-Moriya interaction via asymmetry in magnetization reversal," J. Phys. D **53**, 465001.

Ajejas, Fernando, Viola Křižáková, Dayane de Souza Chaves, Jan Vogel, Paolo Perna, Ruben Guerrero, Adrian Gudin, Julio Camarero, and Stefania Pizzini, 2017, "Tuning domain wall velocity with Dzyaloshinskii-Moriya interaction," Appl. Phys. Lett. **111**, 202402.

Albornoz, L. J., E. E. Ferrero, A. B. Kolton, V. Jeudy, S. Bustingorry, and J. Curiale, 2021, "Universal critical exponents of the magnetic domain wall depinning transition," Phys. Rev. B **104**, L060404.

Arias, Rodrigo, and D. L. Mills, 1999, "Extrinsic contributions to the ferromagnetic resonance response of ultrathin films," Phys. Rev. B **60**, 7395–7409.

Arora, Monika, Justin M. Shaw, and Hans T. Nembach, 2020, "Variation of sign and magnitude of the Dzyaloshinskii-Moriya interaction of a ferromagnet with an oxide interface," Phys. Rev. B **101**, 054421.

Avci, Can Onur, Ethan Rosenberg, Lucas Caretta, Felix Büttner, Maxwell Mann, Colin Marcus, David Bono, Caroline A. Ross, and Geoffrey S. D. Beach, 2019, "Interface-driven chiral magnetism and current-driven domain walls in insulating magnetic garnets," Nat. Nanotechnol. **14**, 561–566.

Baćani, Mirko, Miguel A. Marioni, Johannes Schwenk, and Hans J. Hug, 2019, "How to measure the local Dzyaloshinskii-Moriya interaction in skyrmion thin-film multilayers," Sci. Rep. **9**, 3114.

Bailleul, M., D. Olligs, and C. Fermon, 2003, "Propagating spin wave spectroscopy in a Permalloy film: A quantitative analysis," Appl. Phys. Lett. **83**, 972.

Bailleul, M., D. Olligs, C. Fermon, and S. O. Demokritov, 2001, "Spin waves propagation and confinement in conducting films at the micrometer scale," Europhys. Lett. **56**, 741–747.

Bak, P., and M. H. Jensen, 1980, "Theory of helical magnetic structures and phase transitions in MnSi and FeGe," J. Phys. C **13**, L881.

Balk, A. L., K.-W. Kim, D. T. Pierce, M. D. Stiles, J. Unguris, and S. M. Stavis, 2017, "Simultaneous Control of the Dzyaloshinskii-Moriya Interaction and Magnetic Anisotropy in Nanomagnetic Trilayers," Phys. Rev. Lett. **119**, 077205.

Baltz, V., A. Manchon, M. Tsoi, T. Moriyama, T. Ono, and Y. Tserkovnyak, 2018, "Antiferromagnetic spintronics," Rev. Mod. Phys. **90**, 015005.

Bauer, H. G., J.-Y. Chauleau, G. Woltersdorf, and C. H. Back, 2015, "*k*-vector distribution of magneto-static spin waves excited by micro-fabricated antenna structures," in *Ultrafast Magnetism I*, Springer Proceedings in Physics Vol. 159, edited by J. Y. Bigot,

W. Hübner, T. Rasing, and R. Chantrell (Springer, Cham, Switzerland), pp. 83–85, 10.1007/978-3-319-07743-7_27.

Belabbes, A., G. Bihlmayer, F. Bechstedt, S Blügel, and A. Manchon, 2016, "Hund's Rule-Driven Dzyaloshinskii-Moriya Interaction at $3d$-$5d$ Interfaces," Phys. Rev. Lett. **117**, 247202.

Belmeguenai, M., H. Bouloussa, Y. Roussigné, M. S. Gabor, T. Petrisor, C. Tiusan, H. Yang, A. Stashkevich, and S. M. Chérif, 2017, "Interface Dzyaloshinskii-Moriya interaction in the interlayer antiferromagnetic-exchange coupled Pt/CoFeB/Ru/CoFeB systems," Phys. Rev. B **96**, 144402.

Belmeguenai, M., M. S. Gabor, Y. Roussigné, T. Petrisor, R. B. Mos, A. Stashkevich, S. M. Chérif, and C. Tiusan, 2018, "Interfacial Dzyaloshinskii-Moriya interaction sign in Ir/Co_2FeAl systems investigated by Brillouin light scattering," Phys. Rev. B **97**, 054425.

Belmeguenai, M., M. S. Gabor, Y. Roussigné, A. Stashkevich, S. M. Chérif, F. Zighem, and C. Tiusan, 2016, "Brillouin light scattering investigation of the thickness dependence of Dzyaloshinskii-Moriya interaction in $Co_{0.5}Fe_{0.5}$ ultrathin films," Phys. Rev. B **93**, 174407.

Belmeguenai, M., Y. Roussigné, S. M. Chérif, A. Stashkevich, T. Petrisor, M. Nasui, and M. S. Gabor, 2019, "Influence of the capping layer material on the interfacial Dzyaloshinskii-Moriya interaction in Pt/Co/capping layer structures probed by Brillouin light scattering," J. Phys. D **52**, 125002.

Belmeguenai, Mohamed, Jean-Paul Adam, Yves Roussigné, Sylvain Eimer, Thibaut Devolder, Joo-Von Kim, Salim Mourad Cherif, Andrey Stashkevich, and André Thiaville, 2015, "Interfacial Dzyaloshinskii-Moriya interaction in perpendicularly magnetized Pt/Co/AlO_x ultrathin films measured by Brillouin light spectroscopy," Phys. Rev. B **91**, 180405(R).

Benguettat-El Mokhtari, I., A. Mourkas, P. Ntetsika, I. Panagiotopoulos, Y. Roussigné, S. M. Cherif, A. Stashkevich, F. Kail, L. Chahed, and M. Belmeguenai, 2019, "Interfacial Dzyaloshinskii-Moriya interaction, interface-induced damping and perpendicular magnetic anisotropy in Pt/Co/W based multilayers," J. Appl. Phys. **126**, 133902.

Benguettat-El Mokhtari, I., D. Ourdani, Y. Roussigné, R. B. Mos, M. Nasui, S. M. Chérif, A. Stashkevich, M. S. Gabor, and M. Belmeguenai, 2020, "Investigation of the correlation between perpendicular magnetic anisotropy, spin mixing conductance and interfacial Dzyaloshinskii-Moriya interaction in CoFeB-based systems," J. Phys. D **53**, 505003..

Benguettat-El Mokhtari, I., Y. Roussigné, S. M. Chérif, A. Stashkevich, S. Auffret, C. Baraduc, M. Gabor, H. Béa, and M. Belmeguenai, 2020, "Interface phenomena in ferromagnet/TaO_x-based systems: Damping, perpendicular magnetic anisotropy, and Dzyaloshinskii-Moriya interaction," Phys. Rev. Mater. **4**, 124408.

Benguettat-El Mokhtari, I., *et al.*, 2020, "Perpendicular magnetic anisotropy and interfacial Dzyaloshinskii-Moriya interaction in as grown and annealed X/Co/Y ultrathin systems," J. Phys. Condens. Matter **32**, 495802.

Benitez, M. J., A. Hrabec, A. P. Mihai, T. A. Moore, G. Burnell, D. McGrouther, C. H. Marrows, and S. McVitie, 2015, "Magnetic microscopy and topological stability of homochiral Néel domain walls in a Pt/Co/AlO_x trilayer," Nat. Commun. **6**, 8957.

Berger, L., 1996, "Emission of spin waves by a magnetic multilayer traversed by a current," Phys. Rev. B **54**, 9353–9358.

Bergqvist, Lars, Andrea Taroni, Anders Bergman, Corina Etz, and Olle Eriksson, 2013, "Atomistic spin dynamics of low-dimensional magnets," Phys. Rev. B **87**, 144401.

Bloch, F., 1932, "Zur theorie des austauschproblems und der remanenzerscheinung der ferromagnetika (On the theory of the exchange problem and the remanence phenomenon of ferromagnetic materials)," Z. Phys. **74**, 295–335.

Bode, M., M. Heide, K. von Bergmann, P. Ferriani, S. Heinze, G. Bihlmayer, A. Kubetzka, O. Pietzsch, S. Blügel, and R. Wiesendanger, 2007, "Chiral magnetic order at surfaces driven by inversion asymmetry," Nature (London) **447**, 190–193.

Bogdanov, A., and A. Hubert, 1994, "Thermodynamically stable magnetic vortex states in magnetic crystals," J. Magn. Magn. Mater. **138**, 255–269.

Bogdanov, A. N., and U. K. Rößler, 2001, "Chiral Symmetry Breaking in Magnetic Thin Films and Multilayers," Phys. Rev. Lett. **87**, 037203.

Bogdanov, A. N., U. K. Rößler, M. Wolf, and K.-H. Müller, 2002, "Magnetic structures and reorientation transitions in noncentrosymmetric uniaxial antiferromagnets," Phys. Rev. B **66**, 214410.

Bogdanov, A. N., and D. A. Yablonskii, 1989, "Thermodynamically stable 'vortices' in magnetically ordered crystals. The mixed state of magnets," Zh. Eksp. Teor. Fiz. **95**, 178–182 [Sov. Phys. JETP **68**, 101 (1989), http://jetp.ras.ru/cgi-bin/e/index/e/68/1/p101?a=list].

Bollero, Alberto, *et al.*, 2020, "An extraordinary chiral exchange-bias phenomenon: Engineering the sign of the bias field in orthogonal bilayers by a magnetically switchable response mechanism," Nanoscale **12**, 1155–1163.

Boulle, O., L. D. Buda-Prejbeanu, M. Miron, and G. Gaudin, 2012, "Current induced domain wall dynamics in the presence of a transverse magnetic field in out-of-plane magnetized materials," J. Appl. Phys. **112**, 053901.

Boulle, O., S. Rohart, L. D. Buda-Prejbeanu, E. Jué, I. M. Miron, S. Pizzini, J. Vogel, G. Gaudin, and A. Thiaville, 2013, "Domain Wall Tilting in the Presence of the Dzyaloshinskii-Moriya Interaction in Out-of-Plane Magnetized Magnetic Nanotracks," Phys. Rev. Lett. **111**, 217203.

Boulle, Olivier, *et al.*, 2016, "Room-temperature chiral magnetic skyrmions in ultrathin magnetic nanostructures," Nat. Nanotechnol. **11**, 449.

Bouloussa, H., R. Ramaswamy, Y. Roussigné, A. Stashkevich, H. Yang, M. Belmeguenai, and S. M. Chérif, 2019, "Pt concentration dependence of the interfacial Dzyaloshinskii-Moriya interaction, the Gilbert damping parameter and the magnetic anisotropy in Py/$Cu_{1-x}Pt_x$ systems," J. Phys. D **52**, 055001.

Bouloussa, H., J. Yu, Y. Roussigné, M. Belmeguenai, A. Stashkevitch, H. Yang, and S. M Chérif, 2018, "Brillouin light scattering investigation of interfacial Dzyaloshinskii-Moriya interaction in ultrathin Co/Pt nanostripe arrays," J. Phys. D **51**, 225005.

Büttner, Felix, *et al.*, 2017, "Field-free deterministic ultrafast creation of magnetic skyrmions by spin-orbit torques," Nat. Nanotechnol. **12**, 1040–1044.

Camley, R. E., 1987, "Nonreciprocal surface waves," Surf. Sci. Rep. **7**, 103–187.

Cao, Anni, Runze Chen, Xinran Wang, Xueying Zhang, Shiyang Lu, Shishen Yan, Bert Koopmans, and Weisheng Zhao, 2020, "Enhanced interfacial Dzyaloshinskii-Moriya interactions in annealed Pt/Co/MgO structures," Nanotechnology **31**, 155705.

Cao, Anni, Youri L. W. van Hees, Reinoud Lavrijsen, Weisheng Zhao, and Bert Koopmans, 2020, "Dynamics of all-optically switched magnetic domains in Co/Gd heterostructures with Dzyaloshinskii-Moriya interaction," Phys. Rev. B **102**, 104412.

Cao, Anni, Xueying Zhang, Bert Koopmans, Shouzhong Peng, Yu Zhang, Zilu Wang, Shaohua Yan, Hongxin Yang, and Weisheng Zhao, 2018, "Tuning the Dzyaloshinskii-Moriya interaction in Pt/Co/MgO heterostructures through the MgO thickness," Nanoscale **10**, 12062–12067.

Cao, Jiangwei, Yifei Chen, Tianli Jin, Weiliang Gan, Ying Wang, Yuqiang Zheng, Hua Lv, Susana Cardoso, Dan Wei, and Wen Siang Lew, 2018, "Spin orbit torques induced magnetization reversal through asymmetric domain wall propagation in Ta/CoFeB/MgO structures," Sci. Rep. **8**, 1355.

Carlotti, G., and G. Gubbiotti, 1999, "Brillouin scattering and magnetic excitations in layered structures," Riv. Nuovo Cimento **22**, 1–60.

Casiraghi, Arianna, Héctor Corte-León, Mehran Vafaee, Felipe Garcia-Sanchez, Gianfranco Durin, Massimo Pasquale, Gerhard Jakob, Mathias Kläui, and Olga Kazakova, 2019, "Individual skyrmion manipulation by local magnetic field gradients," Commun. Phys. **2**, 145.

Chauleau, J-Y., H. G. Bauer, H. S. Körner, J. Stigloher, M. Härtinger, G. Woltersdorf, and C. H. Back, 2014, "Self-consistent determination of the key spin-transfer torque parameters from spin-wave Doppler experiments," Phys. Rev. B **89**, 020403.

Chaurasiya, Avinash Kumar, Chandrima Banerjee, Santanu Pan, Sourav Sahoo, Samiran Choudhury, Jaivardhan Sinha, and Anjan Barman, 2016, "Direct observation of interfacial Dzyaloshinskii-Moriya interaction from asymmetric spin-wave propagation in W/CoFeB/SiO_2 heterostructures down to sub-nanometer CoFeB thickness," Sci. Rep. **6**, 32592.

Chauve, Pascal, Thierry Giamarchi, and Pierre Le Doussal, 2000, "Creep and depinning in disordered media," Phys. Rev. B **62**, 6241–6267.

Chaves, Dayane De Souza, Fernando Ajejas, Viola Křižáková, Jan Vogel, and Stefania Pizzini, 2019, "Oxidation dependence of the Dzyaloshinskii-Moriya interaction in Pt/Co/MO_x trilayers ($M =$ Al or Gd)," Phys. Rev. B **99**, 144404.

Chen, G., *et al.*, 2013, "Novel Chiral Magnetic Domain Wall Structure in Fe/Ni/Cu(001) Films," Phys. Rev. Lett. **110**, 177204.

Chen, Gong, Sang Pyo Kang, Colin Ophus, Alpha T. N'Diaye, Hee Young Kwon, Ryan T. Qiu, Changyeon Won, Kai Liu, Yizheng Wu, and Andreas K. Schmid, 2017, "Out-of-plane chiral domain wall spin-structures in ultrathin in-plane magnets," Nat. Commun. **8**, 15302.

Chen, Gong, Tianping Ma, Alpha T. N'Diaye, Heeyoung Kwon, Changyeon Won, Yizheng Wu, and Andreas K. Schmid, 2013, "Tailoring the chirality of magnetic domain walls by interface engineering," Nat. Commun. **4**, 2671.

Chen, Gong, *et al.*, 2020, "Large Dzyaloshinskii-Moriya interaction induced by chemisorbed oxygen on a ferromagnet surface," Sci. Adv. **6**, eaba4924.

Chen, Gong, *et al.*, 2021, "Observation of Hydrogen-Induced Dzyaloshinskii-Moriya Interaction and Reversible Switching of Magnetic Chirality," Phys. Rev. X **11**, 021015.

Chen, L., M. Decker, M. Kronseder, R. Islinger, M. Gmitra, D. Schuh, D. Bougeard, J. Fabian, D. Weiss, and C. H. Back, 2016, "Robust spin-orbit torque and spin-galvanic effect at the Fe/GaAs (001) interface at room temperature," Nat. Commun. **7**, 13802.

Chen, Tian-Yue, Hsin-I Chan, Wei-Bang Liao, and Chi-Feng Pai, 2018, "Current-Induced Spin-Orbit Torque and Field-Free Switching in Mo-Based Magnetic Heterostructures," Phys. Rev. Appl. **10**, 044038.

Chen, Yifei, Qihan Zhang, Junxue Jia, Yuqiang Zheng, Ying Wang, Xiaolong Fan, and Jiangwei Cao, 2018, "Tuning Slonczewski-like torque and Dzyaloshinskii-Moriya interaction by inserting a Pt spacer layer in Ta/CoFeB/MgO structures," Appl. Phys. Lett. **112**, 232402.

Cho, Jaehun, Nam-Hui Kim, Seung Ku Kang, Hee-Kyeong Hwang, Jinyoung Jung, Henk J. M. Swagten, June-Seo Kim, and Chun-Yeol You, 2017, "The sign of the interfacial Dzyaloshinskii-Moriya interaction in ultrathin amorphous and polycrystalline magnetic films," J. Phys. D **50**, 425004.

Cho, Jaehun, *et al.*, 2015, "Thickness dependence of the interfacial Dzyaloshinskii-Moriya interaction in inversion symmetry broken systems," Nat. Commun. **6**, 7635.

Choe, Sug-Bong, and Chun-Yeol You, 2018, "Experimental determination schemes of Dzyaloshinskii-Moriya interaction," J. Korean Phys. Soc. **73**, 238–241.

Ciubotaru, F., T. Devolder, M. Manfrini, C. Adelmann, and I. P. Radu, 2016, "All electrical propagating spin wave spectroscopy with broadband wavevector capability," Appl. Phys. Lett. **109**, 012403.

Coffey, D., T. M. Rice, and F. C. Zhang, 1991, "Dzyaloshinskii-Moriya interaction in the cuprates," Phys. Rev. B **44**, 10112–10116.

Consolo, G., and E. Martinez, 2012, "The effect of dry friction on domain wall dynamics: A micromagnetic study," J. Appl. Phys. **111**, 07D312.

Corredor, Edna C., Susanne Kuhrau, Fabian Kloodt-Twesten, Robert Frömter, and Hans Peter Oepen, 2017, "SEMPA investigation of the Dzyaloshinskii-Moriya interaction in the single, ideally grown Co/Pt(111) interface," Phys. Rev. B **96**, 060410(R).

Cortés-Ortuño, D., and P. Landeros, 2013, "Influence of the Dzyaloshinskii-Moriya interaction on the spin-wave spectra of thin films," J. Phys. Condens. Matter **25**, 156001.

Costa, A. T., R. B. Muniz, S. Lounis, A. B. Klautau, and D. L. Mills, 2010, "Spin-orbit coupling and spin waves in ultrathin ferromagnets: The spin-wave Rashba effect," Phys. Rev. B **82**, 014428.

Costa, A. T., R. B. Muniz, and D. L. Mills, 2003, "Theory of spin excitations in Fe(110) multilayers," Phys. Rev. B **68**, 224435.

Crépieux, A., and C. Lacroix, 1998, "Dzyaloshinsky-Moriya interactions induced by symmetry breaking at a surface," J. Magn. Magn. Mater. **182**, 341–349.

Davydenko, A. V., A. G. Kozlov, A. G. Kolesnikov, M. E. Stebliy, G. S. Suslin, Yu. E. Vekovshinin, A. V. Sadovnikov, and S. A. Nikitov, 2019, "Dzyaloshinskii-Moriya interaction in symmetric epitaxial $[\mathrm{Co/Pd}(111)]_N$ superlattices with different numbers of Co/Pd bilayers," Phys. Rev. B **99**, 014433.

Deger, Caner, 2020, "Strain-enhanced Dzyaloshinskii-Moriya interaction at Co/Pt interfaces," Sci. Rep. **10**, 12314.

del Real, Rafael P., Victor Raposo, Eduardo Martinez, and Masamitsu Hayashi, 2017, "Current-induced generation and synchronous motion of highly packed coupled chiral domain walls," Nano Lett. **17**, 1814–1818.

de Souza Chaves, Dayane, Fernando Ajejas, Viola Křižáková, Jan Vogel, and Stefania Pizzini, 2019, "Oxidation dependence of the Dzyaloshinskii-Moriya interaction in Pt/Co/MO_x trilayers ($M =$ Al or Gd)," Phys. Rev. B **99**, 144404.

Di, Kai, Vanessa Li Zhang, Hock Siah Lim, Ser Choon Ng, Meng Hau Kuok, Xuepeng Qiu, and Hyunsoo Yang, 2015a, "Asymmetric spin-wave dispersion due to Dzyaloshinskii-Moriya interaction in an ultrathin Pt/CoFeB film," Appl. Phys. Lett. **106**, 052403.

Di, Kai, Vanessa Li Zhang, Hock Siah Lim, Ser Choon Ng, Meng Hau Kuok, Jiawei Yu, Jungbum Yoon, Xuepeng Qiu, and Hyunsoo Yang, 2015b, "Direct Observation of the Dzyaloshinskii-Moriya Interaction in a Pt/Co/Ni Film," Phys. Rev. Lett. **114**, 047201.

Dieny, B., *et al.*, 2020, "Opportunities and challenges for spintronics in the microelectronics industry," Nat. Electron. **3**, 446–459.

Diez, L. Herrera, *et al.*, 2019a, "Nonvolatile Ionic Modification of the Dzyaloshinskii-Moriya Interaction," Phys. Rev. Appl. **12**, 034005.

Diez, L. Herrera, *et al.*, 2019b, "Enhancement of the Dzyaloshinskii-Moriya interaction and domain wall velocity through interface intermixing in Ta/CoFeB/MgO," Phys. Rev. B **99**, 054431.

Dillon, Jr., J. F., 1963, "Domains and domain walls," in *Magnetism*, Vol. III, edited by G. T. Rado and H. Suhl (Academic, New York).

Ding, Shilei, Lorenzo Baldrati, Andrew Ross, Zengyao Ren, Rui Wu, Sven Becker, Jinbo Yang, Gerhard Jakob, Arne Brataas, and Mathias Kläui, 2020a, "Identifying the origin of the nonmonotonic thickness dependence of spin-orbit torque and interfacial Dzyaloshinskii-Moriya interaction in a ferrimagnetic insulator heterostructure," Phys. Rev. B **102**, 054425.

Ding, Shilei, *et al.*, 2019, "Interfacial Dzyaloshinskii-Moriya interaction and chiral magnetic textures in a ferrimagnetic insulator," Phys. Rev. B **100**, 100406.

Ding, Shilei, *et al.*, 2020, "Harnessing Orbital-to-Spin Conversion of Interfacial Orbital Currents for Efficient Spin-Orbit Torques," Phys. Rev. Lett. **125**, 177201.

Dohi, Takaaki, Samik DuttaGupta, Shunsuke Fukami, and Hideo Ohno, 2019, "Reversal of domain wall chirality with ferromagnet thickness in W/(Co)FeB/MgO systems," Appl. Phys. Lett. **114**, 042405.

dos Santos, Flaviano José, Manuel dos Santos Dias, Filipe Souza Mendes Guimarães, Juba Bouaziz, and Samir Lounis, 2018, "Spin-resolved inelastic electron scattering by spin waves in noncollinear magnets," Phys. Rev. B **97**, 024431.

dos Santos, Flaviano José, Manuel dos Santos Dias, and Samir Lounis, 2020, "Nonreciprocity of spin waves in noncollinear magnets due to the Dzyaloshinskii-Moriya interaction," Phys. Rev. B **102**, 104401.

Dugato, D. A., J. Brandão, R. L. Seeger, F. Béron, J. C. Cezar, L. S. Dorneles, and T. J. A. Mori, 2019, "Magnetic domain size tuning in asymmetric Pd/Co/W/Pd multilayers with perpendicular magnetic anisotropy," Appl. Phys. Lett. **115**, 182408.

Duine, R. A., Kyung-Jin Lee, Stuart S. P. Parkin, and M. D. Stiles, 2018, "Synthetic antiferromagnetic spintronics," Nat. Phys. **14**, 217.

Dzyaloshinskii, I. E., 1958, "A thermodynamic theory of 'weak' ferromagnetism of antiferromagnetics," J. Phys. Chem. Solids **4**, 241–255.

Emori, Satoru, Uwe Bauer, Sung-Min Ahn, Eduardo Martinez, and Geoffrey S. D. Beach, 2013, "Current-driven dynamics of chiral ferromagnetic domain walls," Nat. Mater. **12**, 611.

Emori, Satoru, Eduardo Martinez, Kyung-Jin Lee, Hyun-Woo Lee, Uwe Bauer, Sung-Min Ahn, Parnika Agrawal, David C. Bono, and Geoffrey S. D. Beach, 2014, "Spin Hall torque magnetometry of Dzyaloshinskii domain walls," Phys. Rev. B **90**, 184427.

Emtage, P. R., 1978, "Interaction of magnetostatic waves with a current," J. Appl. Phys. **49**, 4475–4484.

Fernández-Pacheco, Amalio, Elena Vedmedenko, Fanny Ummelen, Rhodri Mansell, Dorothée Petit, and Russell P. Cowburn, 2019, "Symmetry-breaking interlayer Dzyaloshinskii-Moriya interactions in synthetic antiferromagnets," Nat. Mater. **18**, 679–684.

Ferriani, P., K. von Bergmann, E. Y. Vedmedenko, S. Heinze, M. Bode, M. Heide, G. Bihlmayer, S. Blügel, and R. Wiesendanger, 2008, "Atomic-Scale Spin Spiral with a Unique Rotational Sense: Mn Monolayer on W(001)," Phys. Rev. Lett. **101**, 027201.

Fert, A., and Peter M. Levy, 1980, "Role of Anisotropic Exchange Interactions in Determining the Properties of Spin-Glasses," Phys. Rev. Lett. **44**, 1538–1541.

Fert, A. R., 1991, "Magnetic and transport properties of metallic multilayers," in *Metallic Multilayers*, Materials Science Forum Vol. 59, edited by A. Chamberod and J. Hillairet (Trans Tech Publications, Stafa-Zurich), pp. 439–480, 10.4028/www.scientific.net/MSF.59-60.439.

Finocchio, Giovanni, Felix Büttner, Riccardo Tomasello, Mario Carpentieri, and Mathias Kläui, 2016, "Magnetic skyrmions: From fundamental to applications," J. Phys. D **49**, 423001.

Fischer, Jeison A., Leonid M. Sandratskii, Soo-hyon Phark, Dirk Sander, and Stuart Parkin, 2017, "Atomic structure governed diversity of exchange-driven spin helices in Fe nanoislands: Experiment and theory," Phys. Rev. B **96**, 140407.

Franken, J. H., M. Herps, H. J. M. Swagten, and B. Koopmans, 2014, "Tunable chiral spin texture in magnetic domain-walls," Sci. Rep. **4**, 5248.

Furuta, M., Y. Liu, H. Sepehri-Amin, K. Hono, and J. Zhu, 2017, "Annealing effect on current-driven domain wall motion in Pt/[Co/Ni] wire," J. Appl. Phys. **122**, 113901.

Gallardo, R. A., D. Cortés-Ortuño, T. Schneider, A. Roldán-Molina, Fusheng Ma, R. E. Troncoso, K. Lenz, H. Fangohr, J. Lindner, and P. Landeros, 2019, "Flat Bands, Indirect Gaps, and Unconventional Spin-Wave Behavior Induced by a Periodic Dzyaloshinskii-Moriya Interaction," Phys. Rev. Lett. **122**, 067204.

Gallardo, R. A., D. Cortés-Ortuño, R. E. Troncoso, and P. Landeros, 2019, "Spin-waves in thin films and magnonic crystals with Dzyaloshinskii-Moriya interactions," in *Three-Dimensional Magnonics: Layered, Micro- and Nanostructures*, edited by G. Gubbiotti (Jenny Stanford Publishing, Singapore), p. 121.

Garlow, Joseph A., Shawn D. Pollard, Marco Beleggia, Tanmay Dutta, Hyunsoo Yang, and Yimei Zhu, 2019, "Quantification of Mixed Bloch-Néel Topological Spin Textures Stabilized by the Dzyaloshinskii-Moriya Interaction in Co/Pd Multilayers," Phys. Rev. Lett. **122**, 237201.

Géhanne, P., S. Rohart, A. Thiaville, and V. Jeudy, 2020, "Strength and length scale of the interaction between domain walls and pinning disorder in thin ferromagnetic films," Phys. Rev. Res. **2**, 043134.

Gladii, O., M. Collet, Y. Henry, J.-V. Kim, A. Anane, and M. Bailleul, 2020, "Determining Key Spin-Orbitronic Parameters via Propagating Spin Waves," Phys. Rev. Appl. **13**, 014016.

Gladii, O., M. Haidar, Y. Henry, M. Kostylev, and M. Bailleul, 2016, "Frequency nonreciprocity of surface spin wave in Permalloy thin films," Phys. Rev. B **93**, 054430.

Grassi, Matías Pablo, Alejandro B. Kolton, Vincent Jeudy, Alexandra Mougin, Sebastian Bustingorry, and Javier Curiale, 2018, "Intermittent collective dynamics of domain walls in the creep regime," Phys. Rev. B **98**, 224201.

Gross, I., *et al.*, 2016, "Direct measurement of interfacial Dzyaloshinskii-Moriya interaction in $X|$CoFeB$|$MgO heterostructures with a scanning NV magnetometer ($X =$ Ta, TaN, and W)," Phys. Rev. B **94**, 064413.

Gurevich, A. G., 1996, *Magnetization Oscillations and Waves* (CRC Press, Boca Raton).

Gusev, N. S., A. V. Sadovnikov, S. A. Nikitov, M. V. Sapozhnikov, and O. G. Udalov, 2020, "Manipulation of the Dzyaloshinskii-Moriya Interaction in Co/Pt Multilayers with Strain," Phys. Rev. Lett. **124**, 157202.

Haazen, P. P. J., E. Murè, J. H. Franken, R. Lavrijsen, H. J. M. Swagten, and B. Koopmans, 2013, "Domain wall depinning governed by the spin Hall effect," Nat. Mater. **12**, 299.

Han, Dong-Soo, *et al.*, 2016, "Asymmetric hysteresis for probing Dzyaloshinskii-Moriya interaction," Nano Lett. **16**, 4438–4446.

Han, Dong-Soo, *et al.*, 2019, "Long-range chiral exchange interaction in synthetic antiferromagnets," Nat. Mater. **18**, 703–708.

Hartmann, Dion M. F., Rembert A. Duine, Mariëlle J. Meijer, Henk J. M. Swagten, and Reinoud Lavrijsen, 2019, "Creep of chiral domain walls," Phys. Rev. B **100**, 094417.

Hayashi, Masamitsu, Yoshinobu Nakatani, Shunsuke Fukami, Michihiko Yamanouchi, Seiji Mitani, and Hideo Ohno, 2012, "Domain wall dynamics driven by spin transfer torque and the spin-orbit field," J. Phys. Condens. Matter **24**, 024221.

Heide, M., G. Bihlmayer, and S. Blügel, 2008, "Dzyaloshinskii-Moriya interaction accounting for the orientation of magnetic domains in ultrathin films: Fe/W(110)," Phys. Rev. B **78**, 140403.

Heinze, S., 2000, "Real-space imaging of two-dimensional antiferromagnetism on the atomic scale," Science **288**, 1805–1808.

Heinze, S., 2006, "Simulation of spin-polarized scanning tunneling microscopy images of nanoscale non-collinear magnetic structures," Appl. Phys. A **85**, 407–414.

Heinze, Stefan, Kirsten von Bergmann, Matthias Menzel, Jens Brede, André Kubetzka, Roland Wiesendanger, Gustav Bihlmayer, and Stefan Blügel, 2011, "Spontaneous atomic-scale magnetic skyrmion lattice in two dimensions," Nat. Phys. **7**, 713–718.

Hellman, Frances, *et al.*, 2017, "Interface-induced phenomena in magnetism," Rev. Mod. Phys. **89**, 025006.

Hillebrands, B., P. Baumgart, and G. Güntherodt, 1987, "*In situ* Brillouin scattering from surface-anisotropy-dominated Damon-Eshbach modes in ultrathin epitaxial Fe(110) layers," Phys. Rev. B **36**, 2450–2453.

Hillebrands, Burkard, 1990, "Spin-wave calculations for multilayered structures," Phys. Rev. B **41**, 530–540.

Hiramatsu, Ryo, Kab-Jin Kim, Yoshinobu Nakatani, Takahiro Moriyama, and Teruo Ono, 2014, "Proposal for quantifying the Dzyaloshinsky-Moriya interaction by domain walls annihilation measurement," Jpn. J. Appl. Phys. **53**, 108001.

Holstein, T., and H. Primakoff, 1940, "Field dependence of the intrinsic domain magnetization of a ferromagnet," Phys. Rev. **58**, 1098–1113.

Hrabec, A., N. A. Porter, A. Wells, M. J. Benitez, G. Burnell, S. McVitie, D. McGrouther, T. A. Moore, and C. H. Marrows, 2014, "Measuring and tailoring the Dzyaloshinskii-Moriya interaction in perpendicularly magnetized thin films," Phys. Rev. B **90**, 020402(R).

Hsu, Pin-Jui, *et al.*, 2018, "Inducing skyrmions in ultrathin Fe films by hydrogen exposure," Nat. Commun. **9**, 1571.

Ishikuro, Yuto, Masashi Kawaguchi, Naoaki Kato, Yong-Chang Lau, and Masamitsu Hayashi, 2019, "Dzyaloshinskii-Moriya interaction and spin-orbit torque at the Ir/Co interface," Phys. Rev. B **99**, 134421.

Jaiswal, S., *et al.*, 2017, "Investigation of the Dzyaloshinskii-Moriya interaction and room temperature skyrmions in W/CoFeB/MgO thin films and microwires," Appl. Phys. Lett. **111**, 022409.

Je, Soong-Geun, Duck-Ho Kim, Sang-Cheol Yoo, Byoung-Chul Min, Kyung-Jin Lee, and Sug-Bong Choe, 2013, "Asymmetric magnetic domain-wall motion by the Dzyaloshinskii-Moriya interaction," Phys. Rev. B **88**, 214401.

Jena, Sukanta Kumar, *et al.*, 2021, "Interfacial Dzyaloshinskii-Moriya interaction in the epitaxial W/Co/Pt multilayers," Nanoscale **13**, 7685–7693.

Jué, E., *et al.*, 2016a, "Domain wall dynamics in ultrathin Pt/Co/AlO$_x$ microstrips under large combined magnetic fields," Phys. Rev. B **93**, 014403.

Jué, Emilie, *et al.*, 2016b, "Chiral damping of magnetic domain walls," Nat. Mater. **15**, 272–277.

Kabanov, Y. P., Y. L. Iunin, V. I. Nikitenko, A. J. Shapiro, R. D. Shull, L. Y. Zhu, and C. L. Chien, 2010, "In-plane field effects on the dynamics of domain walls in ultrathin Co films with perpendicular anisotropy," IEEE Trans. Magn. **46**, 2220–2223.

Kalinikos, B. A., 1981, "Spectrum and linear excitation of spin waves in ferromagnetic films," Sov. Phys. J. **24**, 718–731.

Kalinikos, B. A., 1994, "Dipole-exchange spin-wave spectrum of magnetic films," in *Linear and Nonlinear Spin Waves in Magnetic Films and Superlattices*, edited by M. G. Cottam (World Scientific, Singapore), pp. 89–156, 10.1142/9789814343121_0002.

Kalinikos, B. A., and A. N. Slavin, 1986, "Theory of dipole-exchange spin wave spectrum for ferromagnetic films with mixed exchange boundary conditions," J. Phys. C **19**, 7013–7033.

Karakas, Vedat, *et al.*, 2018, "Observation of magnetic radial vortex nucleation in a multilayer stack with tunable anisotropy," Sci. Rep. **8**, 7180.

Karnad, G. V., F. Freimuth, E. Martinez, R. Lo Conte, G. Gubbiotti, T. Schulz, S. Senz, B. Ocker, Y. Mokrousov, and M. Kläui, 2018, "Modification of Dzyaloshinskii-Moriya-Interaction-Stabilized Domain Wall Chirality by Driving Currents," Phys. Rev. Lett. **121**, 147203.

Kasukawa, Shuhei, Yoichi Shiota, Takahiro Moriyama, and Teruo Ono, 2018, "Evaluation of electric field effect on interface magnetic properties by propagating spin wave in Pt/Co/MgO structures," Jpn. J. Appl. Phys. **57**, 080309.

Kataoka, Mitsuo, 1987, "Spin waves in systems with long period helical spin density waves due to the antisymmetric and symmetric exchange interactions," J. Phys. Soc. Jpn. **56**, 3635.

Khadka, Durga, Sabit Karayev, and S. X. Huang, 2018, "Dzyaloshinskii-Moriya interaction in Pt/Co/Ir and Pt/Co/Ru multilayer films," J. Appl. Phys. **123**, 123905.

Khan, R. A., P. M. Shepley, A. Hrabec, A. W. J. Wells, B. Ocker, C. H. Marrows, and T. A. Moore, 2016, "Effect of annealing on the interfacial Dzyaloshinskii-Moriya interaction in Ta/CoFeB/MgO trilayers," Appl. Phys. Lett. **109**, 132404.

Khan, Risalat A., Hans T. Nembach, Mannan Ali, Justin M. Shaw, Christopher H. Marrows, and Thomas A. Moore, 2018, "Magnetic domain texture and the Dzyaloshinskii-Moriya interaction in Pt/Co/IrMn and Pt/Co/FeMn thin films with perpendicular exchange bias," Phys. Rev. B **98**, 064413.

Khvalkovskiy, A. V., V. Cros, D. Apalkov, V. Nikitin, M. Krounbi, K. A. Zvezdin, A. Anane, J. Grollier, and A. Fert, 2013, "Matching domain-wall configuration and spin-orbit torques for efficient domain-wall motion," Phys. Rev. B **87**, 020402.

Kim, Dae-Yun, Duck-Ho Kim, and Sug-Bong Choe, 2016, "Intrinsic asymmetry in chiral domain walls due to the Dzyaloshinskii-Moriya interaction," Appl. Phys. Express **9**, 053001.

Kim, Dae-Yun, Duck-Ho Kim, Joon Moon, and Sug-Bong Choe, 2015, "Determination of magnetic domain-wall types using Dzyaloshinskii-Moriya interaction induced domain patterns," Appl. Phys. Lett. **106**, 262403.

Kim, Dae-Yun, Min-Ho Park, Yong-Keun Park, Joo-Sung Kim, Yune-Seok Nam, Duck-Ho Kim, Soong-Geun Je, Hyeok-Cheol Choi, Byoung-Chul Min, and Sug-Bong Choe, 2018, "Chirality-induced antisymmetry in magnetic domain wall speed," NPG Asia Mater. **10**, e464.

Kim, Dae-Yun, *et al.*, 2019, "Quantitative accordance of Dzyaloshinskii-Moriya interaction between domain-wall and spin-wave dynamics," Phys. Rev. B **100**, 224419.

Kim, Duck-Ho, Dae-Yun Kim, Sang-Cheol Yoo, Byoung-Chul Min, and Sug-Bong Choe, 2019, "Universality of Dzyaloshinskii-Moriya interaction effect over domain-wall creep and flow regimes," Phys. Rev. B **99**, 134401.

Kim, Duck-Ho, Sang-Cheol Yoo, Dae-Yun Kim, Byoung-Chul Min, and Sug-Bong Choe, 2017, "Wide-range probing of Dzyaloshinskii-Moriya interaction," Sci. Rep. **7**, 45498.

Kim, Gyu Won, Alexander S. Samardak, Yong Jin Kim, In Ho Cha, Alexey V. Ognev, Alexandr V. Sadovnikov, Sergey A. Nikitov, and Young Keun Kim, 2018, "Role of the Heavy Metal's Crystal

Phase in Oscillations of Perpendicular Magnetic Anisotropy and the Interfacial Dzyaloshinskii-Moriya Interaction in W/Co-Fe-B/MgO Films," Phys. Rev. Appl. **9**, 064005.

Kim, Kyoung-Whan, Hyun-Woo Lee, Kyung-Jin Lee, and M. D. Stiles, 2013, "Chirality from Interfacial Spin-Orbit Coupling Effects in Magnetic Bilayers," Phys. Rev. Lett. **111**, 216601.

Kim, Nam-Hui, Dong-Soo Han, Jinyong Jung, Jaehun Cho, June-Seo Kim, Henk J. M. Swagten, and Chun-Yeol You, 2015, "Improvement of the interfacial Dzyaloshinskii-Moriya interaction by introducing a Ta buffer layer," Appl. Phys. Lett. **107**, 142408.

Kim, Nam-Hui, Dong-Soo Han, Jinyong Jung, Kwonjin Park, Henk J. M. Swagten, June-Seo Kim, and Chun-Yeol You, 2017, "Dependence of interfacial Dzyaloshinskii-Moriya interaction and perpendicular magnetic anisotropy on the thickness of the heavy-metal layer," Appl. Phys. Express **10**, 103003.

Kim, Nam-Hui, Jinyong Jung, Jaehun Cho, Dong-Soo Han, Yuxiang Yin, June-Seo Kim, Henk J. M. Swagten, and Chun-Yeol You, 2016, "Interfacial Dzyaloshinskii-Moriya interaction, surface anisotropy energy, and spin pumping at spin orbit coupled Ir/Co interface," Appl. Phys. Lett. **108**, 142406.

Kim, Sanghoon, Peong-Hwa Jang, Duck-Ho Kim, Mio Ishibashi, Takuya Taniguchi, Takahiro Moriyama, Kab-Jin Kim, Kyung-Jin Lee, and Teruo Ono, 2017, "Magnetic droplet nucleation with a homochiral Néel domain wall," Phys. Rev. B **95**, 220402(R).

Kim, Sanghoon, *et al.*, 2018, "Correlation of the Dzyaloshinskii-Moriya interaction with Heisenberg exchange and orbital asphericity," Nat. Commun. **9**, 1648.

Kim, Woo-Yeong, Hyung Keun Gweon, Kyung-Jin Lee, and Chun-Yeol You, 2019, "Correlation between interfacial Dzyaloshinskii-Moriya interaction and interfacial magnetic anisotropy of Pt/Co/MgO structures," Appl. Phys. Express **12**, 053007.

Kloodt-Twesten, Fabian, Susanne Kuhrau, Hans Peter Oepen, and Robert Frömter, 2019, "Measuring the Dzyaloshinskii-Moriya interaction of the epitaxial Co/Ir(111) interface," Phys. Rev. B **100**, 100402.

Kolesnikov, A. G., *et al.*, 2021, "Magnetic properties and the interfacial Dzyaloshinskii-Moriya interaction in exchange biased Pt/Co/Ni$_x$O$_y$ films," Appl. Surf. Sci. **543**, 148720.

Kooy, C., and U. Enz, 1960, "Experimental and theoretical study of the domain configuration in thin layers of BaFe$_{12}$O$_{19}$," Philips Res. Rep. **15**, 7–29, https://www.pearl-hifi.com/06_Lit_Archive/02_PEARL_Arch/Vol_16/Sec_53/Philips_Rsrch_Reports_1946_thru_1977/Philips%20Research%20Reports-15-1960.pdf.

Körner, H. S., J. Stigloher, H. G. Bauer, H. Hata, T. Taniguchi, T. Moriyama, T. Ono, and C. H. Back, 2015, "Interfacial Dzyaloshinskii-Moriya interaction studied by time-resolved scanning Kerr microscopy," Phys. Rev. B **92**, 220413(R).

Kostylev, M., 2014, "Interface boundary conditions for dynamic magnetization and spin wave dynamics in a ferromagnetic layer with the interface Dzyaloshinskii-Moriya interaction," J. Appl. Phys. **115**, 233902.

Koyama, T., *et al.*, 2011, "Observation of the intrinsic pinning of a magnetic domain wall in a ferromagnetic nanowire," Nat. Mater. **10**, 194.

Kozlov, A. G., A. G. Kolesnikov, M. E. Stebliy, A. P. Golikov, and A. V. Davydenko, 2020, "Domain-period method for determination of the energy of the Dzyaloshinskii-Moriya interaction in $[\mathrm{Co/Pd}(111)]_5$ superlattices," Phys. Rev. B **102**, 144411.

Krizakova, V., J. Peña Garcia, J. Vogel, N. Rougemaille, D. de Souza Chaves, S. Pizzini, and A. Thiaville, 2019, "Study of the velocity plateau of Dzyaloshinskii domain walls," Phys. Rev. B **100**, 214404.

Kubetzka, A., O. Pietzsch, M. Bode, and R. Wiesendanger, 2003, "Spin-polarized scanning tunneling microscopy study of 360° walls in an external magnetic field," Phys. Rev. B **67**, 020401.

Küß, M., M. Heigl, L. Flacke, A. Hörner, M. Weiler, M. Albrecht, and A. Wixforth, 2020, "Nonreciprocal Dzyaloshinskii-Moriya Magnetoacoustic Waves," Phys. Rev. Lett. **125**, 217203.

Kuświk, P., M. Matczak, M. Kowacz, and K. Szuba-Jabłoński, N. Michalak, B. Szymański, A. Ehresmann, and F. Stobiecki, 2018, "Asymmetric domain wall propagation caused by interfacial Dzyaloshinskii-Moriya interaction in exchange biased Au/Co/NiO layered system," Phys. Rev. B **97**, 024404.

Lau, D., J. P. Pellegren, H. T. Nembach, J. M. Shaw, and V. Sokalski, 2018, "Disentangling factors governing Dzyaloshinskii domain-wall creep in Co/Ni thin films using Pt$_x$Ir$_{1-x}$ seed layers," Phys. Rev. B **98**, 184410.

Lau, Derek, Vignesh Sundar, Jian-Gang Zhu, and Vincent Sokalski, 2016, "Energetic molding of chiral magnetic bubbles," Phys. Rev. B **94**, 060401(R).

Lavrijsen, R., D. M. F. Hartmann, A. van den Brink, Y. Yin, B. Barcones, R. A. Duine, M. A. Verheijen, H. J. M. Swagten, and B. Koopmans, 2015, "Asymmetric magnetic bubble expansion under in-plane field in Pt/Co/Pt: Effect of interface engineering," Phys. Rev. B **91**, 104414.

Lee, Aidan J., Adam S. Ahmed, Jose Flores, Side Guo, Binbin Wang, Nuria Bagués, David W. McComb, and Fengyuan Yang, 2020, "Probing the Source of the Interfacial Dzyaloshinskii-Moriya Interaction Responsible for the Topological Hall Effect in Metal/Tm$_3$Fe$_5$O$_{12}$ Systems," Phys. Rev. Lett. **124**, 107201.

Lee, Jong Min, Chaun Jang, Byoung-Chul Min, Seo-Won Lee, Kyung-Jin Lee, and Joonyeon Chang, 2016, "All-electrical measurement of interfacial Dzyaloshinskii-Moriya interaction using collective spin-wave dynamics," Nano Lett. **16**, 62–67.

Legrand, William, Jean-Yves Chauleau, Davide Maccariello, Nicolas Reyren, Sophie Collin, Karim Bouzehouane, Nicolas Jaouen, Vincent Cros, and Albert Fert, 2018, "Hybrid chiral domain walls and skyrmions in magnetic multilayers," Sci. Adv. **4**, eaat0415.

Legrand, William, Davide Maccariello, Fernando Ajejas, Sophie Collin, Aymeric Vecchiola, Karim Bouzehouane, Nicolas Reyren, Vincent Cros, and Albert Fert, 2020, "Room-temperature stabilization of antiferromagnetic skyrmions in synthetic antiferromagnets," Nat. Mater. **19**, 34–42.

Lemerle, S., J. Ferré, C. Chappert, V. Mathet, T. Giamarchi, and P. Le Doussal, 1998, "Domain Wall Creep in an Ising Ultrathin Magnetic Film," Phys. Rev. Lett. **80**, 849–852.

Lemesh, Ivan, and Geoffrey S. D. Beach, 2018, "Twisted domain walls and skyrmions in perpendicularly magnetized multilayers," Phys. Rev. B **98**, 104402.

Lemesh, Ivan, and Geoffrey S. D. Beach, 2019, "Walker Breakdown with a Twist: Dynamics of Multilayer Domain Walls and Skyrmions Driven by Spin-Orbit Torque," Phys. Rev. Appl. **12**, 044031.

Lemesh, Ivan, Felix Büttner, and Geoffrey S. D. Beach, 2017, "Accurate model of the stripe domain phase of perpendicularly magnetized multilayers," Phys. Rev. B **95**, 174423.

Lemesh, Ivan, *et al.*, 2018, "Current-induced skyrmion generation through morphological thermal transitions in chiral ferromagnetic heterostructures," Adv. Mater. **30**, 1805461.

Levy, Peter M., and A. Fert, 1981, "Anisotropy induced by nonmagnetic impurities in Cu Mn spin-glass alloys," Phys. Rev. B **23**, 4667–4690.

Lin, T., *et al.*, 2018, "Observation of room-temperature magnetic skyrmions in Pt/Co/W structures with a large spin-orbit coupling," Phys. Rev. B **98**, 174425.

Lin, Weinan, *et al.*, 2020, “Perpendicular Magnetic Anisotropy and Dzyaloshinskii-Moriya Interaction at an Oxide/Ferromagnetic Metal Interface,” Phys. Rev. Lett. **124**, 217202.

Litzius, Kai, *et al.*, 2017, “Skyrmion Hall effect revealed by direct time-resolved x-ray microscopy,” Nat. Phys. **13**, 170–175.

Liu, Chuanpu, *et al.*, 2018, “Long-distance propagation of short-wavelength spin waves,” Nat. Commun. **9**, 738.

Liu, Luqiao, Chi-Feng Pai, Y. Li, H. W. Tseng, D. C. Ralph, and R. A. Buhrman, 2012, “Spin-torque switching with the giant spin Hall effect of tantalum,” Science **336**, 555–558.

Lo Conte, R., *et al.*, 2015, “Role of B diffusion in the interfacial Dzyaloshinskii-Moriya interaction in $\mathrm{Ta/Co_{20}Fe_{60}B_{20}/MgO}$ nanowires,” Phys. Rev. B **91**, 014433.

Lo Conte, R., *et al.*, 2017, “Ferromagnetic layer thickness dependence of the Dzyaloshinskii-Moriya interaction and spin-orbit torques in $\mathrm{PtCoAlO}_x$,” AIP Adv. **7**, 065317.

Lucassen, Juriaan, *et al.*, 2020, “Extraction of Dzyaloshinskii-Moriya interaction from propagating spin waves,” Phys. Rev. B **101**, 064432.

Luo, H. M., Y. Y. Hsu, B. N. Lin, Y. P. Chi, T. J. Lee, and H. C. Ku, 1999, “Correlation between weak ferromagnetism and crystal symmetry in $\mathrm{Gd_2CuO_4}$-type cuprates,” Phys. Rev. B **60**, 13119–13124.

Ma, Xin, Guoqiang Yu, Seyed A. Razavi, Stephen S. Sasaki, Xiang Li, Kai Hao, Sarah H. Tolbert, Kang L. Wang, and Xiaoqin Li, 2017, “Dzyaloshinskii-Moriya Interaction across an Antiferromagnet-Ferromagnet Interface,” Phys. Rev. Lett. **119**, 027202.

Ma, Xin, Guoqiang Yu, Chi Tang, Xiang Li, Congli He, Jing Shi, Kang L. Wang, and Xiaoqin Li, 2018, “Interfacial Dzyaloshinskii-Moriya Interaction: Effect of 5*d* Band Filling and Correlation with Spin Mixing Conductance,” Phys. Rev. Lett. **120**, 157204.

Ma, Xin, *et al.*, 2016, “Interfacial control of Dzyaloshinskii-Moriya interaction in heavy metal/ferromagnetic metal thin film heterostructures,” Phys. Rev. B **94**, 180408(R).

Magni, A., *et al.*, 2022, “Key points in the determination of the interfacial Dzyaloshinskii-Moriya interaction from asymmetric bubble domain expansion,” IEEE Trans. Magn. **58**, 1–16.

Málek, Z., and V. Kamberský, 1958, “On the theory of the domain structure of thin films of magnetically uni-axial materials,” Czech. J. Phys. **8**, 416–421.

Malozemoff, A. P., and J. C. Slonczewski, 1979, *Magnetic Domain Walls in Bubble Materials*, edited by Raymond Wolfe (Academic Press, New York).

Manchon, A., J. Železný, I. M. Miron, T. Jungwirth, J. Sinova, A. Thiaville, K. Garello, and P. Gambardella, 2019, “Current-induced spin-orbit torques in ferromagnetic and antiferromagnetic systems,” Rev. Mod. Phys. **91**, 035004.

Martinez, E., L. Lopez-Diaz, L. Torres, C. Tristan, and O. Alejos, 2007, “Thermal effects in domain wall motion: Micromagnetic simulations and analytical model,” Phys. Rev. B **75**, 174409.

Martinez, Eduardo, Satoru Emori, and Geoffrey S. D. Beach, 2013, “Current-driven domain wall motion along high perpendicular anisotropy multilayers: The role of the Rashba field, the spin Hall effect, and the Dzyaloshinskii-Moriya interaction,” Appl. Phys. Lett. **103**, 072406.

Martinez, Eduardo, Satoru Emori, Noel Perez, Luis Torres, and Geoffrey S. D. Beach, 2014, “Current-driven dynamics of Dzyaloshinskii domain walls in the presence of in-plane fields: Full micromagnetic and one-dimensional analysis,” J. Appl. Phys. **115**, 213909.

Martinez, Eduardo, Giovanni Finocchio, Luis Torres, and Luis Lopez-Diaz, 2013, “The influence of the spin-orbit torques on the current-driven domain wall motion,” AIP Adv. **3**, 072109.

Martínez, Eduardo, and Óscar Alejos, 2014, “Coupled Dzyaloshinskii walls and their current-induced dynamics by the spin Hall effect,” J. Appl. Phys. **116**, 023909.

Meckler, S., M. Gyamfi, O. Pietzsch, and R. Wiesendanger, 2009, “A low-temperature spin-polarized scanning tunneling microscope operating in a fully rotatable magnetic field,” Rev. Sci. Instrum. **80**, 023708.

Meckler, S., N. Mikuszeit, A. Preßler, E. Y. Vedmedenko, O. Pietzsch, and R. Wiesendanger, 2009, “Real-Space Observation of a Right-Rotating Inhomogeneous Cycloidal Spin Spiral by Spin-Polarized Scanning Tunneling Microscopy in a Triple Axes Vector Magnet,” Phys. Rev. Lett. **103**, 157201.

Meier, T. N. G., M. Kronseder, and C. H. Back, 2017, “Domain-width model for perpendicularly magnetized systems with Dzyaloshinskii-Moriya interaction,” Phys. Rev. B **96**, 144408.

Meijer, Mariëlle J., Juriaan Lucassen, Rembert A. Duine, Henk J. M. Swagten, Bert Koopmans, Reinoud Lavrijsen, and Marcos H. D. Guimarães, 2020, “Chiral spin spirals at the surface of the van der Waals ferromagnet $\mathrm{Fe_3GeTe_2}$,” Nano Lett. **20**, 8563–8568.

Meijer, Mariëlle J., Juriaan Lucassen, Fabian Kloodt-Twesten, Robert Frömter, Oleg Kurnosikov, Rembert A. Duine, Henk J. M. Swagten, Bert Koopmans, and Reinoud Lavrijsen, 2020, “Magnetic Chirality Controlled by the Interlayer Exchange Interaction,” Phys. Rev. Lett. **124**, 207203.

Melcher, R. L., 1973, “Linear Contribution to Spatial Dispersion in the Spin-Wave Spectrum of Ferromagnets,” Phys. Rev. Lett. **30**, 125.

Metaxas, P. J., J. P. Jamet, A. Mougin, M. Cormier, J. Ferré, V. Baltz, B. Rodmacq, B. Dieny, and R. L. Stamps, 2007, “Creep and Flow Regimes of Magnetic Domain-Wall Motion in Ultrathin Pt/Co/Pt Films with Perpendicular Anisotropy,” Phys. Rev. Lett. **99**, 217208.

Michels, Andreas, *et al.*, 2019, “Microstructural-defect-induced Dzyaloshinskii-Moriya interaction,” Phys. Rev. B **99**, 014416.

Miron, Ioan Mihai, Gilles Gaudin, Stéphane Auffret, Bernard Rodmacq, Alain Schuhl, Stefania Pizzini, Jan Vogel, and Pietro Gambardella, 2010, “Current-driven spin torque induced by the Rashba effect in a ferromagnetic metal layer,” Nat. Mater. **9**, 230.

Miron, Ioan Mihai, *et al.*, 2011, “Fast current-induced domain-wall motion controlled by the Rashba effect,” Nat. Mater. **10**, 419.

Mock, R., B. Hillebrands, and R. Sandercock, 1987, “Construction and performance of a Brillouin scattering set-up using a triple-pass tandem Fabry-Perot interferometer,” J. Phys. E **20**, 656.

Moon, Jung-Hwan, Soo-Man Seo, Kyung-Jin Lee, Kyoung-Whan Kim, Jisu Ryu, Hyun-Woo Lee, R. D. McMichael, and M. D. Stiles, 2013, “Spin-wave propagation in the presence of interfacial Dzyaloshinskii-Moriya interaction,” Phys. Rev. B **88**, 184404.

Moon, Kyoung-Woong, Duck-Ho Kim, Sang-Cheol Yoo, Soong-Geun Je, Byong Sun Chun, Wondong Kim, Byoung-Chul Min, Chanyong Hwang, and Sug-Bong Choe, 2015, “Magnetic bubblecade memory based on chiral domain walls,” Sci. Rep. **5**, 9166.

Moore, T. A., I. M. Miron, G. Gaudin, G. Serret, S. Auffret, B. Rodmacq, A. Schuhl, S. Pizzini, J. Vogel, and M. Bonfim, 2008, “High domain wall velocities induced by current in ultrathin $\mathrm{Pt/Co/AlO}_x$ wires with perpendicular magnetic anisotropy,” Appl. Phys. Lett. **93**, 262504; **95**, 179902(E) (2009).

Moreau-Luchaire, C., *et al.*, 2016, “Additive interfacial chiral interaction in multilayers for stabilization of small individual skyrmions at room temperature,” Nat. Nanotechnol. **11**, 444–448.

Moriya, Tôru, 1960, “Anisotropic superexchange interaction and weak ferromagnetism,” Phys. Rev. **120**, 91.

Mühlbauer, S., B. Binz, F. Jonietz, C. Pfleiderer, A. Rosch, A. Neubauer, R. Georgii, and P. Böni, 2009, “Skyrmion lattice in a chiral magnet,” Science **323**, 915–919.

Nasseri, S. Ali, Eduardo Martinez, and Gianfranco Durin, 2018, "Collective coordinate descriptions of magnetic domain wall motion in perpendicularly magnetized nanostructures under the application of in-plane fields," J. Magn. Magn. Mater. **468**, 25–43.

Nasseri, S. Ali, Simone Moretti, Eduardo Martinez, Claudio Serpico, and Gianfranco Durin, 2017, "Collective coordinate models of domain wall motion in perpendicularly magnetized systems under the spin Hall effect and longitudinal fields," J. Magn. Magn. Mater. **426**, 195–201.

Nembach, Hans T., Emilie Jué, Eric R. Evarts, and Justin M. Shaw, 2020, "Correlation between Dzyaloshinskii-Moriya interaction and orbital angular momentum at an oxide-ferromagnet interface," Phys. Rev. B **101**, 020409.

Nembach, Hans T., Justin M. Shaw, Mathias Weiler, Emilie Jué, and Thomas J. Silva, 2015, "Linear relation between Heisenberg exchange and interfacial Dzyaloshinskii-Moriya interaction in metal films," Nat. Phys. **11**, 825–829.

Neusser, S., G. Duerr, H. G. Bauer, S. Tacchi, M. Madami, G. Woltersdorf, G. Gubbiotti, C. H. Back, and D. Grundler, 2010, "Anisotropic Propagation and Damping of Spin Waves in a Nanopatterned Antidot Lattice," Phys. Rev. Lett. **105**, 067208.

Pai, Chi-Feng, Maxwell Mann, Aik Jun Tan, and Geoffrey S. D. Beach, 2016, "Determination of spin torque efficiencies in heterostructures with perpendicular magnetic anisotropy," Phys. Rev. B **93**, 144409.

Parkin, Stuart, and See-Hun Yang, 2015, "Memory on the racetrack," Nat. Nanotechnol. **10**, 195.

Pellegren, J. P., D. Lau, and V. Sokalski, 2017, "Dispersive Stiffness of Dzyaloshinskii Domain Walls," Phys. Rev. Lett. **119**, 027203.

Perini, Marco, Sebastian Meyer, Bertrand Dupé, Stephan von Malottki, André Kubetzka, Kirsten von Bergmann, Roland Wiesendanger, and Stefan Heinze, 2018, "Domain walls and Dzyaloshinskii-Moriya interaction in epitaxial Co/Ir(111) and Pt/Co/Ir(111)," Phys. Rev. B **97**, 184425.

Petit, Dorothée, Peter R. Seem, Marine Tillette, Rhodri Mansell, and Russell P. Cowburn, 2015, "Two-dimensional control of field-driven magnetic bubble movement using Dzyaloshinskii-Moriya interactions," Appl. Phys. Lett. **106**, 022402.

Pham, Thai Ha, *et al.*, 2016, "Very large domain wall velocities in Pt/Co/GdO$_x$ and Pt/Co/Gd trilayers with Dzyaloshinskii-Moriya interaction," Europhys. Lett. **113**, 67001.

Pietzsch, Oswald, and Roland Wiesendanger, 2011, "Non-collinear magnetic order in nanostructures investigated by spin-polarized scanning tunneling microscopy," Pure Appl. Chem. **83**, 1981–1988.

Pizzini, S., *et al.*, 2014, "Chirality-Induced Asymmetric Magnetic Nucleation in Pt/Co/AlO$_x$ Ultrathin Microstructures," Phys. Rev. Lett. **113**, 047203.

Prabhakar, A., and D. Stancil, 2009, *Spin Waves* (Springer-Verlag, Boston).

Quan, J., X. Zhao, W. Liu, L. Liu, Y. Song, Y. Li, J. Ma, S. Li, X. Zhao, and Z. Zhang, 2020, "Enhancement of spin-orbit torque and modulation of Dzyaloshinskii-Moriya interaction in Pt$_{100-x}$Cr$_x$/Co/AlO$_x$ trilayer," Appl. Phys. Lett. **117**, 222405.

Rojas-Sánchez, J. C., and A. Fert, 2019, "Compared Efficiencies of Conversions between Charge and Spin Current by Spin-Orbit Interactions in Two- and Three-Dimensional Systems," Phys. Rev. Appl. **11**, 054049.

Romming, Niklas, Henning Pralow, André Kubetzka, Markus Hoffmann, Stephan von Malottki, Sebastian Meyer, Bertrand Dupé, Roland Wiesendanger, Kirsten von Bergmann, and Stefan Heinze, 2018, "Competition of Dzyaloshinskii-Moriya and Higher-Order Exchange Interactions in Rh/Fe Atomic Bilayers on Ir(111)," Phys. Rev. Lett. **120**, 207201.

Rößler, U. K., A. N. Bogdanov, and C. Pfleiderer, 2006, "Spontaneous skyrmion ground states in magnetic metals," Nature (London) **442**, 797.

Rougemaille, N., and A. K. Schmid, 2010, "Magnetic imaging with spin-polarized low-energy electron microscopy," Eur. Phys. J. Appl. Phys. **50**, 20101.

Rowan-Robinson, R. M., A. A. Stashkevich, Y. Roussigné, M. Belmeguenai, S.-M. Chérif, A. Thiaville, T. P. A. Hase, A. T. Hindmarch, and D. Atkinson, 2017, "The interfacial nature of proximity-induced magnetism and the Dzyaloshinskii-Moriya interaction at the Pt/Co interface," Sci. Rep. **7**, 16835.

Ryu, Kwang-Su, Luc Thomas, See-Hun Yang, and Stuart Parkin, 2013, "Chiral spin torque at magnetic domain walls," Nat. Nanotechnol. **8**, 527.

Ryu, Kwang-Su, Luc Thomas, See-Hun Yang, and Stuart S. P. Parkin, 2012, "Current induced tilting of domain walls in high velocity motion along perpendicularly magnetized micron-sized Co/Ni/Co racetracks," Appl. Phys. Express **5**, 093006.

Ryu, Kwang-Su, See-Hun Yang, Luc Thomas, and Stuart S. P. Parkin, 2014, "Chiral spin torque arising from proximity-induced magnetization," Nat. Commun. **5**, 3910.

Saha, S., *et al.*, 2019, "Formation of Néel-type skyrmions in an antidot lattice with perpendicular magnetic anisotropy," Phys. Rev. B **100**, 144435.

Sarma, Bhaskarjyoti, Felipe Garcia-Sanchez, S. Ali Nasseri, Arianna Casiraghi, and Gianfranco Durin, 2018, "Dynamics and morphology of chiral magnetic bubbles in perpendicularly magnetized ultra-thin films," J. Magn. Magn. Mater. **456**, 433–438.

Schilz, W., 1973, "Spin-wave propagation in epitaxial YIG films," Philips Res. Rep. **28**, 50–65.

Schlotter, Sarah, Parnika Agrawal, and Geoffrey S. D. Beach, 2018, "Temperature dependence of the Dzyaloshinskii-Moriya interaction in Pt/Co/Cu thin film heterostructures," Appl. Phys. Lett. **113**, 092402.

Schott, M., L. Ranno, H. Béa, C. Baraduc, S. Auffret, and A. Bernand-Mantel, 2021, "Electric field control of interfacial Dzyaloshinskii-Moriya interaction in Pt/Co/AlO$_x$ thin films," J. Magn. Magn. Mater. **520**, 167122.

Schryer, N. L., and L. R. Walker, 1974, "The motion of 180° domain walls in uniform dc magnetic fields," J. Appl. Phys. **45**, 5406–5421.

Seo, Soo-Man, Kyoung-Whan Kim, Jisu Ryu, Hyun-Woo Lee, and Kyung-Jin Lee, 2012, "Current-induced motion of a transverse magnetic domain wall in the presence of spin Hall effect," Appl. Phys. Lett. **101**, 022405.

Serga, A. A., A. V. Chumak, and B. Hillebrands, 2010, "YIG magnonics," J. Phys. D **43**, 264002.

Shahbazi, Kowsar, Aleš Hrabec, Simone Moretti, Michael B. Ward, Thomas A. Moore, Vincent Jeudy, Eduardo Martinez, and Christopher H. Marrows, 2018, "Magnetic properties and field-driven dynamics of chiral domain walls in epitaxial Pt/Co/Au$_x$/Pt$_{1-x}$ trilayers," Phys. Rev. B **98**, 214413.

Shahbazi, Kowsar, Joo-Von Kim, Hans T. Nembach, Justin M. Shaw, Andreas Bischof, Marta D. Rossell, Vincent Jeudy, Thomas A. Moore, and Christopher H. Marrows, 2019, "Domain-wall motion and interfacial Dzyaloshinskii-Moriya interactions in Pt/Co/Ir(t_{Ir})/Ta multilayers," Phys. Rev. B **99**, 094409.

Shao, Q., Y. Li, G. Yu, S. K. Kim, X. Che, C. Tang, Q. L. He, Y. Tserkovnyak, J. Shi, and K. L. Wang, 2019, "Topological Hall effect at above room temperature in heterostructures composed of a magnetic insulator and a heavy metal," Nat. Electron. **2**, 182–186.

Shepley, Philippa M., Harry Tunnicliffe, Kowsar Shahbazi, Gavin Burnell, and Thomas A. Moore, 2018, "Magnetic properties, domain-wall creep motion, and the Dzyaloshinskii-Moriya interaction in Pt/Co/Ir thin films," Phys. Rev. B **97**, 134417.

Slonczewski, J. C., 1996, "Current-driven excitation of magnetic multilayers," J. Magn. Magn. Mater. **159**, L1–L7.

Sobolev, V. L., S. C. Chen, and H. L. Huang, 1995, "Domain wall dynamics in the presence of an external magnetic field normal to the anisotropy axis," J. Magn. Magn. Mater. **147**, 284.

Sobolev, Vladimir L., Huei Li Huang, and Shoan Chung Chen, 1994, "Generalized equations for domain wall dynamics," J. Appl. Phys. **75**, 5797.

Soohoo, R. F., 1963, "General exchange boundary condition and surface anisotropy energy of a ferromagnet," Phys. Rev. **131**, 594–601.

Soucaille, R., M. Belmeguenai, J. Torrejon, J.-V. Kim, T. Devolder, Y. Roussigné, S.-M. Chérif, A. A. Stashkevich, M. Hayashi, and J.-P. Adam, 2016, "Probing the Dzyaloshinskii-Moriya interaction in CoFeB ultrathin films using domain wall creep and Brillouin light spectroscopy," Phys. Rev. B **94**, 104431.

Soumyanarayanan, Anjan, *et al.*, 2017, "Tunable room-temperature magnetic skyrmions in Ir/Fe/Co/Pt multilayers," Nat. Mater. **16**, 898–904.

Srivastava, Titiksha, *et al.*, 2018, "Large-voltage tuning of Dzyaloshinskii-Moriya interactions: A route toward dynamic control of skyrmion chirality," Nano Lett. **18**, 4871–4877.

Stamps, R. L., and Burkard Hillebrands, 1991, "Dipolar interactions and the magnetic behavior of two-dimensional ferromagnetic systems," Phys. Rev. B **44**, 12417–12423.

Stashkevich, A. A., M. Belmeguenai, Y. Roussigné, S. M. Cherif, M. Kostylev, M. Gabor, D. Lacour, C. Tiusan, and M. Hehn, 2015, "Experimental study of spin-wave dispersion in Py/Pt film structures in the presence of an interface Dzyaloshinskii-Moriya interaction," Phys. Rev. B **91**, 214409.

Stejskal, Ondřej, André Thiaville, Jaroslav Hamrle, Shunsuke Fukami, and Hideo Ohno, 2020, "Current distribution in metallic multilayers from resistance measurements," Phys. Rev. B **101**, 235437.

Tacchi, S., R. E. Troncoso, M. Ahlberg, G. Gubbiotti, M. Madami, J. Åkerman, and P. Landeros, 2017, "Interfacial Dzyaloshinskii-Moriya Interaction in Pt/CoFeB Films: Effect of the Heavy-Metal Thickness," Phys. Rev. Lett. **118**, 147201.

Tanaka, Masaaki, Musashi Shimazaki, Tatsuro Ohmasa, Takafumi Suzuki, Shunsuke Honda, Syuta Honda, Hiroyuki Awano, and Ko Mibu, 2020, "Stabilization of Néel-type domain walls in multilayered magnetic wires using antiferromagnetic interlayer exchange coupling," J. Appl. Phys. **128**, 063902.

Tarasenko, S. V., A. Stankiewicz, V. V. Tarasenko, and J. Ferré, 1998, "Bloch wall dynamics in ultrathin ferromagnetic films," J. Magn. Magn. Mater. **189**, 19–24.

Tersoff, J., and D. R. Hamann, 1983, "Theory and Application for the Scanning Tunneling Microscope," Phys. Rev. Lett. **50**, 1998–2001.

Tetienne, J.-P., *et al.*, 2015, "The nature of domain walls in ultrathin ferromagnets revealed by scanning nanomagnetometry," Nat. Commun. **6**, 6733.

Thiaville, A., J. M. García, and J. Miltat, 2002, "Domain wall dynamics in nanowires," J. Magn. Magn. Mater. **242–245**, 1061.

Thiaville, A., Y. Nakatani, J. Miltat, and Y. Suzuki, 2005, "Micromagnetic understanding of current-driven domain wall motion in patterned nanowires," Europhys. Lett. **69**, 990.

Thiaville, André, Stanislas Rohart, Émilie Jué, Vincent Cros, and Albert Fert, 2012, "Dynamics of Dzyaloshinskii domain walls in ultrathin magnetic films," Europhys. Lett. **100**, 57002.

Torrejon, Jacob, Junyeon Kim, Jaivardhan Sinha, Seiji Mitani, Masamitsu Hayashi, Michihiko Yamanouchi, and Hideo Ohno, 2014, "Interface control of the magnetic chirality in CoFeB/MgO heterostructures with heavy-metal underlayers," Nat. Commun. **5**, 4655.

Tsurkan, S., and Kh. Zakeri, 2020, "Giant Dzyaloshinskii-Moriya interaction in epitaxial Co/Fe bilayers with C_{2v} symmetry," Phys. Rev. B **102**, 060406(R).

Udvardi, L., and L. Szunyogh, 2009, "Chiral Asymmetry of the Spin-Wave Spectra in Ultrathin Magnetic Films," Phys. Rev. Lett. **102**, 207204.

Udvardi, L., L. Szunyogh, K. Palotás, and P. Weinberger, 2003, "First-principles relativistic study of spin waves in thin magnetic films," Phys. Rev. B **68**, 104436.

Vaňatka, M., J.-C. Rojas-Sánchez, J. Vogel, M. Bonfim, M. Belmeguenai, Y Roussigné, A. Stashkevich, A. Thiaville, and S. Pizzini, 2015, "Velocity asymmetry of Dzyaloshinskii domain walls in the creep and flow regimes," J. Phys. Condens. Matter **27**, 326002.

Vedmedenko, E. Y., *et al.*, 2020, "The 2020 magnetism roadmap," J. Phys. D **53**, 453001.

Vélez, Saül, *et al.*, 2019, "High-speed domain wall racetracks in a magnetic insulator," Nat. Commun. **10**, 4750.

Vlaminck, V., and M. Bailleul, 2010, "Spin-wave transduction at the submicrometer scale: Experiment and modeling," Phys. Rev. B **81**, 014425.

Vogel, Jan, Jérôme Moritz, and Olivier Fruchart, 2006, "Nucleation of magnetisation reversal, from nanoparticles to bulk materials," C.R. Phys. **7**, 977–987.

Walker, L. R., 1956, Bell Telephone Laboratories Memorandum (unpublished).

Wang, Hanchen, *et al.*, 2020, "Chiral Spin-Wave Velocities Induced by All-Garnet Interfacial Dzyaloshinskii-Moriya Interaction in Ultrathin Yttrium Iron Garnet Films," Phys. Rev. Lett. **124**, 027203.

Wang, X. S., H. W. Zhang, and X. R. Wang, 2018, "Topological Magnonics: A Paradigm for Spin-Wave Manipulation and Device Design," Phys. Rev. Appl. **9**, 024029.

Wells, Adam W. J., Philippa M. Shepley, Christopher H. Marrows, and Thomas A. Moore, 2017, "Effect of interfacial intermixing on the Dzyaloshinskii-Moriya interaction in Pt/Co/Pt," Phys. Rev. B **95**, 054428.

Wong, Q. Y., W. L. Gan, F. L. Luo, G. J. Lim, C. C. I. Ang, F. N. Tan, W. C. Law, and W. S. Lew, 2018, "*In situ* Kerr and harmonic measurement in determining current-induced effective fields in MgO/CoFeB/Ta," J. Phys. D **51**, 115004.

Woo, Seonghoon, *et al.*, 2016, "Observation of room-temperature magnetic skyrmions and their current-driven dynamics in ultrathin metallic ferromagnets," Nat. Mater. **15**, 501–506.

Woo, Seonghoon, *et al.*, 2017, "Spin-orbit torque-driven skyrmion dynamics revealed by time-resolved x-ray microscopy," Nat. Commun. **8**, 15573.

Wortmann, D., S. Heinze, Ph. Kurz, G. Bihlmayer, and S. Blügel, 2001, "Resolving Complex Atomic-Scale Spin Structures by Spin-Polarized Scanning Tunneling Microscopy," Phys. Rev. Lett. **86**, 4132–4135.

Yamamoto, Kento, Abdul-Muizz Pradipto, Kenji Nawa, Toru Akiyama, Tomonori Ito, Teruo Ono, and Kohji Nakamura, 2017, "Interfacial Dzyaloshinskii-Moriya interaction and orbital magnetic moments of metallic multilayer films," AIP Adv. **7**, 056302.

Yang, H., S. Hu, M. Tang, S. Che, H. Chen, D. Wu, and X. Qiu, 2021, "Spin-orbit torque and Dzyaloshinskii-Moriya interaction in perpendicularly magnetized heterostructures with iridium," Appl. Phys. Lett. **118**, 062409.

Yang, Hongxin, Olivier Boulle, Vincent Cros, Albert Fert, and Mairbek Chshiev, 2018, "Controlling Dzyaloshinskii-Moriya interaction via chirality dependent atomic-layer stacking, insulator capping and electric field," Sci. Rep. **8**, 12356.

Yang, Hongxin, André Thiaville, Stanislas Rohart, Albert Fert, and Mairbek Chshiev, 2015, "Anatomy of Dzyaloshinskii-Moriya Interaction at Co/Pt Interfaces," Phys. Rev. Lett. **115**, 267210.

Yang, Hongxin, *et al.*, 2018, "Significant Dzyaloshinskii-Moriya interaction at graphene-ferromagnet interfaces due to the Rashba effect," Nat. Mater. **17**, 605–609.

Yoshida, Y., S. Schröder, P. Ferriani, D. Serrate, A. Kubetzka, K. von Bergmann, S. Heinze, and R. Wiesendanger, 2012, "Conical Spin-Spiral State in an Ultrathin Film Driven by Higher-Order Spin Interactions," Phys. Rev. Lett. **108**, 087205.

Yoshimura, Yoko, Kab-Jin Kim, Takuya Taniguchi, Takayuki Tono, Kohei Ueda, Ryo Hiramatsu, Takahiro Moriyama, Keisuke Yamada, Yoshinobu Nakatani, and Teruo Ono, 2016, "Soliton-like magnetic domain wall motion induced by the interfacial Dzyaloshinskii-Moriya interaction," Nat. Phys. **12**, 157.

Yu, Guoqiang, Pramey Upadhyaya, Xiang Li, Wenyuan Li, Se Kwon Kim, Yabin Fan, Kin L. Wong, Yaroslav Tserkovnyak, Pedram Khalili Amiri, and Kang L. Wang, 2016, "Room-temperature creation and spin-orbit torque manipulation of skyrmions in thin films with engineered asymmetry," Nano Lett. **16**, 1981–1988.

Yu, Guoqiang, *et al.*, 2017, "Room-temperature skyrmion shift device for memory application," Nano Lett. **17**, 261–268.

Yu, Jiawei, Xuepeng Qiu, Yang Wu, Jungbum Yoon, Praveen Deorani, Jean Mourad Besbas, Aurelien Manchon, and Hyunsoo Yang, 2016, "Spin orbit torques and Dzyaloshinskii-Moriya interaction in dual-interfaced Co-Ni multilayers," Sci. Rep. **6**, 32629.

Yu, X. Z., Y. Onose, N. Kanazawa, J. H. Park, J. H. Han, Y. Matsui, N. Nagaosa, and Y. Tokura, 2010, "Real-space observation of a two-dimensional skyrmion crystal," Nature (London) **465**, 901.

Yun, Jijun, Dong Li, Baoshan Cui, Xiaobin Guo, Kai Wu, Xu Zhang, Yupei Wang, Jian Mao, Yalu Zuo, and Li Xi, 2018, "Current induced domain wall motion and tilting in Pt/Co/Ta structures with perpendicular magnetic anisotropy in the presence of the Dyzaloshinskii-Moriya interaction," J. Phys. D **51**, 155001.

Zakeri, Kh., Y. Zhang, J. Prokop, T.-H. Chuang, N. Sakr, W. X. Tang, and J. Kirschner, 2010, "Asymmetric Spin-Wave Dispersion on Fe(110): Direct Evidence of the Dzyaloshinskii-Moriya Interaction," Phys. Rev. Lett. **104**, 137203.

Zakeri, Khalil, 2017, "Probing of the interfacial Heisenberg and Dzyaloshinskii-Moriya exchange interaction by magnon spectroscopy," J. Phys. Condens. Matter **29**, 013001.

Zhang, S., and Z. Li, 2004, "Roles of Nonequilibrium Conduction Electrons on the Magnetization Dynamics of Ferromagnets," Phys. Rev. Lett. **93**, 127204.

Zhang, Vanessa Li, Kai Di, Hock Siah Lim, Ser Choon Ng, Meng Hau Kuok, Jiawei Yu, Jungbum Yoon, Xuepeng Qiu, and Hyunsoo Yang, 2015, "In-plane angular dependence of the spin-wave nonreciprocity of an ultrathin film with Dzyaloshinskii-Moriya interaction," Appl. Phys. Lett. **107**, 022402.

Zhang, W., R. Chen, B. Jiang, X. Zhao, W. Zhao, S. S. Yan, G. Han, S. Yu, G. Liu, and S. Kang, 2021, "Tunable interfacial Dzyaloshinskii-Moriya interaction in symmetrical Au/[Fe/Au]n multilayers," Nanoscale **13**, 2665–2672.

Zhang, W., H. Zhong, R. Zang, Y. Zhang, S. Yu, G. Han, G. L. Liu, S. S. Yan, S. Kang, and L. M. Mei, 2018, "Electrical field enhanced interfacial Dzyaloshinskii-Moriya interaction in MgO/Fe/Pt system," Appl. Phys. Lett. **113**, 122406.

Zheludev, A., S. Maslov, G. Shirane, I. Tsukada, T. Masuda, K. Uchinokura, I. Zaliznyak, R. Erwin, and L. P. Regnault, 1999, "Magnetic anisotropy and low-energy spin waves in the Dzyaloshinskii-Moriya spiral magnet $Ba_2CuGe_2O_7$," Phys. Rev. B **59**, 11432–11444.